Development and validation of a numerical latent heat thermal energy storage model with application in a CSP-biomass system

Auteur : Kohnen, Oliver
Promoteur(s) : Dewallef, Pierre
Faculté : Faculté des Sciences appliquées
Diplôme : Master en ingénieur civil électromécanicien, à finalité approfondie
Année académique : 2015-2016
URI/URL : http://hdl.handle.net/2268.2/1675

University of Liège
Faculty of Applied Science

Master thesis

Development and validation of a numerical latent heat thermal energy storage model with application in a CSP-biomass system

Author: KOHNEN Oliver

Submitted in fulfillment of the requirements
for the degree of Master of Science in
Electromecanical Civil Engineering

Academic year 2015-2016

Development and validation of a numerical latent heat thermal energy storage model with application in a CSP-biomass system

Submitted in fulfillment of the requirements
for the degree of Master of Science in
Electromecanical Civil Engineering by Kohnen Oliver

This Thesis has been written at:

AIT (Austrian Institute of Technology) GmbH
Energy Department
Buiness case of Sustainable Thermal Energy Systems (TES)
Giefinggasse 2
1210 Vienna, Austria

Examination Committee:

Prof. DEWALLEF Pierre, ULg (Adviser)
Prof. QUOILIN Sylvain, ULg
Prof. LEMORT Vincent, ULg
Prof. LEONARD Grégoire, ULg
Dr. HENGSTBERGER Florian, AIT (Supervisor)

Declaration

I, Kohnen Oliver, declare that this thesis titled, *Development and validation of a numerical latent heat thermal energy storage model with application in a CSP-biomass system*, and the work presented in it are my own. I confirm that:

- Where any part of this thesis has previously been submitted for a degree or any other qualification at this University or any other institution, this has been clearly stated.
- Where I have consulted the published work of others, this is always clearly attributed.
- Where I have quoted from the work of others, the source is always given. With the exception of such quotations, this thesis is entirely my own work.
- I have acknowledged all main sources of help.
- Where the thesis is based on work done by myself jointly with others, I have made clear exactly what was done by others and what I have contributed myself.

Signed: 

Date: 10.08.2016

Acknowledgements

I am very grateful to Dr. Florian Hengstberger, who made this work possible. I wish to thank him for his countless explanations and advises, which have been essential for this work.

I would like to thank Adriano Desideri, for providing me the numeric model of the CSP-biomass system and for answering corresponding questions.

I am also grateful to Professor Pierre Dewallef, for his commitment to make my stay in Austria possible.

A special thanks goes to all the members of the Sustainable Thermal Energy Systems business case (TES) of the AIT, who warmly welcomed me, as well as my diploma colleagues, who provided an excellent atmosphere.

Last but not least, I would like to thank my family, my friends and especially my girlfriend for their unwavering support, even in the distance.

Abstract

This master thesis relates to the development of a latent heat thermal energy storage (LHTES) model and the validation against experimental measurement data.
Two 2D numeric models based on the *ThermoCycle* Modelica library using different model approaches have been established:
A white-box discretized and a grey-box single-node model have been developed. The models account for the temperature dependence of all material properties of phase change material (PCM), storage and heat transfer fluid (HTF).
Validation of both models based on experimental data from a LHTES lab-scaled prototype with partial and full charging and discharging has been performed. The statistical analysis proved the validity and usefulness of the model parameter sets. Differences between both models in terms of estimated parameters, relative errors and simulation times are presented and analysed.
After the optimized model parameters have been found, the validated discretized white-box PCM storage model is integrated in a practical application to improve the overall system efficiency.
The application scenario consists in a concentrated solar power (CSP) biomass combined heat and power (CHP) system based on organic Rankine cycle (ORC) technology developed in the framework of the EU founded BRICKER project. The PCM storage is introduced to the solar field in order to maximize the solar generated energy and hence reduce the biomass consummation.
A comparison with a thermocline storage concludes this work.

Contents

Nomenclature

a_m	mass fraction of molten PCM [-]
A	area [m^2]
A_{ap}	storage inner cross section area [m^2]
$A_{fins,tot}$	total fin area [m^2]
AU	heat transfer coefficient [$W\,K^{-1}$]
c_p	specific heat capacity [$J\,kg^{-1}\,K^{-1}$]
c_{lp}	average specific heat capacity between T^0 and T_m [$J\,kg^{-1}\,K^{-1}$]
c_{sp}	average specific heat capacity between T_m and T^f [$J\,kg^{-1}\,K^{-1}$]
$\tilde{c}_p$	apparent specific heat capacity [$J\,kg^{-1}\,K^{-1}$]
cov	covariance matrix
d_{fins}	fin thickness [m]
ΔT	transition width of the apparent specific heat capacity peak [K]
E	thermal energy [kW h]
f	solar fraction [-]
h	specific enthalpy [$J\,K^{-1}$]
l_{hex}	total heat exchanger length [m]
L	latent heat of fusion [$J\,kg^{-1}$]
m	mass [kg]
$\dot{m}$	mass flow [$kg\,s^{-1}$]
N	number of model cell components [-]
Nu	Nusselt number [-]
N_{tube}	number of HTF tubes in the storage[-]
$perr$	relative error [-]

Pr	Prandtl number [-]
$\dot{q}$	heat flux [$\mathrm{W\,m^2}$]
Q_{stored}	quantity of heat stored [J]
$\dot{Q}$	thermal power [W]
r	radial position [m]
R	heat resistance [$\mathrm{m^2\,K\,W^{-1}}$]
Re	Reynolds number [-]
T	temperature [°C]
T_m	PCM melting temperature [°C]
u	specific internal energy [$\mathrm{J\,kg^{-1}}$]
U	coefficient of heat transfer [$\mathrm{W\,m^{-2}\,K^{-1}}$]
V	volume [$\mathrm{m^3}$]
v	velocity [$\mathrm{m\ s^{-1}}$]
x	axial position [m]

Greek Symbols

δ	elements of the covariance matrix
λ	thermal conductivity [$\mathrm{W\,K^{-1}}$]
μ	location parameter of a normal distribution
ν	kinematic viscosity [$\mathrm{m^2\,s^{-1}}$]
π	circle constant (=3.1415...) [-]
ρ	density [$\mathrm{kg\,m^{-3}}$]
σ	scale parameter of a normal distribution
ϕ	probability distribution function

Subscripts and Superscripts

$\star$	reference value
0	initial value
1	related to PCM model 1
2	related to PCM model 2
ax	axial direction
BM	biomass
ex	exhaust/outlet
f	final
F	fins
H	heat transfer fluid
in	inner
out	outer
P	phase change material
SF	solar field
su	supply/inlet
tot	total
T	tube
W	tube wall (including fins)

Acronyms

BMB	biomass boiler
CHP	combined heat and power
CSP	concentrated solar power
DNI	direct normal irradiation [$\mathrm{W\,m^{-2}}$]
DSC	differential scanning calorimetry
HDPE	high density polyethylene
HEX	heat exchanger
HTF	heat transfer fluid
HVAC	heating, ventilation and air conditioning

LHS	latent heat storage
LHTES	latent heat thermal energy storage
ORC	organic Rankine cycle
PCM	phase change material
SF	solar field
SOC	state of charge
TES	thermal energy storage
VSP	vertical sump pump

Chapter 1

Introduction

1.1 Latent heat storages

The last 30 years were characterized by an significant increase in energy consumption, leading to substantial growth of greenhouse gases in atmosphere and, as consequence, to climatic changes. Last circumstance necessitate more effective utilization of energy in all sectors of human activity. Many countries subsidize the development of energy saving technologies and systems based on use of non-combustible renewable energy sources. Thermal energy storage plays significant role in developing the specified technologies [17].They are key elements for the effective thermal management in process heat and power generation. A thermal energy storage is indispensable for solar thermal applications when flexibility and dispatchability are demanded. The storages act as a buffer between energy demand and supply, thereby allowing both systems to be run independently from one another [19].
In the last three decades, latent heat thermal energy storages (LHTES) based on phase change materials (PCMs) have been subject to considerable research. They offer a significantly higher energy density compared to sensible heat storage systems [27]. The storage process is almost isothermal at the melting temperature of the phase change material [11]. Most of the phase change problems consider temperature ranges between 0 °C and 60 °C suitable for domestic heating applications [8]. However, latent heat storage above 100 °C are of particular interesting for high temperature applications because of the lower pressure than steam accumulators or pressurized water tanks, leading to cheaper investment costs for the tanks [28]. As most PCMs suffer

from low thermal conductivity, heat transfer enhancement techniques have to be used to effectively charge and discharge latent heat storages. [27] [8].

1.2 BRICKER CSP-biomass plant

The system is developed in the framework of the EU founded BRICKER project, aimed to develop scalable, replicable, high energy efficient, zero emissions and cost effective energy systems, to refurbish existing public-owned non-residential buildings [1]. It consists in a concentrated solar power (CSP) biomass combined heat and power (CHP) system based on organic Rankine cycle (ORC) technology. Coupled with heat recovery ventilation technology and novel insulation material, the CHP system has the aim of reducing the energy consumption of buildings by up to 50 % [12].

1.3 Goal of this work

This thesis aims at developing a numeric model of a latent heat thermal energy storage and its validation by experimental data of a laboratory storage prototype. Two models will be developed using different modelling approaches.
A waste of solar thermal energy occurs in the CSP-biomass system introduced above, when there is an superior solar irradiation. Using a thermal storage, for example a LHTES, the excess of generated solar power can be stored and used in low-sunlight hours. The implementation of the PCM storage aims to increase the solar fraction, meaning to maximise the total solar generated energy of the system.

1.4 Organization of the report

After this short introduction of latent heat storages and their practical application, a literature review on PCM storages in general (generalities, storage designs, materials) as well as a system background of the CSP-biomass system will be given in chapter 2.
Chapter 3 treats the model set-up for the discretized and single-node model, presented in 3.1 and 3.2, respectively. Detailed mathematical models for each component and heat transfer between will be demonstrated. The implementation in *Dymola*, a Modelica based dynamic modelling environment, is presented at the end of each model component section.
The validation of the models is treated in chapter 4.1 for the discretized and 4.2 for the single-node model. The parameter optimization followed by a statistical analyse is given thereby. The result of storage implementation to the CSP-biomass system are presented in section 5.
This thesis ends with a summary of the achieved results.

Chapter 2

Literature review

2.1 PCM storage

2.1.1 Generalities

Latent heat thermal energy storages (LHTES) are based on the absorption or release of thermal energy when the storage phase change material (PCM) undergoes a phase change from solid to liquid or liquid to gas or vice versa. The storage capacity of the LHTES system for an ideal PCM (see figure 2.1) is given in Eqs. (2.1) and (2.2) [24].

$$Q_{stored} = \int_{T^0}^{T_m} mc_p dT + ma_m L + \int_{T_m}^{T^f} mc_p dT \tag{2.1}$$

$$Q_{stored} = m[c_{sp}(T_m - T^0) + a_m L + c_{lp}(T^f - T_m)] \tag{2.2}$$

LHTES are particularly attractive due to their specific thermal proprieties, which are essentially high-energy storage density and the characteristic to store thermal energy at nearly constant temperature. Latter is called the phase-transition temperature of phase change material (PCM). Phase transition can be classified in the following four forms [24]:

- In **solid–solid** transitions, thermal energy is stored as the material is transformed from one crystalline phase to another. This storage phenomena has generally small latent heat and small volume changes than solid–liquid transitions. However, solid–solid phase change materials offer the advantages of less severe container requirements and a greater design flexibility.[24]. In the case of thermal storage applications, relatively few solid-solid PCMs with suitable heats of fusion and transition temperatures have been identified so far [14].

- **Solid–gas** and **liquid–gas** transitions have the highest latent heat of phase transition, compared to the other methods. Their large volume change during the phase transition is associated with containment problems due to pressure rise [24]. They are therefore rarely considered for practical applications [14].

- **Solid–liquid** transformations have smaller latent heat than liquid–gas. However, these transformations involve only a small change in volume. It is of the order of 10% or less [24].

The phase change from solid to liquid or vice versa is preferred because the operating pressure is lower than liquid to gas or solid to gas phase changes [11]. In the following we will base our review exclusively on materials used for **solid-liquid** phase change.

2.1.2 Storage design

There are three basic components that all latent heat thermal energy storages have in common [14]:

- A **phase change material** that undergoes the phase transition in a specific operating temperature range and where the the thermal energy is stored as the latent heat of fusion (L).

- A **container** for the PCM.

- A **heat exchanging surface** for transferring thermal energy from the heat transfer fluid to the PCM and vice versa.

Therefore, the development of a LHTES system requires an excellent understanding of two essentially subjects: heat storage materials (PCMs) and heat exchangers. A special design of the heat exchanger to be used is needed, due to the low thermal conductivity of PCMs in general [24].

There are several storage designs developed over the years. The most common concept are:

Shell and tube

The shell and tube design is based on a (finned) heat exchanger placed in tank containing the PCM [28]. A labscale prototype of the last design configuration is presented in section 2.1.7.

Macro-encapsulation

The macro-encapsulation storage design consists in the inclusion of PCM's such as paraffin in form of small packages such as tubes, pouches, spheres, panels or other containers. They can serve directly as heat exchangers or can be incorporated in building products [18].

Micro-encapsulation

Micro-encapsulation is characterized by the encapsulation of solid or liquid particles of $1\,\mu m$ to $1000\,\mu m$ diameter with a solid shell. Physical processes using this method are spray drying, centrifugal and fluidized bed processes, or coating processes e.g. in rolling cylinders [21]. Advantages of micro-encapsulation are the improvement of heat transfer to the HTF due to the large surface to volume ratio of the capsules. A potential drawback of micro-encapsulation is however the possible increase in subcooling chance [21]. The subcooling phenomena is presented in section 2.1.4.

2.1.3 Comparison to sensible heat storages

Figure 2.1 shows the difference between a sensible and a LHTES, with ideal materials (constant c_p and a transition width of 0 K for the PCM). In a sensible storage (green line), the thermal heat stored is associated with an increase in the storage material temperature. For a LHTES (red line), once the phase change temperature has been reached, no temperature change will

occur until all PCM has changed its phase. For temperatures different from the phase change temperature, the latent heat storage behaves like a sensible storage [22].

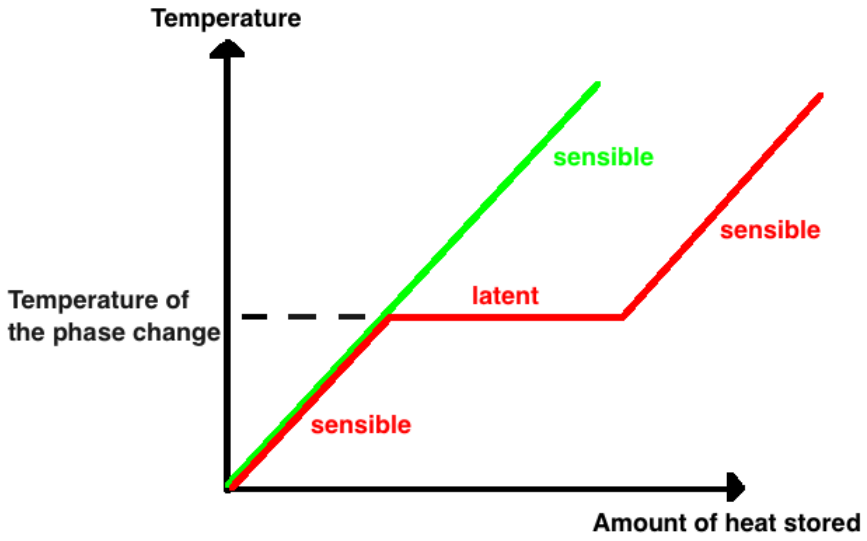

Figure 2.1: Comparison of sensible and latent heat storages in terms of temperature profile as a function of stored heat

In reality, the phase transition does not occur at a constant temperature (isothermal process), but in a certain temperature range, so that the horizontal line in figure 2.1 is a slightly increasing curve. For many materials, this transition temperature width is only of just a few degrees (about 10 K), so a nearly constant temperature profile can be archived around the phase change temperature. Consequently, thermal systems needing rather smooth and constant supply temperature profiles benefit from this storage technology [22].

2.1.4 Subcooling

Many phase change materials do not solidify immediately when the melting/-solidification temperature is reached. Crystallization often occurs well below the melting temperature. This effect is called subcooling or supercooling. Its effect on the temperature evolution is presented in figure 2.2 [21].

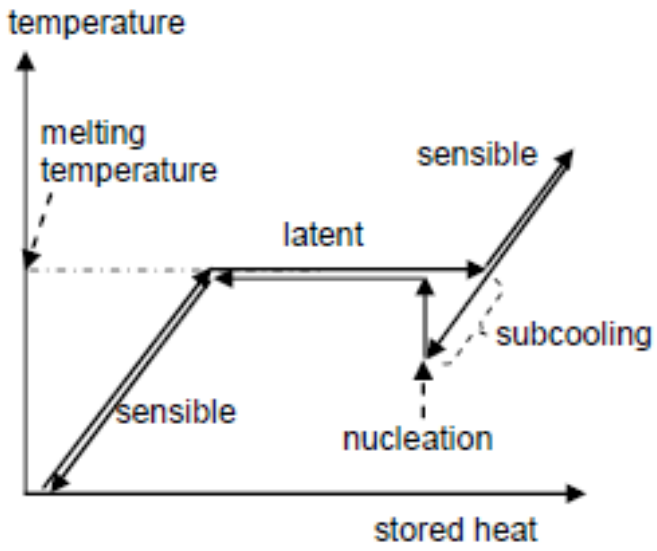

Figure 2.2: Effect of subcooling on a latent heat storage

During the melting process, there is no difference whether a PCM shows sub-cooling or not. But during release of thermal energy, the latent heat is not released when the melting temperature is reached due to subcooling. It makes it necessary to reduce the temperature well below the phase change temperature to release the latent heat stored in the material. If nucleation does not happen at all, only sensible energy is stored and the latent heat of fusion is not released at all. Subcooling can therefore be a serious problem in technical applications of PCM [21].

2.1.5 Phase change materials

The selection a PCM for a particular application is guided by the operating temperature of the heating or cooling and should be matched to the PCM transition temperature. Furthermore, the latent heat should be as high as possible, to limit the storage size. High thermal conductivity would provide higher charging and discharging rates of the stored energy.
Nowadays a large number of phase change materials are available in any required temperature range [24].
A classification of PCMs is given in figure 2.3.

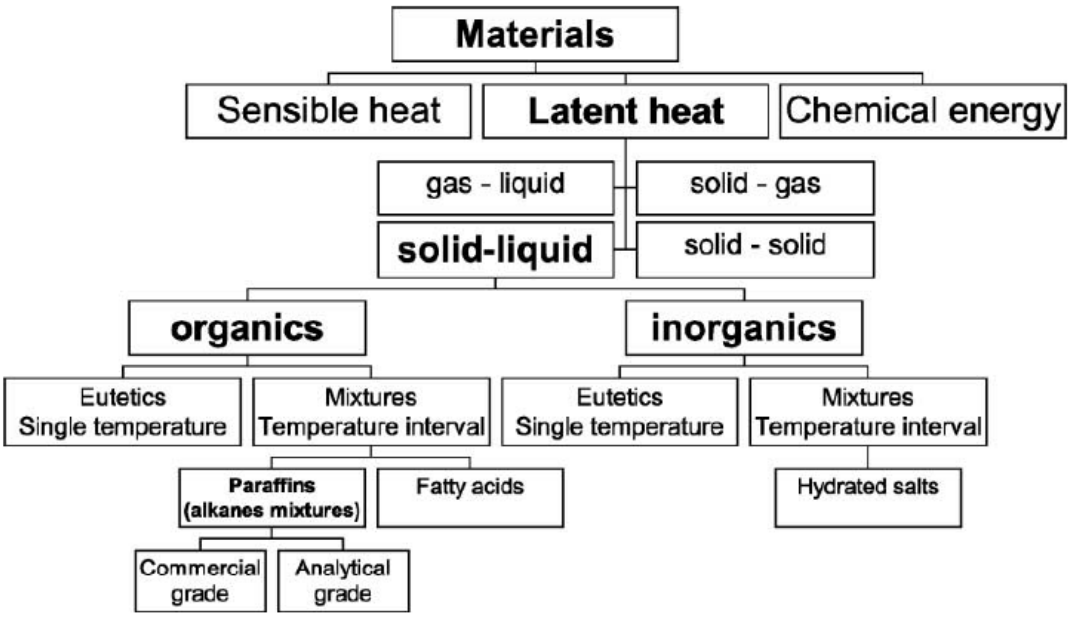

Figure 2.3: Classification of energy storage materials [7]

As no single PCM can have all properties for an ideal storage media, the available materials have to be used and it has to be tried to compensate the poor material properties by an appropriate storage design. For example metallic fins can be implemented into the storage to increase the thermal conductivity of the storage material [24].

PCM can be divided into the following main classes:

1. **Organic PCMs**
   Organic materials are classified as paraffin and non-paraffins:

   - **Paraffin** wax consists of a mixture of n-alkanes of the type

     $$\text{CH3–(CH2)}_n\text{–CH3}$$

     Both the phase transition temperature and latent heat increase with chain length [24].

   - The **non-paraffin** organic are among the phase change materials the most numerous class. Unlike the paraffins which have very similar properties, each of these materials have its own specific properties. The largest part of the class is composed of Esters,fatty acids, alcohol's and glycol's [24].

   Organic materials are characterized by congruent melting, meaning the propriety of repeated melting and freezing without phase segregation and subsequent degradation of the latent heat of fusion. Furthermore they crystallize with little or no subcooling and are usually non-corrosive [24].

2. **Inorganic PCMs**

   Inorganic materials are further classified as salt hydrate and metallics. These phase change materials show little and there is no degradation of heat of fusion with cycling [24].

   - **Salt hydrates** are made of alloys of inorganic salts and water forming a crystalline solid. Its general formula is AB-$n\text{H}_2\text{O}$. The solid–liquid transformation of salt hydrates consists in a dehydration of the salt, although this process is comparable with thermodynamic melting or solidification. At the melting point the

hydrate crystals breakup into a lower hydrate and water [24]:

$$\text{AB-}n\text{H}_2\text{O} \rightarrow \text{AB-}m\text{H}_2\text{O} + (n-m)\text{H}_2\text{O}$$

or anhydrous salt and water:

$$\text{AB-}n\text{H}_2\text{O} \rightarrow \text{AB} + n\ \text{H}_2\text{0}$$

One problem with the most salt hydrates is the fact that the released water from the crystallization process is not sufficient to dissolve all the present solid phase. Due to density difference, the lower hydrate settles down at the bottom of the container. This effect is called phase separation and consists in the main source of problem for the implementation of this PCM type [24].

- **Metallics**: This category contains the low melting metals and metal eutectic. Due to their high weight and cost, these metallics have not yet been seriously considered as phase change materials. However, when volume reduction is a main issue, they are good alternative because of the high heat of fusion [24].

3. **Eutectics**
   An eutectic is a composition of two or more materials. In the case of their utilization as phase change materials, eutectics nearly always melt and freeze without segregation. Since they solidify to an intimate mixture of crystals, they leave little opportunity for the components to separate. During the melting process, both components liquefy simultaneously, again without separation [24].

2.1.6 Applications

The applications of PCM storages can be divided into two main groups: **thermal protection or inertia** and **energy storage**. The main difference between the two fields relates to the thermal conductivity of the phase change material. In several applications in thermal protection it is appropriate to have low conductivity values, where as in storage systems low conductivity values can cause real problems since the capacity to absorb or release the

thermal energy is highly limited [27].
The most common applications where PCM are considered or already in use are [15] [27] [28]:

- Ice storages for HVAC applications
- Concentrated solar power
- Waste heat recovery in industrial processes
- Solar thermal systems
- Conservation and transport of temperature sensitive materials (food, etc.)
- Building applications (PCM integrated in walls, ceilings, etc.)

2.1.7 Laboratory prototype PCM storage

In the following section, a lab-scale shell and tube latent heat storage prototype is presented. It has been developed at the sustainable thermal energy system department of the Austrian Institute of Technology (AIT) in Vienna, Austria. Several measurement experiment have been realized by the laboratory staff. The results are used to validate the numeric storage models developed in the frame of this thesis. An in-depth discussion of the measurements are important for the validation understanding.
A full documentary of this storage prototype can be found in [28].

Storage design

The storage design consists of an insulated steel container equipped with a fin-and-tube heat exchanger. The phase change phenomena is of the type solid-liquid with high density polyethylene (HDPE) used as phase change material. The thermal oil Marlotherm SH is used as heat transfer fluid.
The heat exchanger consists of 301 parallel aluminum fins. The thickness of the fins is 0.25 mm and the fin-to-fin spacing is 8 mm. The fins are attached to 72 tubes made of steel, which are arranged in the storage as shown in figure 2.4. 30 cm of mineral wool is used as insulation material. The storage has a total length of 3.4 m and a weight of 370 kg without PCM. The storage was filled with 170 kg of HDPE pellets (figure 2.5) [28].

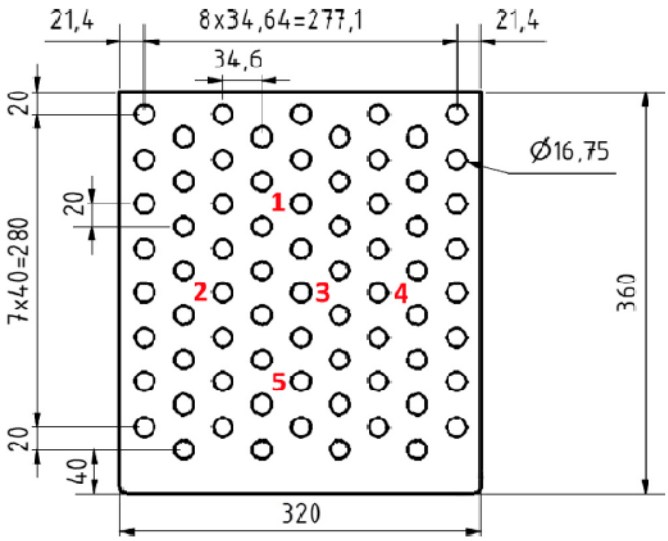

Figure 2.4: Arrangement of the steel tubes. At positions 1–5 thermocouples were immersed within the PCM.

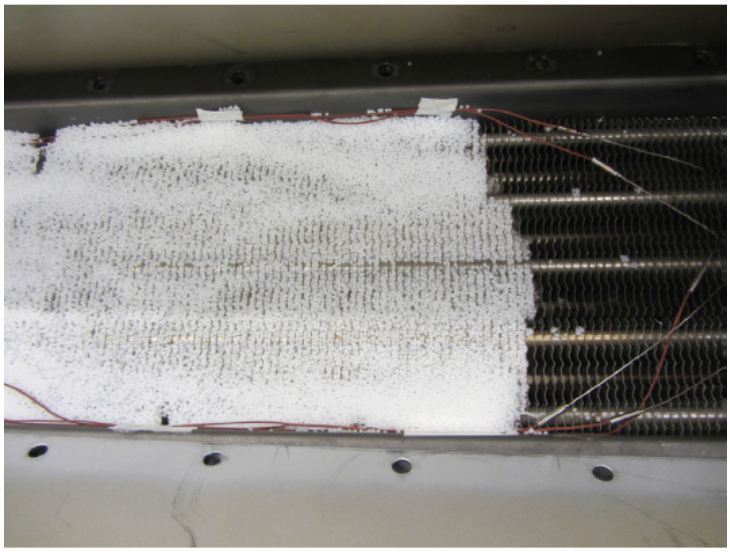

Figure 2.5: HDPE pellets poured into the storage

Figure 2.6 shows the top surface of the full storage in solid phase. Deformation of the fins results due to the thermal expansion of the PCM during melting and crystallization [28].

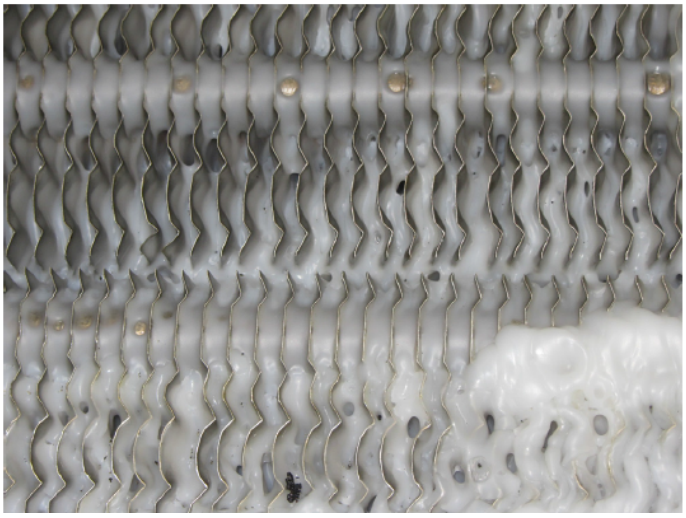

Figure 2.6: Top surface of the full storage in solid state. Deformation of the fins can be observed

Polymers as phase change materials

Polymers as phase change materials have rarely been used in latent heat storages up to now. However, this material class has some interesting advantages [28]:

- Large industrial availability ensuring high material quality
- Low material prize, especially for commodity plastics
- An existing professional recycling industry causing further material cost reduction
- Chemical and physical properties can be modified by compounding additives into the raw polymer

Especially **high density polyethylene (HDPE)** turned out to be suitable for this application frame because of its high enthalpy, prize and large-scale availability [28].

Experimental setup

To characterize the storage, it was connected to a thermostat (Lauda ITH350). Inlet and outlet temperatures were measured using resistance thermometers and the mass flow was recorded with a clamp-on ultrasonic flow meter (Flexim Fluxus F601). The PCM temperatures were measured by thermocouples in four equidistant layers along the length-axis of the storage, each layer contains 5 sensors as illustrated in in figure 2.4 [28].

Figure 2.7 shows measurement results where the storage was charged from 105 °C to 155 °C and discharged from 155 °C to 105 °C at a constant mass flow of 0.41 kg/s.
The resulting plateaus, which are typical for a LHTES, at the melting temperature can clearly be observed [28].

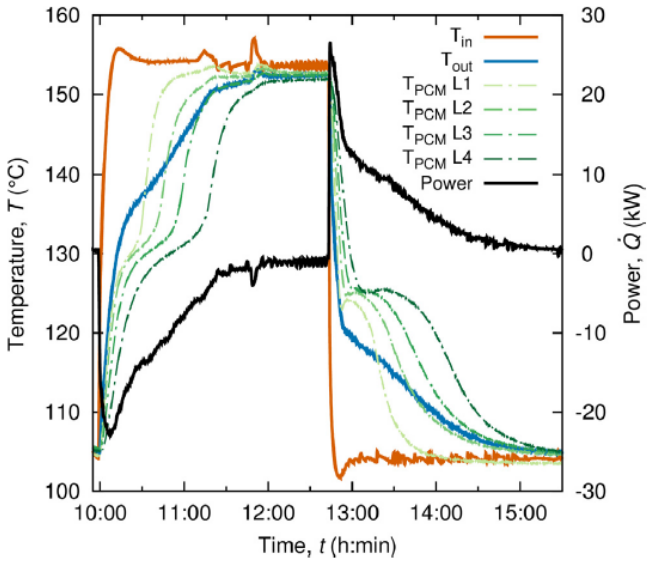

Figure 2.7: Temperatures and calculated power profiles for a thermal oil mass flow of 0.41 kg/s. A full charging followed by a discharging process have been realized

It is interesting to compare the melting and crystallization behaviour resulting from DSC measurements performed at different heating and cooling rates. The results are shown in figure 2.8. The subcooling effect, introduced in section 2.1.4, can be clearly observed, due to difference in the phase change temperature depending on heating or cooling process. Also a reduction of the apparent specific heat peaks can be observed during the heating process [28].

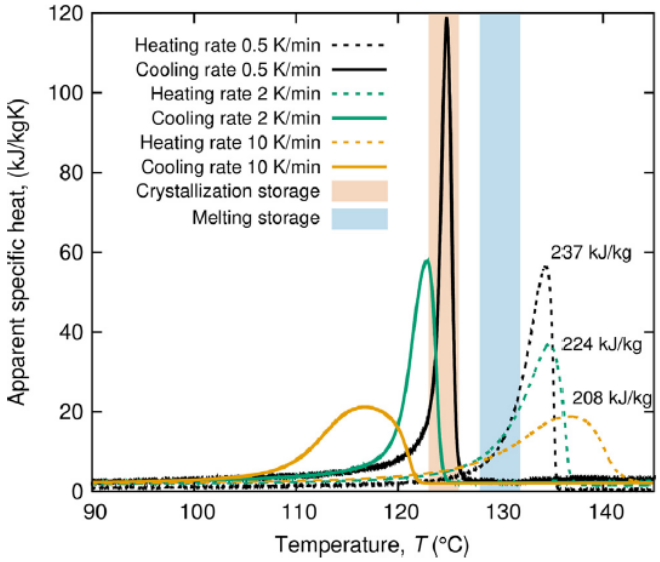

Figure 2.8: DSC measurements of HDPE for different heating and cooling rates compared to the melting and crystallization ranges of the prototype storage. Due to subcooling, a difference in the phase change temperature depending on the process type and rate can be observed

2.2 ThermoCycle Modelica library

The PCM storage model developed in this work is based on basic Modelica models from the *ThermoCycle* library. In the following the concepts of this library will be introduced.

ThermoCycle is an open Modelica library for the simulation of low-capacity thermodynamic cycles and thermal systems. Special attention is paid on robustness and simulation speed [23].
Particular attention is paid on the following three typical challenges typical for thermo-flow system simulation. [23]:

- Computational efficiency
- Robustness during initialization and integration

The thermophysical properties are computed using the open-source thermodynamic properties database *Coolprop*. The interface between CoolProp and

Modelica is based on the *Coolprop2Modelica* library, a modified version of the ExternalMedia library [23] [2].

The intention of the library is to furnish a entirely open-source solution for the computation of thermophysical substance properties, using CoolProp, and the simulation of complex thermodynamic systems with their control strategy. Compared to similar libraries used in the modelling of thermo-flow systems as for example *ThermoPower* or *ThermoSysPro*, the ThermoCycle library contains diverse models dedicated to the model small-scale thermal systems, such as volumetric compressors used in simulations of heat pump or refrigeration cycles.
The key features of the library are the following [23]:

- Designed for system level simulations
- Full compatibility with other Modelica libraries due to the use of stream connectors
- Ability to handle reverse flows and flow reversals
- Various numerical robustness strategies implemented in the components and accessible through Boolean parameters
- Limited levels of hierarchical modelling causing high model readability

The components provided in the library are designed to be as generic as possible [23].
The full documentation of the ThermoCycle library can be found in [23].

2.3 Application: BRICKER CSP-biomass plant

The PCM storage model developed in this work is integrated into a practical application to analyse the resulting differences in terms of system behaviour. Especially thermal solar plants can increase their efficiency by using a thermal storage dedicated to balance the differences between supply and demand of solar power. A review of different types of thermal storages used in high temperature solar plants for power generation can be found in [20].
The use of a PCM storage gives the advantage of a lower storage volume due to the high energy density and a nearly isothermal storage outlet temperature profile (see section 2.1.5). Latter argument is beneficial for system component needing constant supply temperatures, as for example ORC power generators. Furthermore, the investment costs for a PCM storage are possibly lower than for sensible large thermal-oil tanks or molten salt storages.

2.3.1 Generalities

In the last decades, concentrated solar power (CSP) systems have been increasingly considered worldwide as a key technology for meeting the renewable energy demand [12]. The total current CSP capacity is still small due to the large investment costs. Only 3.6 GW_{el} were installed by the end of 2013 [12]. One approach to attain competitiveness to other power plants systems consists in hybridization with a second source of energy [12]. It has not only the benefit of a cost reduction but it also provides thermal power continuity when the solar source is unavailable during night or on cloudy day. Several plants worldwide have demonstrated the advantages of this solution [12]. In regard of the renewable power generation, the hybridization of CSP technology with biomass has gained attention. Recently, CHP systems using organic Rankine cycle (ORC) technology integrated with an hybrid CSP-biomass heat source, have been investigated [12]. In order to stimulate the development of such technologies, the European Union founded the BRICKER project. It aims to develop a scalable, replicable, high energy efficient, zero emissions and cost effective CSP-Biomass trigeneration system, based on ORC technology, to refurbish existing public-owned non-residential buildings. The CHP unit together with lightweight facades, and phase change material insulation technology, is expected to reduce the building energy consumption by at least 50 % [1]. Three systems are being developed in Spain,

Belgium and Turkey to demonstrate the concept feasibility [12]. The system presented in this work is situated in Cacares, Spain.

2.3.2 System background

As introduced in section 1.2, the system consists in a solar power (CSP) biomass combined heat and power (CHP) system based on organic Rankine cycle (ORC) technology, developed for building applications.
The system is composed by two main loops as shown in figure 2.9.
The first loop contains 4 mains components:

- Solar field (SF)
- biomass combustion boiler (BMB)
- Oil-water heat exchanger (HXI)
- ORC power block

Referring on figure 2.9, the heat transfer fluid is first preheated through the parabolic solar collectors of the solar field (a to b), characterized by a total collector area of $54\,\mathrm{m}^2$ [12].
The thermal oil *TherminolSP*, is selected as heat transfer fluid. It is mainly used for CSP applications thanks to its low operating pressure, high thermal stability (up to $335\,^{\circ}\mathrm{C}$) and good heat transfer characteristics[12].
The preheated HTF (thermal oil) is heated up the nominal ORC temperature in a biomass combustion boiler (d to e). It is then transferred to the ORC system for electricity production (h) and to the oil-water heat exchanger (f to g) delivering additional heat to the second loop [12].

Loop II comprises following components:

- Absorption chiller
- ORC condenser cooling side
- Secondary side of HXI
- Connection to the thermal load of the building

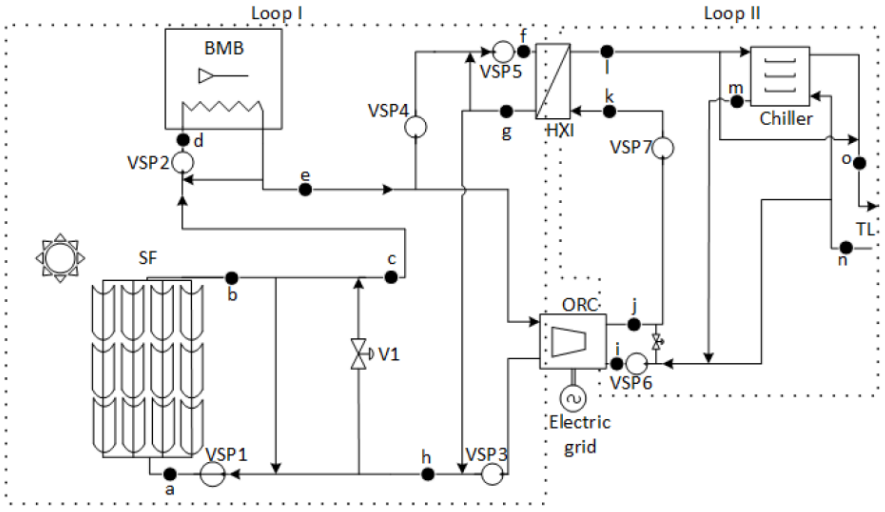

Figure 2.9: Schematic flow diagram of the Bricker CHP system

Focusing on the righ part of figure 2.9, the heat transfer fluid is first pre-heated in the ORC condenser from (i) to (j), and then it is pumped through HXI from (k) to (l) where it reaches the maximum temperature of loop II. In the second loop water is used as heat transfer fluid. The hot water is then directed to the Chiller or directly to the building depending on the thermal demand [12].

2.3.3 Control strategy

The following control strategy ensures that all components are operated within their admissible limits. Several points have to be taken into account [12]:

- **Solar field**: To avoid deterioration of the thermal oil, the temperature through the parabolics are limited by the maximal thermal oil temperature.
- **Biomass boiler**: The power range of the boiler is between 150 and 500 kW. Automatic shut-down occurs if the the thermal power supply falls below 150 kW. The system operates at constant mass flow of 9.5 kg/s. To keep the temperature at the outlet at the set-point, a

recirculation circuit and an internal control which regulates the amount of biomass burned is implemented.

- **ORC unit**: A constant temperature at the evaporator of 245 °C with a maximal deviation of 20 K as well as constant mass flow of 2.5 kg/s is required.

- **Absorption chiller**: As for the ORC system, a constant supply temperature with a maximal deviation of 5 K can be handled. A proper control of the oil-water heat exchanger is required to respect the boundaries.

In general, high control of the solar field is needed to insure safe biomass boiler operation in order to avoid a biomass shut-down. As shown in figure 2.9, The solar field is equipped with a recirculation and a bypass stream to reach this objective. The fluid valve regulating the mass flow in the bypass stream is controlled by the boiler inlet temperature. The bypass is activated if the biomass supply temperature exceeds the maximal temperature leading to shut-down. By activating the solar field bypass, the thermal oil recirculates in the collectors tubes due to the pump VSP1 which circulates at constant mass flow [12].
When the outlet temperature of the solar field overpasses the set-point, automatic defocusing of the parabolic collectors occurs, reducing the solar power generation [12].
In the case, the heat rejected from the ORC's condenser is not sufficient to satisfy the thermal load of the building, extra power has to be supplied to the second loop via the additional oil-water heat exchanger HXI. A temperature sensor in point (l) controls heat exchange rate in HXI via pump VSP4 in order to respect the set point for the absorption chiller supply. Using VSP5 at constant speed in combination with a recirculation circuit, constant mass flow in HXI is obtained [12].

Chapter 3

Numeric modelling

3.1 Discretized PCM storage model

In the following a white-box discretized model of the shell and tube LHTES described in section 2.1.7 is presented. It is a white box model based on physical material parameters and heat transfer processes. All simulated variables represent realistic physical values.
The model considers convective heat transfer between HTF and the tube wall, heat conduction in axial direction in the tube, heat exchange with the PCM and thermal conduction in radial and axial direction inside the PCM. The phase change phenomena is modelled using an apparent heat capacity method with two different models [25]. It describes the specific heat capacity of the PCM as a function of temperature with a significant increasing around the melting temperature. A detailed method description can be found in section 3.1.3.
For all tubes, equal mass flow of the HTF and equal temperature distribution on the shell and tube side has been considered. Therefore, only one tube is considered in the model and boundary effects near to the limit of the storage device, e.g. energy losses to the surrounding, are ignored [25]. The aluminum fins are taken into account only indirectly by an increase in the thermal conductivity of the PCM. Concerning the thermal capacity of the fins, it is lumped into the thermal capacity of the tube wall.

Figure3.1 schematizes the main ideas of the model set-up. The storage is divided into equal cuboids, one for each HTF tube, see sub-figure (1). As

already mentioned above, the model considers only one tube. The next step consists in the conversion of the rectangular PCM block into a cylinder (2), which is then discretized in radial and axial direction (3).

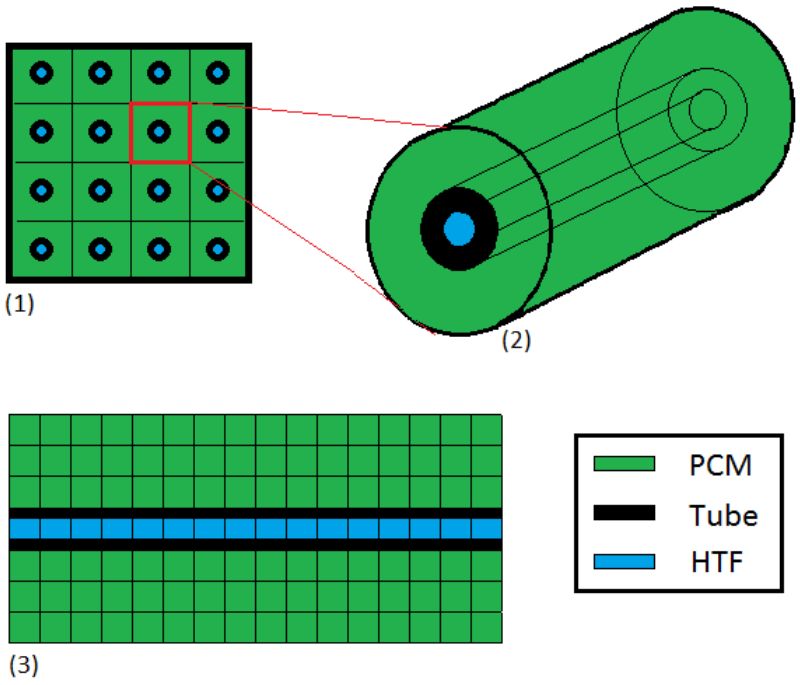

Figure 3.1: Schemata of the modelling idea: (1) Subdivision of the storage in equal cuboids, (2)Conversion from cuboid to cylinder, (3)Discretization in radial and axial direction

3.1.1 Heat transfer fluid (HTF) model

The forced convective mass flow of the HTF in the tube is modelled in the axial direction x. Heat transfer to the tube inner wall is considered only. Radial fluid flow, axial heat conduction in the fluid, viscous dissipation, external forces and compressibility have been neglected [10] [25]. The internal energy equation in Eq. (3.1) is expressed in terms of HTF temperature T_H with $du = c_p(T)dT$ using specific heat capacity for incompressible fluids $c_p \approx c_v$.

$$\rho_H c_{p,H} \frac{\partial T_H}{\partial t} = -v_H \rho_H c_{p,H} \frac{\partial T_H}{\partial x} - \frac{2}{r_{in}} \dot{q}_H \tag{3.1}$$

The initial and boundary conditions for Eq. (3.1) are:

$$T_H(t = 0, x) = T_H^0(x), \quad T_H(t, x = 0) = T_H^{su}(t) \tag{3.2}$$

Furthermore, the fluid velocity v_H depends on the mass flow $\dot{m}_{H,total}$:

$$v_H = \frac{\dot{m}_{H,total}}{n_T \pi (r_{in})^2 \rho_H} \tag{3.3}$$

It has to be noted that in Eq. (3.1) density changes, induced by local temperature changes, are neglected [25]. In Eqs. (3.1) and (3.3), r_{in} presents the tube inner radius.

Heat transfer

$\dot{q}_H$ represents the heat flux density, i.e. the heat transfer from fluid to the tube. $\dot{q}_H$ is calculated using the heat transfer coefficient U:

$$\dot{q}_H = U(T_H - T_W) \tag{3.4}$$

In Eq. (3.4), T_H and T_W are the HTF and inner tube wall temperatures at the axial position x, respectively. The heat transfer coefficient U is calculated from the dimensionless numbers and correlations for forced convective heat transfer inside a tube introduced below [26] [25].

$$\mathrm{Nu} = \frac{U \cdot d_{in}}{\lambda_H}, \quad \mathrm{Re} = \frac{\dot{v}_H \cdot d_{in}}{\nu_H}, \quad \mathrm{Pr} = \frac{\nu_H \cdot \rho_H \cdot c_{p,H}}{\lambda_H} \tag{3.5}$$

In Eq. (3.5), $d_{in} = 2r_{in}$, λ_H is the thermal conductivity and ν_H is the kinematic viscosity of the HTF. Except for $\rho_H(T)$ all other HTF properties are temperature dependent. The corresponding correlations are given in Eqs.(3.6) to (3.9) where T is the temperature in $[°C]$ [25].

$$\rho_H = c_1 T + c_2 \quad [kg/m^3], \quad with \quad c_1 = -0.71482,\ c_2 = 1058.4 \tag{3.6}$$

$$c_{p,H} = c_1 T + c_2 \quad [J/kgK], \quad with \quad c_1 = 3.7263,\ c_2 = 1474.5 \tag{3.7}$$

$$\lambda_H = c_1 T + c_2 \quad [W/mK], \quad with \quad c_1 = -0.00013184,\ c_2 = 0.13326 \tag{3.8}$$

$$\mu_H = c_1 T^{-c_2} \cdot 10^{-6} \quad [m^2/s], \quad with \quad c_1 = 10113,\ c_2 = 1.755 \tag{3.9}$$

The coefficients result from a fitting of the HTF thermophysical properties to measured data taken from product information.

The local Nusselt number for fully developed turbulent flow with $\mathrm{Re} \geq 10^4$ is [26]:

$$\mathrm{Nu}_x = \frac{(\xi/8)\mathrm{Re}\,\mathrm{Pr}}{1 + 12.7\sqrt{\xi/8}(\mathrm{Pr}^{2/3} - 1)} \left[1 + \frac{1}{3}(d_{in}/x)^{2/3}\right] \tag{3.10}$$
$$with \quad \xi = (1.8\, log_{10}\mathrm{Re} 11.5)^{-2}$$

The local Nusselt number at any point x in a pipe with laminar flow ($\mathrm{Re} \leq 2300$) reads [26]:

$$\mathrm{Nu}_{x,T} = \left\{ (3.66)^3 + (0.7)^3 + \left[1.077\sqrt[3]{\mathrm{Re}\,\mathrm{Pr}(d_{in}/x)} - 0.7\right]^3 + \left[\frac{1}{2}\Big(\frac{2}{1 + 22\mathrm{Pr}}\Big)^{1/6} (\mathrm{Re}\,\mathrm{Pr}\, d_{in}/x)^{1/2}\right]^3 \right\}^{1/3} \tag{3.11}$$

In the transition region between laminar and turbulent flow with $2300 \leq \mathrm{Re} \leq 10^4$ the local Nusselt number is:

$$\begin{aligned} \mathrm{Nu} &= (1-\gamma)\mathrm{Nu}_{lam,2300} + \gamma \mathrm{Nu}_{turb,10^4} \\ with \quad \gamma &= \frac{\mathrm{Re}-2300}{10^4-2300}, \quad 0 \leq \gamma \leq 1 \end{aligned} \tag{3.12}$$

In Eq. (3.12), the local value of $\mathrm{Nu}_{lam,2300}$ is calculated using Eq. (3.11) with Re=2300 and $\mathrm{Nu}_{turb,10^4}$ is calculated from Eq. (3.10) with Re=10^4.

Implementation in Modelica

The introduced HTF model is translated into the Modelica laguage by using the numeric modelling environment *Dymola*.
Figure 3.2 shows the HTF cell build with elements of the ThermoCycle library.

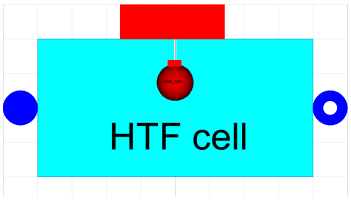

Figure 3.2: HTF cell in Dymola

It is based on the 1-D incompressible fluid flow model of the ThermoCycle library. No marginal changes have been done on the original model, except that the calculation for the mass flow velocity (see Eq. (3.3)) was added. The HTF cell uses a new heat transfer model, named `Tube_heat_transfer`, regrouping the heat transfer equations (3.4),(3.5),(3.10),(3.11),(3.12).

A new media model, called `HTF` was created in order to implement the thermophysical properties of the Marlotherm SH fluid, introduced in equations (3.6) to (3.9).
It extends the *PartialMedium* interface of the Modelica library. Also the calculation of the *state of charge*, introducing in section 3.1.5, is implemented in the HTF media model.

3.1.2 Tubes and fines models

The wall temperature T_W is modelled assuming a constant temperature in radial direction, so that there is no temperature gradient in the tube wall in radial direction. Heat conduction in axial direction and heat transfer at the inner and outer tube wall are considered only.
The internal energy equation, Eq. (3.13), is expressed in terms of the tube wall temperature T_W and the inner energy $du = c_p(T)dT$ [25].

$$(A\rho c_p)_W \frac{\partial T_W}{\partial t} = A_T \frac{\partial}{\partial x}\Big(\lambda_T \frac{\partial T_W}{\partial x}\Big) + 2\pi(r_{in}\dot{q}_H - r_{out}\dot{q}_P) \tag{3.13}$$

The initial and boundary conditions are:

$$T_W(t=0,x) = T_W^0(x), \quad \lambda_T \frac{\partial T_W}{\partial x}\bigg|_{t,x=0} = 0, \quad \lambda_T \frac{\partial T_W}{\partial x}\bigg|_{t,x=L} = 0 \tag{3.14}$$

The heat capacity of the fins is added to the heat capacity of the tube wall: $(A\rho c_p)_W = (A_T\rho_T c_{p,T} + A_F\rho_F c_{p,F})$, with the subscripts T and F indicating the tube and fin, respectively. A_T and A_F are the corresponding cross-sectional areas. In Eq. (3.13), λ_T corresponds to the thermal conductivity coefficient of the tube, $\dot{q}_H$ and $\dot{q}_P$ represent heat flux densities from the HTF to the tube inner wall (see Eq. (3.4)) and from the wall to the PCM (see Eq. (3.15)), respectively. Finally, r_{in} is the inner and r_{out} the outer tube radius.

$$\dot{q}_P = \lambda_P \frac{\partial T_P}{\partial r}\bigg|_{r=r_{out}} \tag{3.15}$$

All properties are temperature dependent with correlations given in Eqs. (3.16)-(3.18). TThe coefficients have been determined by fitting the properties to measured data from hf-DSC and Laser Flash Analysis [25]:

$$\rho_T = c_1 T + c_2 \quad [kg/m^3], \quad with \quad c_1 = -0.3067,\ c_2 = 7718.19 \tag{3.16}$$

$$c_{p,T} = c_1 T + c_2 \quad [J/Kg/K], \quad with \quad c_1 = 0.4188,\ c_2 = 338.96 \tag{3.17}$$

$$\lambda_T = 50 \quad [W/m/K] \tag{3.18}$$

Implementation in Modelica

Figure 3.3 shows the tube wall cell model in Dymola environment.

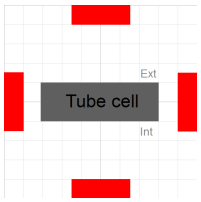

Figure 3.3: Tube wall cell in Dymola

The tube wall cell possess four heat ports for the heat transfer in radial (top and bottom port) and axial (right and left port) direction. The component is based on the `MetalWallL` model of the ThermoCycle library, representing a lumped tube of solid material.
Axial conductive heat transfer described by λ_T has been added. Therefore Eq. (3.13) is discretized in axial direction using a central difference scheme.

Figure 3.4 schematizes the discretization of the tube wall.

The resulting heat flux in axial direction is given by Eq. (3.19):

$$\dot{q}_{W,ax}^{i,i+1} = \frac{\lambda_T}{\Delta x/2}(T_W^{i,i+1} - T_W^i) \quad with \quad \Delta x = l_{cell} = \frac{l_{hex}}{N_{ax}} \tag{3.19}$$

Where l_{hex}, the total length of the heat exchanger tube and N_ax the discretization rate or number of cells in axial direction.

In addition to the heat transfer, calculations for the heat exchange surfaces of the tube wall have been added. There are three exchange surfaces:

- $A_{rad,in}$: Inner tube surface, used for radial heat transfer HTF-Tube

$$A_{rad,in} = \pi \cdot d_{in} \cdot l_{cell} \tag{3.20}$$

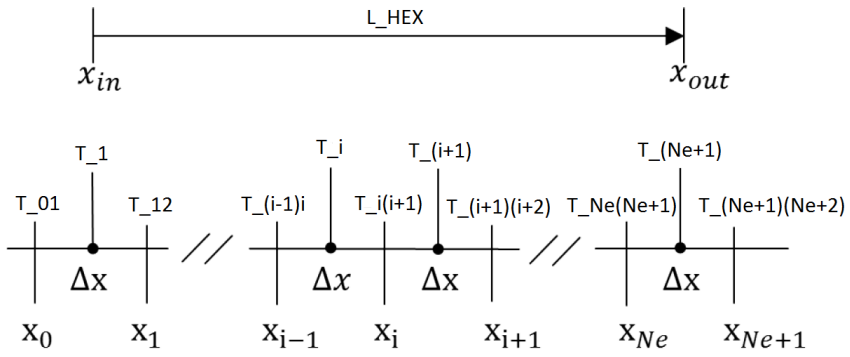

Figure 3.4: Discretization scheme for the tube wall

- $A_{rad,out}$: Outer tube surface, used for radial heat transfer Tube-PCM

$$A_{rad,out} = \pi \cdot d_{out} \cdot l_{cell} \tag{3.21}$$

- A_{ax}: Axial cross section, used for axial heat conduction in the tube wall

$$A_{ax} = \pi \cdot (\frac{r_{out}{}^2}{2} - \frac{r_{in}{}^2}{2}) \tag{3.22}$$

To be able to compute the thermophysical properties of the tube wall material, Eq. (3.16),(3.17) and (3.18) are included in this model.

3.1.3 Phase change material (PCM) model

It is assumed that the phase change transport phenomena in the PCM is controlled by conduction in radial and axial direction. Moreover, the fins reaching into the PCM are considered only indirectly by an increase of the thermal conductivity of the PCM resulting in an effective thermal conductivity λ_P. It consists in a volume weighted avarage value of the fin and PCM conductivity. By using the apparent heat capacity method, an explicit treatment of the phase change moving boundary is avoided [25]. A temperature interval for the phase change is considered and a transition zone has been defined. Mixed material properties with a smooth transition between phases (solid, mushy and liquid) have been applied afterwards. Whereas thermal

conductivity and heat capacity are considered to vary with phases and temperature, constant density has been assumed. Thus, material velocity due to density changes and their impact on the integration domain can be neglected [25].

The internal energy equation for the PCM is expressed in terms of the PCM temperature T_P and the apparent heat capacity as shown in Eq. (3.23 with $du = \tilde{c}_P(T)dT$. Thermal conduction in the PCM around the tube is considered in radial and axial direction. For temperature dependent λ_P and $\tilde{c}_P$, we obtain in cylindrical coordinates [9][6]:

$$\rho_P \tilde{c}_P \frac{\partial T_P}{\partial t} = \frac{1}{r}\frac{\partial}{\partial r}\Big(r\lambda_P \frac{\partial T_P}{\partial r}\Big) + \frac{\partial}{\partial x}\Big(\lambda_P \frac{\partial T_P}{\partial x}\Big) \tag{3.23}$$

A cylindrical PCM domain is considered ranging from the outer tube radius r_{out} to r_{end}. The latter is determined from the cross-section of the storage filled with PCM [25]:

$$r_{end} = \sqrt{A_{ap}/N_{tube}/\pi + r_{out}^2} \tag{3.24}$$

Eq. (3.23) is solved with the following initial and boundary conditions:

$$\begin{gathered} T_P(t=0,r) = T_P^0(r), \quad T_P(t, r=r_{out}) = T_W(t), \\ \lambda_P \frac{\partial T_P}{\partial r}\bigg|_{t,r=r_{end}} = 0, \quad \lambda_P \frac{\partial T_P}{\partial x}\bigg|_{t,x=0} = 0, \quad \lambda_P \frac{\partial T_P}{\partial x}\bigg|_{t,x=l_{hex}} = 0 \end{gathered} \tag{3.25}$$

The PCM properties ρ_P and λ_P change significantly for solid and liquid phase. However, in the model ρ_P is set to 850 kg/m^3 (density variations neglected). The correlation for λ_P is given in Eq. (3.26). To determine the correlation coefficients, PCM material properties have been
fitted to measured data from hf-DSC and laser flash analysis [25].

$$\begin{gathered} \lambda_P = \frac{c_1}{1+\exp(c_4(T-c_2))} + c_3 \quad [W/m/K] \\ with \quad c_1 = 0.41857,\ c_2 = 96.162,\ c_3 = 0.15406,\ c_4 = 0.036647 \end{gathered} \tag{3.26}$$

The correlation for the apparent specific heat capacity $\tilde{c}_P(T_P)$ reads:

$$\tilde{c}_P = 1000(c_{p,P} + b_1\phi), \quad with \quad c_{p,P} = a_0 + a_1 T_P \tag{3.27}$$

$\tilde{c}_P(T_P)$ is modelled using a combination of a linear term for the specific caloric heat $c_{p,P}(T_P)$ and a distribution function $\phi(T_P)$ for the specific latent heat. Two different functions have been considered:

1. Normal (Gaussian) function, with the peak position at μ and width σ
2. Sigmoid function, where T_m is the peak location parameter and ΔT the peak width

Normal function

The first model *(Mod1)* uses a normal distribution for the specific latent heat model:

$$\phi(T) = \frac{1}{\sigma\sqrt{2\pi}} exp(-\frac{(T-\mu)^2}{2\sigma^2}) \tag{3.28}$$

Figure 3.5 shows the normal function and the corresponding apparent specific heat capacity parameters of *Mod1*, see Eq.(3.27) and (3.28).

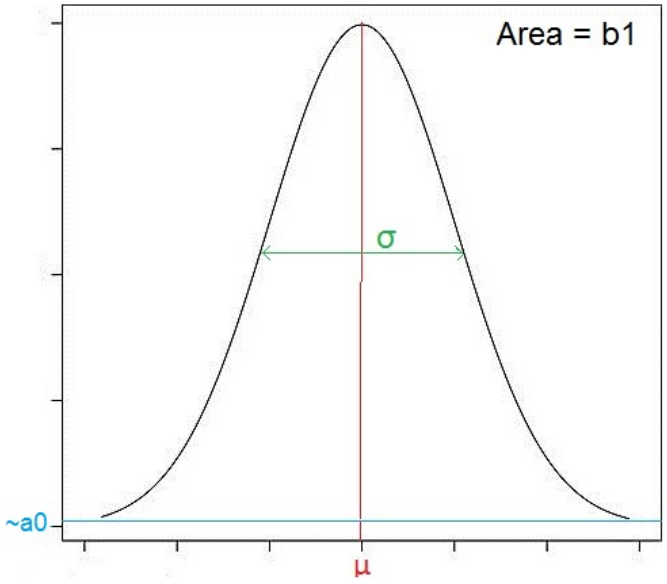

Figure 3.5: Normal function and parameters of *Mod1*

Sigmoid function

In the second model the specific latent heat is characterized by the sigmoid function (3.29), using the parameter L, which is the latent heat of the material, `width_T` (or ΔT), the transition width of the specific heat capacity peak and T_m, the melting temperature of the PCM.

$$\phi(T) = L\frac{ae^{-a(T-T_m)}}{(1+e^{-a(T-T_m)})^2} \tag{3.29}$$

The transition width ΔT is defined by

$$a = -\frac{2}{\Delta T}\ln(\frac{1-f}{f}) \tag{3.30}$$

So that at the temperature $T_m + \Delta T/2$ only a fraction of f=1/100 of the PCM is still in the solid state [15].

Figure 3.6 represents the sigmoid function and the corresponding apparent specific heat capacity parameters of *Mod2*.

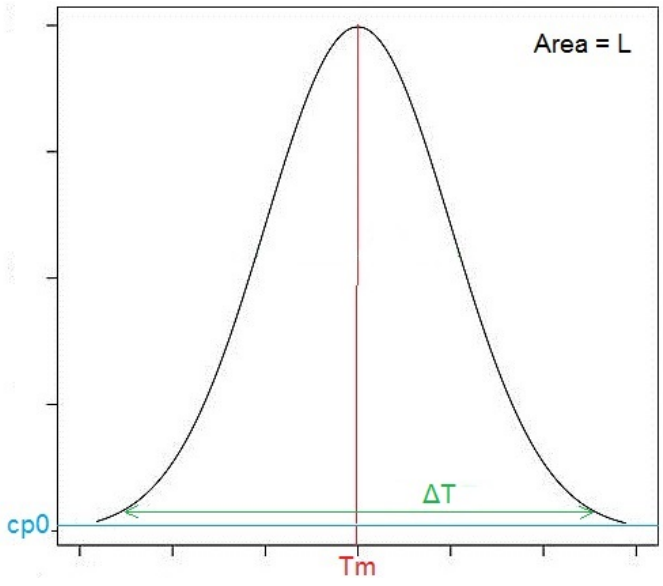

Figure 3.6: Sigmoid function and parameters of *Mod2*

Implementation in Modelica

Figure 3.7 shows the PCM cell model in the Dymola interface.

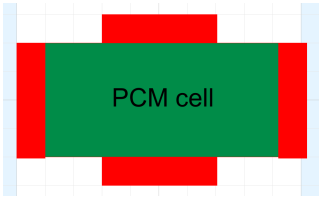

Figure 3.7: PCM cell in Dymola

The PCM cell possesses four heat ports for the heat transfer in radial (top and bottom port) and axial (right and left port) direction. Unlike the tube wall model, heat conduction in radial direction is considered. Therefore Eq. (3.23) is discretized not only in axial but also in radial direction. The axial discretization has been taken from the tube wall discretization, see Eq. (3.19), where λ_T is replaced by λ_P.
A scheme of the radial discretization is shown in figure 3.8.

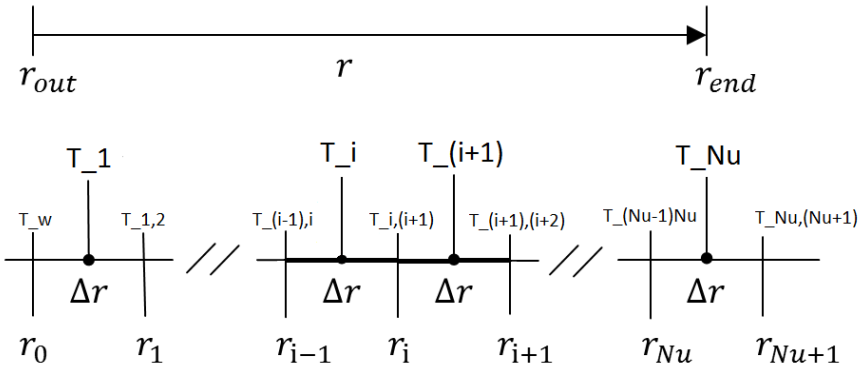

Figure 3.8: Radial discretization scheme

The PCM cell width in radial direction is given by

$$\Delta r = r_{out} - r_{in} \tag{3.31}$$

As the temperatures T_i are located in the geometrical centre of the PCM cell, the conductive heat fluxes in radial direction are:

$$\dot{q}_{P,rad}^{i-1,i} = \frac{\lambda_P}{\Delta r/2}(T_P^{i-1,i} - T_P^i) \tag{3.32}$$

$$\dot{q}_{P,rad}^{i,i+1} = \frac{\lambda_P}{\Delta r/2}(T_P^{i,i+1} - T_P^i) \tag{3.33}$$

with $q_{P,rad}^{i-1,i}$ corresponds to the heat flux between the cell centre and the inner radius, $q_{P,rad}^{i-1,i}$ relates the centre to the outer cell radius.

The axial conductive heat flux is of the same form as for the tube wall cell, described in Eq. (3.19).

Finally, the heat exchange surfaces are the following:

$$A_{rad,out} = 2 \cdot \pi \cdot r_{out} \cdot l_{cell} \tag{3.34}$$

$$A_{rad,in} = 2 \cdot \pi \cdot r_{in} \cdot l_{cell} \tag{3.35}$$

$$A_{ax} = \pi \cdot (r_{out}^2 - r_{in}^2) \tag{3.36}$$

The energy balance, see Eq.(3.23) on the PCM cell in Dymola is of the form:

$$V_{cell} \cdot \rho_P \cdot c_{p,P} \cdot \frac{d}{dt}T = \dot{Q}_1 + \dot{Q}_2 + \dot{Q}_3 + \dot{Q}_4 \tag{3.37}$$

where $\dot{Q}_1$ and $\dot{Q}_2$ are the heat transfer rates transferred to the outer and inner radial surface and $\dot{Q}_3$ and $\dot{Q}_4$ the thermal powers transferred to the right and left axial surfaces, respectively. They are calculated using the heat flux of the corresponding direction (see Eq (3.32) and (3.33)), multiplying it with the respective heat exchange surface (Eq. (3.34) to (3.36)).

3.1.4 Stored energy

The total stored energy Q_{stored} absorbed or released by the storage between time $[t_0; t]$ is obtained from the solution of the differential equation [25]:

$$\frac{dQ_{stored}}{dt} = \dot{m}_{H,total} \int_{T_H(x=0)}^{T_H(x=L)} c_{p,H}(T)dT, \quad Q_{stored}(t=0) = Q^0_{stored} \tag{3.38}$$

with Q^0_{stored} being the initial absorbed energy at time t=0.

3.1.5 State of charge

The state of charge (SOC) is a parameter which indicates the extend to which a LHTES is charged relative to storable latent heat [25]. The values for SOC range from 0 to 1 with 1 meaning the PCM is fully molten and 0 corresponds to solid PCM only. The local $SOC(T_P)$ is obtained from the integration of the latent heat $\phi(T_P)$ in Eq. (3.27) [25].

$$SOC(T_P) = \int_{-\infty}^{T_P} \phi(T)dT \quad with \quad \int_{-\infty}^{+\infty} \phi(T)dT = 1 \tag{3.39}$$

In time domain we get:

$$\frac{\partial SOC(T_P)}{\partial t} = \frac{\partial SOC(T_P)}{\partial T_P}\frac{\partial T_P}{\partial t} = \phi(T_P)\frac{\partial T_P}{\partial t} \tag{3.40}$$

With T_P and SOC being functions of r and x, the global SOC_{tot} of the complete storage is computed as mean value by integration in radial and axial direction [25].

$$\frac{dSOC_{tot}}{dt} = \frac{\int_0^L \int_{r_{out}}^{r_{end}} \frac{\partial SOC(T_P)}{\partial t} r \, dr \, dx}{\int_0^L \int_{r_{out}}^{r_{end}} r \, dr \, dx}, \quad SOC_{tot}(t=0) = SOC^0_{tot} \tag{3.41}$$

with SOC^0_{tot} being the initial state of charge at time $t = 0$.

Case of the Sigmoid function

The Sigmoid function has the benefit that its integral is given by an analytic expression. As the integral of the specific latent heat gives the state of charge (see Eq. (3.39)), we get an analytic expression for the SOC expressed in Eq. (3.42)

$$SOC(T) = \frac{1}{L}\int_0^T \phi(T')dT' = \frac{1}{1+e^{-a(T-T_m)}} \tag{3.42}$$

3.1.6 Model implementation in Modelica

After introducing all the individual components of the PCM storage model, they are connected together composing the final model.
First the components in radial direction are assembled, forming one axial component named `radial_components`. Each is composed of:

- 1 HTF cell
- 1 Tube wall cell
- `N_rad` PCM cells

The user of the model specifies at the beginning the number of PCM cells in radial direction, `N_rad`.

Figure 3.9 shows schematically the build up of the component `radial_components` in the Dymola interface.

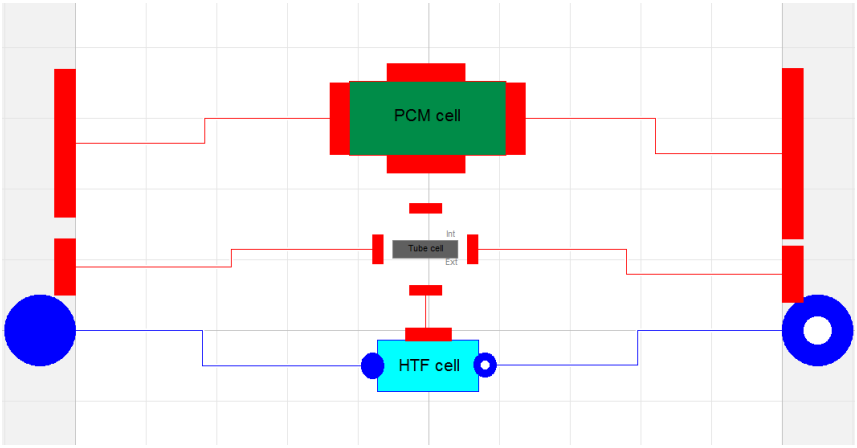

Figure 3.9: Build up of the `Radial_components` model

Figure 3.10 shows the item of the *Radial_components* component.

This axial component possesses several ports:

- 2 fluid ports for the HTF flow

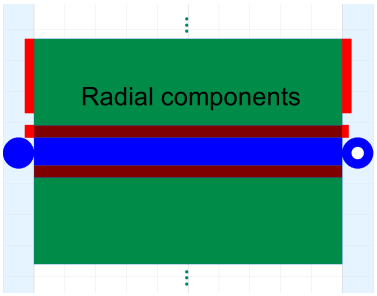

Figure 3.10: `Radial_components` item

- 2 heat ports for the axial heat conduction in the tube wall
- 2*`N_rad` heat ports for the axial heat conduction between the PCM cells

The heat losses to the ambient has been neglected, so no heat port in radial direction has been added.

To take in account the axial discretization, `N_ax` of the axial component, introduced before, are connected in series and building up the final PCM storage model, named `PCM_storage_model`. A schemata is given in figure 3.11.

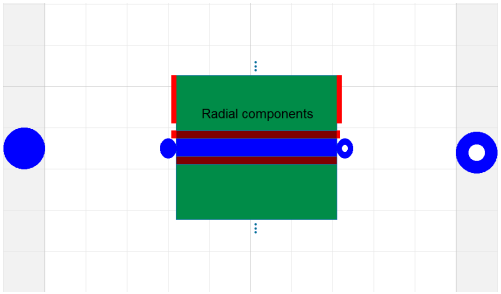

Figure 3.11: Build up of `PCM_storage_model`

Figure 3.12 shows the item of the `PCM_storage_model` component.
It possesses only 2 fluid connectors for the HTF mass flow.

Figure 3.12: `PCM_storage_model` item

3.1.7 Storage parameters

Phase change medium

In section 3.1.3 two different models for the PCM apparent heat capacity has been presented. Each of them possesses a set of parameter used for a later curve fitting for storage validation on experimental measurement data, described in section 4.

Table 3.1 summarizes the parameters for the models 1 and 2. Parameters which are not listed in the table are kept constant.

Geometry

Table 3.2 resumes the geometrical parameters to be provided to the storage model.

Other parameters

Several other parameters have to be provided to the model:

- `HTF`: The user can specify the heat transfer fluid
- `p`: PCM pressure
- `Mdotnom`: Nominal HTF flow rate
- λ_{wall}: Thermal conductivity of the tube wall material, see Eq. (3.18)
- `PCM_cond_ax` (Boolean): If true, the axial PCM conduction is considered

Model 1			
Parameter	Description	Unit	Ref. equation
c2	Characterizes the temperature dependency of the thermal conductivity to the PCM/fins material	-	3.26
c3	Constant term in the thermal conductivity expression of the PCM/fin material	-	3.26
a0	Constant term in the sensible specific heat capacity expression	kJ/kg	3.27
b1	Latent heat of the PCM	kJ/kg	3.27
μ	Melting temperature of the PCM (peak temperature of the normal function)	°C	3.28
σ	Peak width of the normal function	-	3.28
Model 2			
λ_P	Thermal conductivity of the PCM	W/mK	3.26
$c_{p,P}$	Constant term in the sensible specific heat capacity expression	kJ/kg	3.27
L	latent heat of the PCM	kJ/kg	3.31
ΔT	Transition width of the specific heat capacity peak characterised by the Sigmoid function	K	3.32
T_m	Melting temperature of the PCM	°C	3.31

Table 3.1: Parameter summary for the model 1 and 2

Parameter	Description	Unit	Ref. equation
N_{tube}	Number of heat exchanger tubes in the storage	-	3.24
A_{ap}	Inner cross section area of the storage	m^2	3.24
l_{hex}	Total length of the storage heat exchanger	m	3.19
d_{in}	Inner diameter of the HTF tube	m	3.20
d_{out}	Outer diameter of the HTF tube	m	3.21
$A_{fins,tot}$	Total fin area	m^2	//
d_{fins}	Fin thickness	m	//

Table 3.2: Geometrical storage parameters

- `const_U` (Boolean): If set true, the heat transfer coefficient U is considered to be constant. Its value is given by *U_nom*

- `U_nom`: Nominal constant heat transfer coefficient

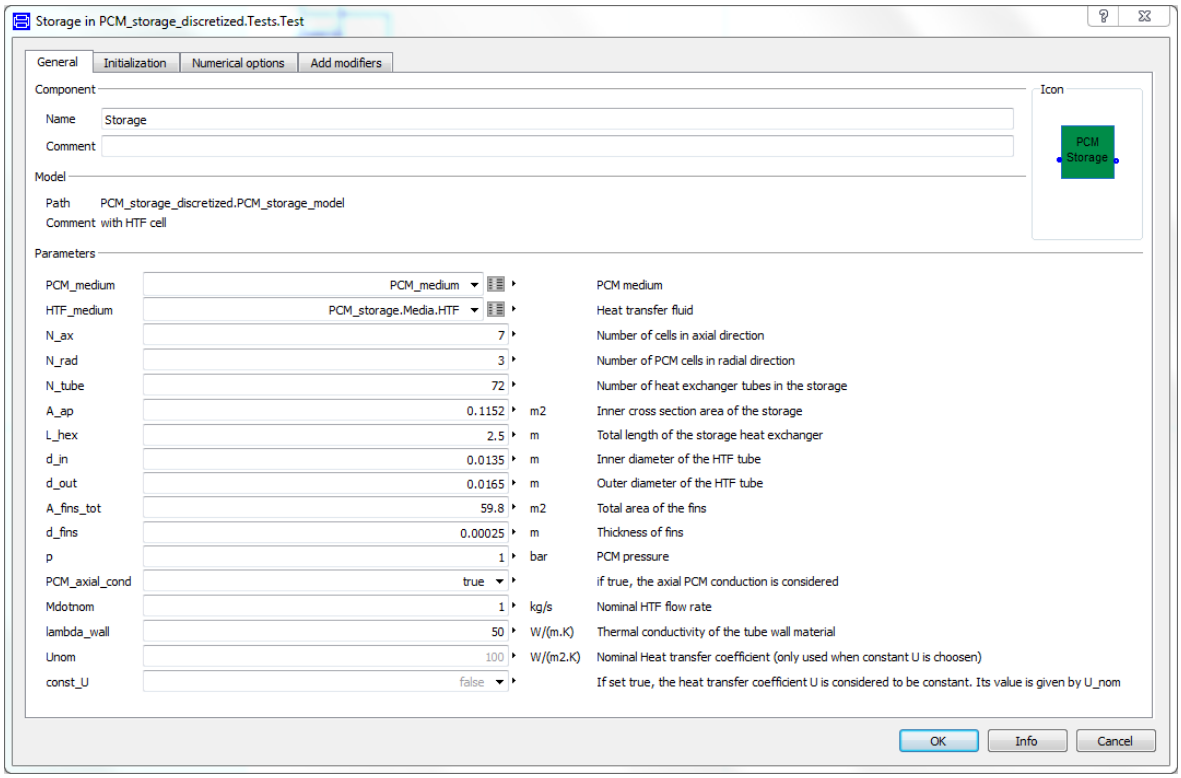

Figure 3.13: Parameter window of the discretized storage model

3.2 Single-node model

This section consists in the presentation of a grey-box single node model of the same LHTES as for the white-box discretized model in the previous chapter.
The difference consists in the fact that for this model, no discretization in axial and radial direction is applied. Therefore, the PCM model is composed of only one axial component modelling the HTF, tube wall, PCM and heat transfer between.

This model consists in a grey-box model, meaning that the simulated thermal variables of the storage as well as the medium storage parameters don't represent the real physical values. The thermophysical processes in the storage interior can't be predicted with this model, so a new storage cannot be designed based on this model.
In the later model validation (see chapter 4.2), the parameters are adapted so as the storage outlet temperature fits the measurement. Other internal thermal characteristics (PCM temperature, etc.) can't be predicted by this model. In this case the discretized model must be used.
The aim was to create a fast, simple and slim model which exterior characteristics (HTF oulet temperature) fit to existing storage characteristics.

3.2.1 Heat transfer

As the model does not have any discretization, the PCM cell temperature is different to the temperature next to the tube wall, necessary for the calculation of the heat power transferred to the PCM, see Eq. (3.4). To correct the heat transfer, the calculation of the heat transfer coefficient U is modified. In this single-node model, heat transfer is modelled with two heat resistances in series R_1 and R_2, as shown in figure 3.14.
The total heat transfer coefficient U is calculated with Eq. 3.43.

$$R = R_1 + R_2 <=> \frac{1}{U} = \frac{1}{U_1} + \frac{1}{U_2} \tag{3.43}$$

In the following two paragraphs the heat transfer coefficients U_1 and U_2 will be explained.

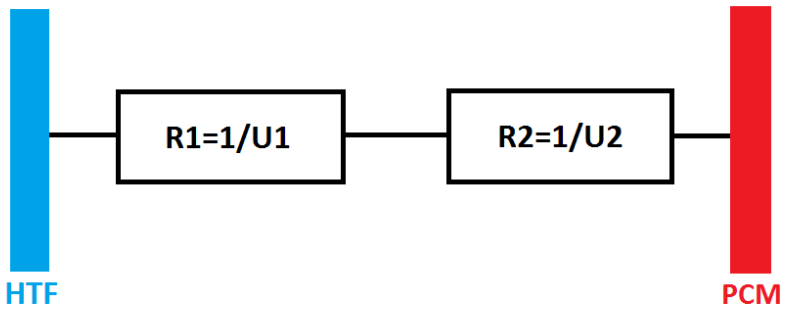

Figure 3.14: Schema of the heat transfer

Heat transfer coefficient U1

This first heat transfer coefficient is of the same nature as the one for the discretized model, introduced in section 3.1.1.It describes the dependency of the heat transfer coefficient on the flow rate in the HTF tubes.
A very simplified approach is used for the calculation of U_1. It is described by a linear dependency on the HTF mass flow rate $\dot{m}$, given in Eq. 3.44.

$$U_1 = a_5(\dot{m} - \dot{m}^*) + U_1^* \tag{3.44}$$

where U_1^* is the reference heat transfer coefficient value at a mass flow $\dot{m}^*$. It is calculated using the data given by the discretized model. a_5 is a system parameter representing the dependency of the U_1 on the HTF mass flow rate. For the further calculations following reference values have been used:

- U_1^*=700 $[W/m^2K]$
- $\dot{m}^*$=3 $[kg/s]$

Heat transfer coefficient U2

Before describing the heat transfer coefficient U_2, an analyse of the heat transfer in a real storage is presented.
In the loading process of a storage the PCM melts from the HTF tube with a melting front outwards (see figure 4.2).

As the temperature near the tube wall increases quickly over the melting temperature, the thermal power transferred to the PCM decreases. The more PCM is in molten state (high SOC), the more decreases the power delivered to the PCM. Figure 3.15 shows this behaviour. The curve has been generated with simulation data of the discretized model.

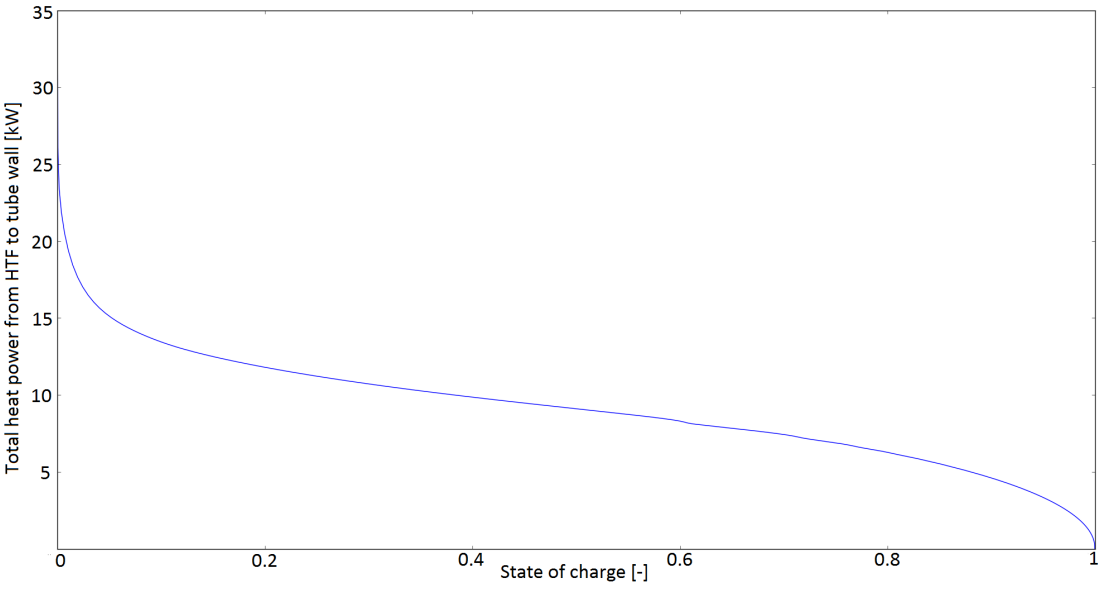

Figure 3.15: Thermal heat power HTF-PCM as a function of the global storage SOC

The lumped heat transfer conductance AU, can be easily be deduced by the thermal power using Eq. 3.45:

$$AU = \frac{\dot{Q}_H}{T_{H,avg} - T_m} \quad with \quad T_{H,avg} = \frac{T_H^{su} + T_H^{ex}}{2} \tag{3.45}$$

and T_m the melting temperature of the PCM.

Plotting the heat transfer conductance AU for different HTF mass flow rates of the melting process, we get the results shown in figure 3.16.

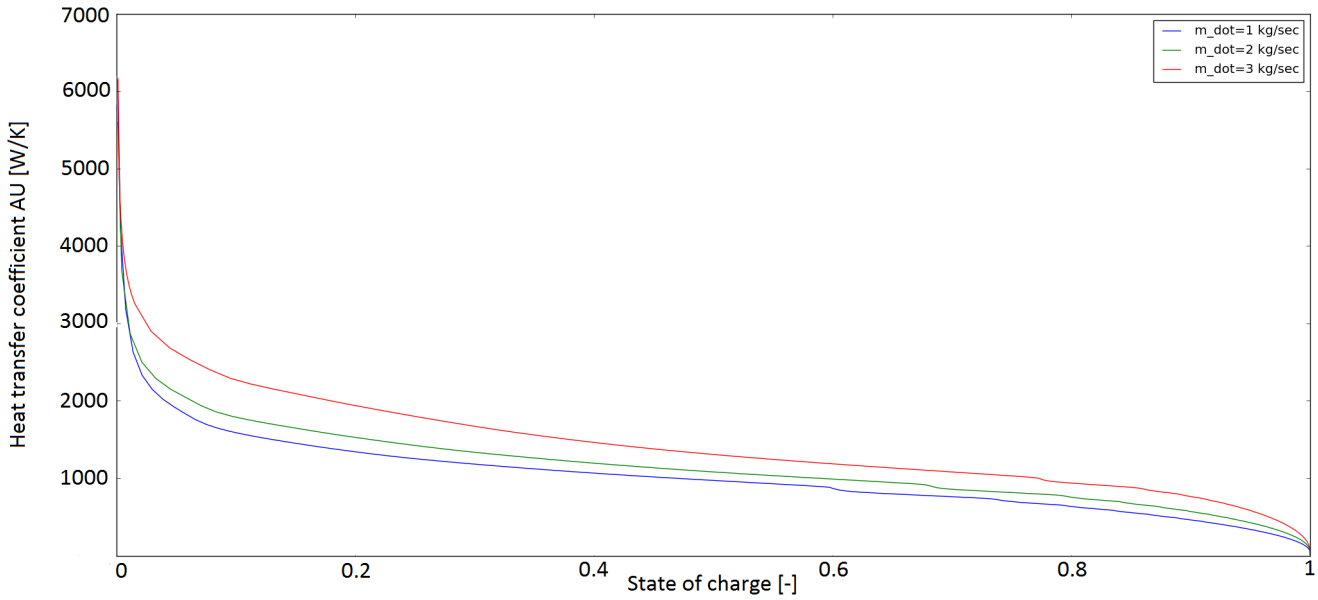

Figure 3.16: Heat transfer coefficient AU as a function of SOC for different mass flows (melting process). Higher heat transfer is obtained with higher mass flow rate

The same procedure has been done for the solidification process. The result can be seen in figure 3.17.

The heat transfer coefficient U can be deduced on AU by devising the latter by the total heat transfer area, which is in this case the sum of the inner tube HTF surfaces. As this area is geometrical value and not depending on the SOC, the shape of U is the same as for AU.

As it can seen in figure 3.17, the shape of the curve for the solidification process is the same as for melting, but inverted. So the value of U at a given SOC in the melting process is equal to the U at $1-SOC$ in the solidification

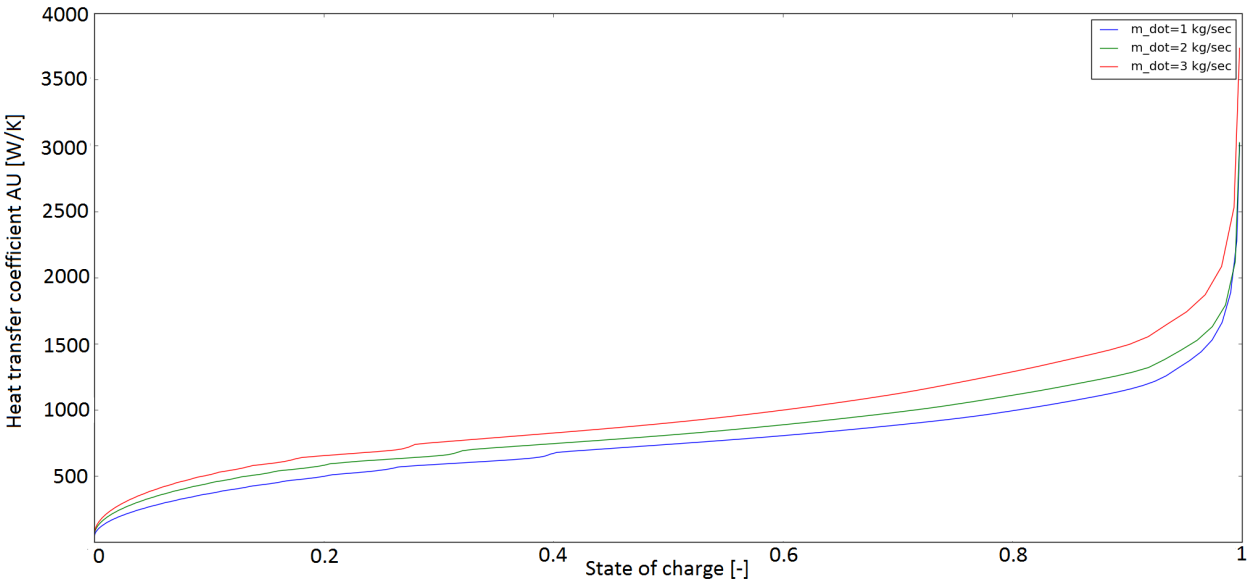

Figure 3.17: Global coefficient of heat transfer AU as a function of SOC for different mass flows (solidification process). Higher heat transfer is obtained with higher mass flow rate

process. Therefore a new variable x is introduced which value is defined by Eq. 3.46.

$$x = \begin{cases} SOC & \text{if melting process} \\ 1 - SOC & \text{if solidification process} \end{cases} \tag{3.46}$$

Now, knowing the shape of U, as well as U_1 for a given mass flow rate, the heat transfer coefficient U_2 can be described as the part of U representing its dependency on the SOC.

Figure 3.18 represents the total heat transfer coefficient U as well as its composition by U_1 and U_1 as a function of SOC for a HTF mass flow rate of 3 kg/s.

Analysing the shape of U_2 we can observe that for low SOC values, it de-

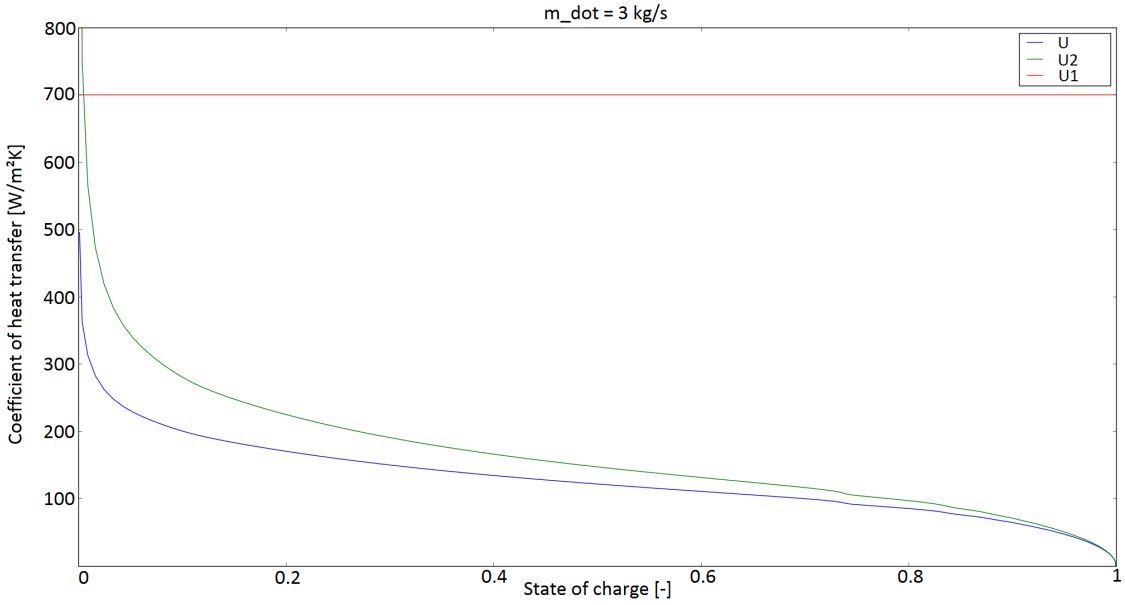

Figure 3.18: Heat transfer coefficients for a HTF mass flow rate of 3 kg/sec. The reation between the heat transfer coefficient can be found in Eq. (3.43)

creases approximately as $1/x$ followed by a nearly linear behaviour and end with a behaviour of $\sqrt{1-x}$ for SOC approaching 1. For this reasons the following equation for U_2 has been developed:

$$U_2 = \frac{1}{a_1 + a_2 \cdot x} + a_3\sqrt{1-x} + a4 \tag{3.47}$$

where x is the variable introduced in Eq. (3.46).

Eq. (3.47) possesses 4 parameters (a_i) describing the heat transfer. Including the parameter for the calculation of U_1 the heat transfer model is described by 5 parameters.

In the following, two other equations for AU_2 are listed using more simple expressions with only 3 parameters. They are named **version 2** (Eq. 3.48)

and **version 3** (Eq. 3.49). **Version 1** correspond to the initial expression in Eq. (3.47).

$$U_2 = a_1(1-x)^{a_2} + a_3 \tag{3.48}$$

$$U_2 = \frac{a_1}{1+x^{a_2}} + a_3 \tag{3.49}$$

A comparison in results between the versions can be found in section 4.2.3.

For the later model validation is does not make any difference if the parameter optimization is done for the calculation of U (resp. U_1 and U_2) or AU (resp. AU_1 and AU_2), because the heat transfer surface is a constant that would not modify the equation for the heat transfer coefficient calculation (see Eq. 3.43). In the case of the AU adaptation, the optimized parameters would include the heat transfer surface, so that there is no further need to define a specific geometrical parameter for this heat transfer area. Using this method, the model needs less geometrical parameters.
For our model validation, both approaches will be analysed. As we know exactly the geometrical dimensions of the storage, the pure coefficient of heat transfer U can be parametrized. The heat transfer coefficient AU is used, when the heat exchanger geometry is unknown.

3.2.2 Model implementation in Modelica

As for the discretized model, three main components compose the single node model:

- HTF component
- Tube wall component
- PCM component

Heat transfer fluid

The HTF component calculates the fluid state of the HTF and regulates the heat transfer to the tube wall by using modified heat transfer components of

the ThermoCycle library. They contain the heat transfer coefficient calculations introduced above.
An icon of the HTF component is given in figure 3.19 Enthalpy is used as

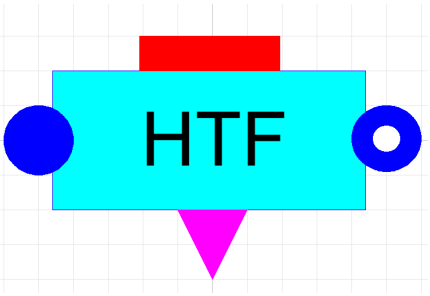

Figure 3.19: HTF component of the single-node grey-box model

state variable, so the energy balance equation is of the form as given by Eq. (3.50).

$$V_H \cdot \rho_H \cdot \frac{d}{dt} h_H + \dot{m}_H (h_{su} - h_{ex}) = \dot{Q}_H \tag{3.50}$$

where h_{out} and h_{in} are linked to h by a upwind scheme discretization.
The thermal power $\dot{Q}$ is calculated using the heat transfer coefficient AU:

$$\dot{Q}_H = AU(T_H - T_W) \tag{3.51}$$

As introduced in Eq. (3.46) the variable x necessary for the computation of the heat transfer coefficient is depending on the fact if the storage is in the loading or unloading condition.
To let the model know in which state the storage is, a condition has to be set up. This condition uses the power delivered by the HTF. A boolean variable has been created, named *loading*. It is defined by Eq. 3.52.

$$loading = \begin{cases} \texttt{true} & \text{if} \quad \dot{Q}_H \leq 0 \\ \texttt{false} & \text{if} \quad \dot{Q}_H > 0 \end{cases} \tag{3.52}$$

The loading condition enters the HTF component by an boolean input, as it can be seen in figure 3.21. There it is transferred to the heat transfer components, where the calculation of the x variable is situated.

Tube wall

The tube wall component models the thermal heat capacity of the heat exchanger. No thermal conductance inside the tube is assumed. Therefore the temperature of the tube wall corresponds to the PCM temperature ($T_P = T_W$).
The energy balance of the tube wall is given in Eq. (3.53), where temperature is chosen as state variable.

$$m_W \cdot c_{P,W} \cdot \frac{d}{dt} T_W = \dot{Q}_P - \dot{Q}_H \tag{3.53}$$

The component item is the same as for the discretized model, see figure 3.3.

Phase change material

As the discretized model, the single-node model uses the apparent heat capacity method to model the melting process. The sigmoid function ($Mod2$) is implemented only in this model.
The energy balance of the specified mass of PCM, with temperature as state variable is given in Eq. (3.54).

$$m_P \cdot c_{p,P} \cdot \frac{d}{dt} T_P = -\dot{Q}_P \tag{3.54}$$

Unlike the discretized PCM component, the single node model component possesses only one thermal port, because there is no further need for the axial and radial heat conduction between multiple PCM cells.
Figure 3.20 shows the item of the PCM component.

Figure 3.20: PCM component in the single node model

Storage

The connection between the single components is realized in the same way as for the discretized model, see figure 3.21.

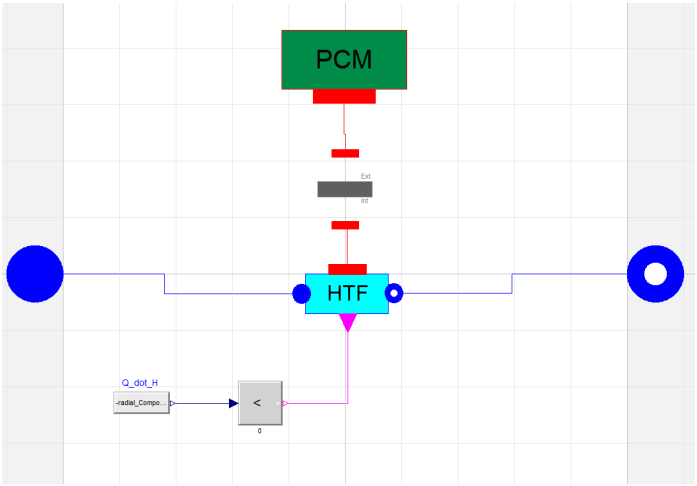

Figure 3.21: Assembly of the components in the single node model

As in the discretized model, it possesses two fluid flow connectors for the HTF inlet and outlet.
The model uses no longer detailed geometrical parameters for the energy balance calculation, but only the fluid volumes of the HTF and the total masses of the heat exchanger and the phase change material.
The icon of the model is presented in figure 3.22.

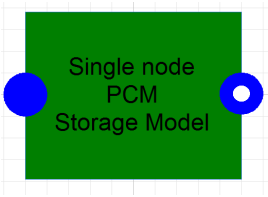

Figure 3.22: *Single_node_storage_model* item

In the parameter settings, the user can choose between the version of heat transfer calculation (see Eqs. 3.47, 3.48, 3.49).

3.2.3 Storage parameters

Phase change medium

As already mentioned in section 3.2.2, the phase change medium model used in the single-node model is *Model 2* from section 3.1.3. The parameters can be found in table 3.1.
Only difference to the discretized model, consists in the fact that there is no longer necessity of the parameter λ_P, which is lumped into the overall heat transfer coefficient.
In fact, λ_P characterizes the heat transfer in the PCM. Multiplied by the heat conduction width it corresponds to the heat transfer coefficient between the PCM cells.
In the single-node model, the heat transfer coefficient is computed by external equations depending on the SOC, including the information of the thermal conductivity of the PCM.
By consequence, there are only 4 PCM parameters in the case of the single node model: $c_{p,P}, \mathrm{L}, \Delta T, T_m$.

Heat transfer

Depending on the heat transfer version used, the user has to specify the parameters a_1, a_2, a_3, a_4, a_5 for the *version 1* and a_1, a_2, a_3, a_5 for *version 2* and *version 3*.

Geometry

Table 3.3 summarizes the geometrical parameters to be provided to the storage model.

Parameter	Desecration	Unit	Ref. equation
V_H	Volume of heat transfer fluid in the heat exchanger tubes	m^3	3.50
m_W	Total mass of the heat exchanger	kg	3.53
m_P	Total mass of phase change material in the storage	kg	3.54

Table 3.3: Geometrical storage parameters for the *Single_node_storage*

Other parameters

Several other parameters have to be provided to the model:

- `HTF`: The user can specify the heat transfer fluid
- `Mdotnom`: Nominal HTF flow rate
- `heat_transfer`: The user can choice between different heat transfer calculation expression (version 1-3 and constant)
- $c_{P,W}$: Specific heat capacity of the heat exchanger material
- `U_nom`: Heat transfer value if the constant model is chosen

Further simplifications could have been done. For example the thermal capacity of the heat exchanger could be included into the phase change material. In this case m_W and $c_{P,W}$ can be eliminated from the parameter list. Furthermore, the HTF fluid volume is not mandatory. In fact, V_H can be eliminated by omitting the derivative part in Eq.(3.50).

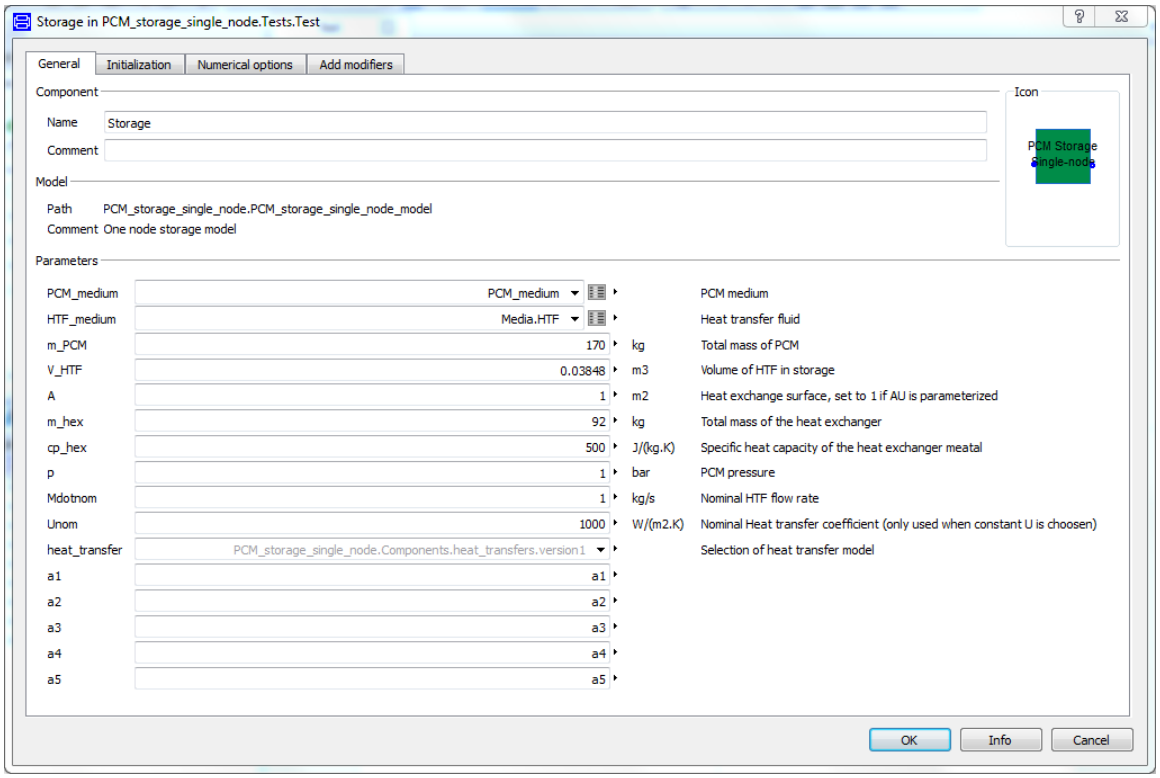

Figure 3.23: Parameter window of the single-node grey-box model

Chapter 4

Model validation: Results and discussion

4.1 Discretized PCM storage model

4.1.1 Introduction

In the following the results of the model validation for the discretized PCM storage mode are presented. The parameter determination based on a model simulation fitting to experimental data are analysed. A statistical analysis, treating correlation and error estimation, of the model parameters is included.

As introduced in section 3.1.3, two different models are considered *(Mod1, Mod2)* each with a different set of parameters. As described in section 3.1.3, they differ in the correlation used to model the apparent heat capacity $\tilde{c_P}$ and thermal conductivity λ_P.

Three experiments have been considered. The first consists in a charging, the second in a discharging and in the last the two were combined in a total changing-discharging cycle. In every experiment, the HTF flow rate is kept constant with low flows and laminar flow conditions in the pipes with Reynolds Numbers of 2100-2220. In the charging experiment the HTF storage inlet temperature is increased from approximately 105 to 155 °C and in the discharging experiment reduced from 155 to 105 °C.

Table 4.1 lists the starting parameter values for the curve fitting. They are the same for each of the three experiments. The signification of these parameters can be found in table 3.1.

Model 1						
Parameter	c2	c3	a0	b1	μ	σ
Unit	-	-	kJ/kg	kJ/kg	°C	-
Value	96.162	0.154	1.765	211.610	132	4.266

Model 2					
Parameter	λ_P	$c_{p,P}$	L	T_m	ΔT
Unit	W /m /K	kJ/kg	kJ/kg	°C	K
Value	1	1.765	211.610	132	10

Table 4.1: Starting values of the parameters in Model 1 and 2

As introduced in section 3.1.7, the storage possesses several geometrical parameters. In table 4.2, parameter values based on the lab-scaled storage, described in section 2.1.7 are resumed. These parameters are kept constant for the following model validation. The description of the parameters can be found in table 3.2.

Parameter	Value	Unit
N_{tube}	72	-
A_{ap}	0.1152	m^2
L_{hex}	2.5	m
d_{in}	0.0135	m
d_{out}	0.0165	m
$A_{fins,tot}$	59.8	m^2
d_{fins}	0.00025	m

Table 4.2: Geometrical storage parameters from the lab scaled storage

4.1.2 Parameter optimization

In order to validate the PCM storage model on experimental measurement data, the PCM storage parameters, presented in table 4.1, are optimized to fit the simulation outlet temperature results on the experimental curves.
The said optimization has been realised using a *Python*-based optimizer from the *SciPy* package. A documentation of the optimizer can be found in [4]. To run simulations out of a *Python*-script, the *Simulator* class of the *BuildingsPy* package has been employed. The corresponding documentation is provided in [5].
A *least-square* method has been used to fit the simulation data curve on the measurements one. It takes an error vector as input, which corresponds to the differences for simulation and measurement data in outlet temperatures for each time step. The optimizer tries du minimise this error, by varying the PCM storage parameters.
To archive model validation for different HTF mass flows, the optimization has been done by providing the sum of two error vectors resulting of simulations with different HTF mass flows to the optimizer. Simulations with 1 kg/s and 0.35 kg /s have been considered.
Beside the fact that the *SciPy* optimizer returns an optimized parameter set, it also provides the covariance matrix of the parameters, which will be used for further statistical analyses.

4.1.3 Charging experiment

Model validation

In the single charging experiment, the HTF inlet temperature is kept constant around 155 °C over a time of 9000 seconds, with an initial uniform storage PCM temperature of 105 °C. Figure 4.1 represents the inlet temperature profiles for different mass flows. After an initial increasing, the temperature is kept constant. The storage outlet temperature is then fitted to the measurement using a parameter optimization.

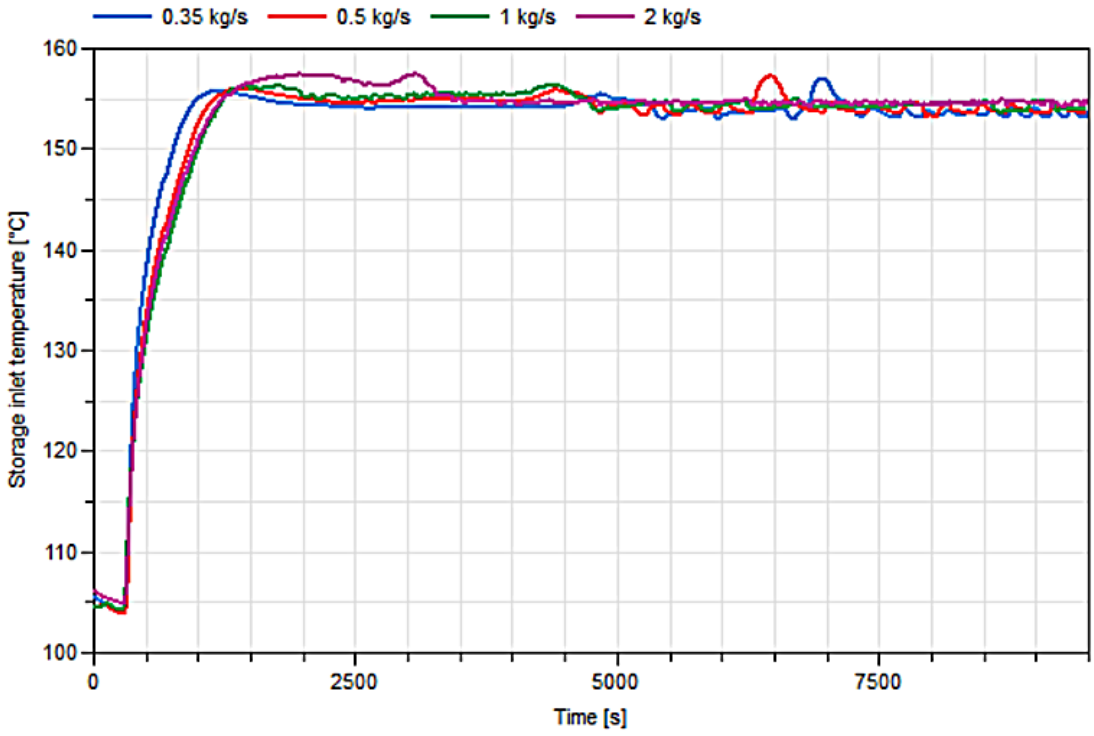

Figure 4.1: Storage inlet temperature profiles for different mass flows in the charging experiment. Nearly the same temperature profiles can be observed

To get a better view of the melting process in the storage, a 2D visualization is given in figure 4.2. The storage has been discretized by 50 cells in axial direction and 10 cells in radial direction, giving a total discretization of 500 cells. The state of charge is represented as a function of time for a mass flow of 1 kg/s.
The x-axes corresponds to the axial direction (HTF flow direction) and the y-axes to the radial direction of the tube.

The optimized parameters for the charging experiments are shown in table 4.3. In the first row the parameters are in the absolute value, in the second they are normalized to the start values of table 4.1.

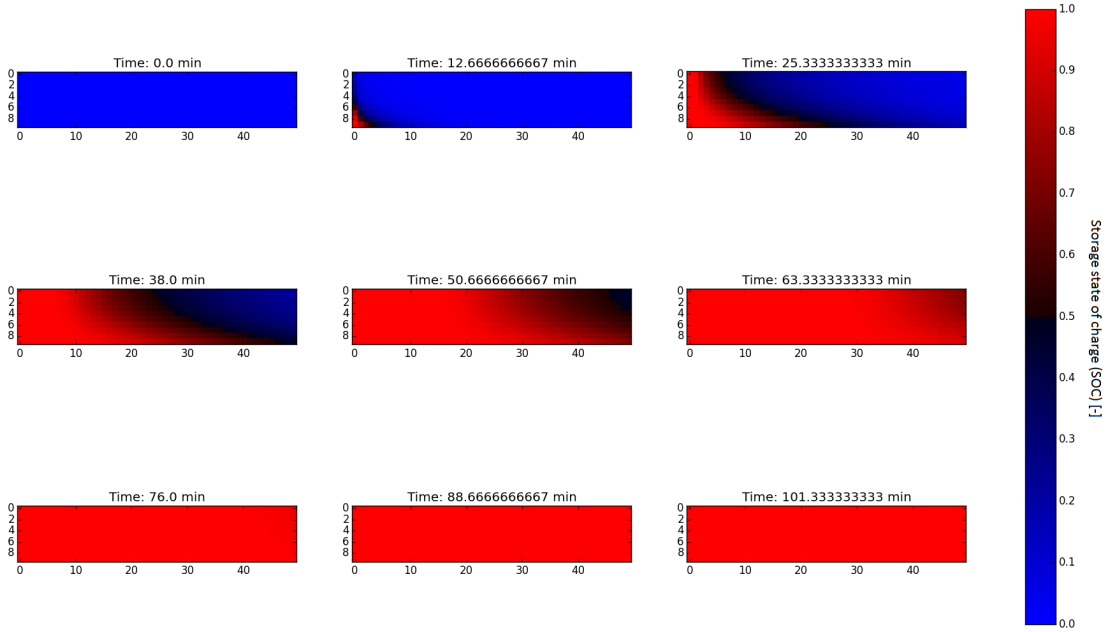

Figure 4.2: 2D visualization of the melting process (SOC, $\dot{m} = 1kg/s$)

The temperature profiles for the charging experiments using the model 1 and 2 are shown in figure 4.3 and figure 4.4 respectively. The predicted external HTF temperatures fit the measurements very well.

Model 1						
Parameter	c2	c3	a0	b1	μ	σ
Unit	-	-	kJ/kg	kJ/kg	°C	-
Absolute	170.356	1.580	2.431	104.919	127.961	4.177
Normalized	1.771	10.259	1.377	0.495	0.990	0.979

Model 2					
Parameter	λ_P	$c_{p,P}$	L	T_m	ΔT
Unit	W /m /K	kJ/kg	kJ/kg	°C	K
Absolute	1.648	2.307	107.630	125.968	8.223
Normalized	1.648	1.307	0.508	0.985	0.822

Table 4.3: Estimated parameters in Model 1 and 2 for the individual fitting of data from a single charging.

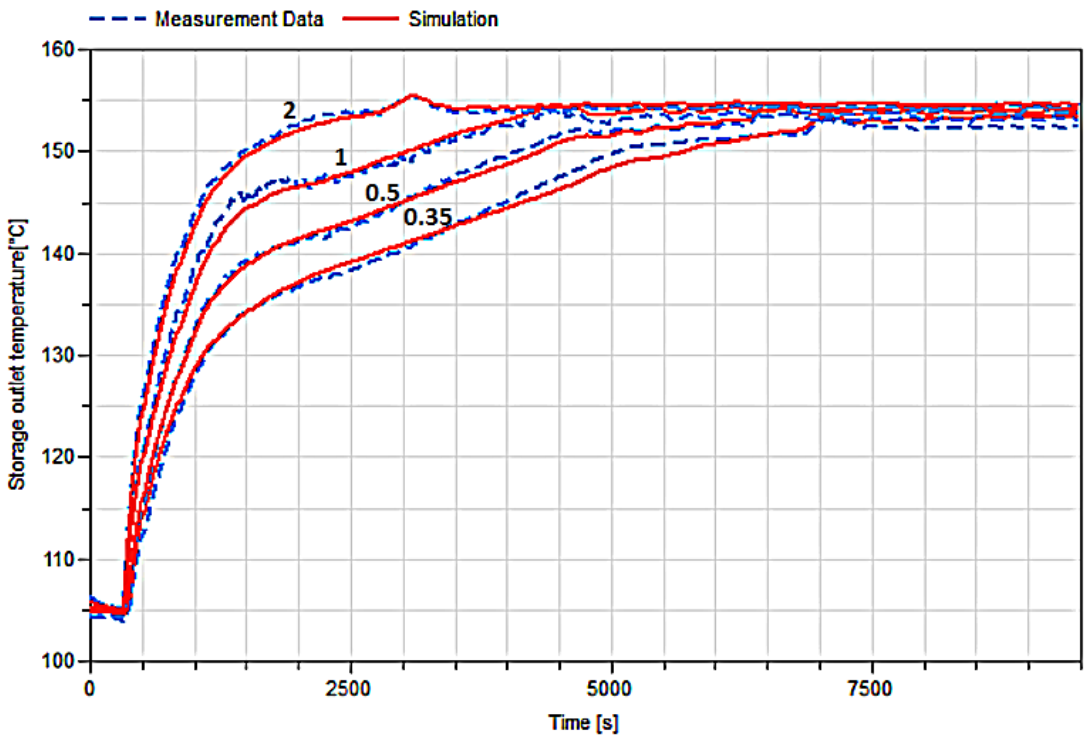

Figure 4.3: Experimental data and model predictions for *Mod1* for mass flow rates 0.35 to 2 kg /s

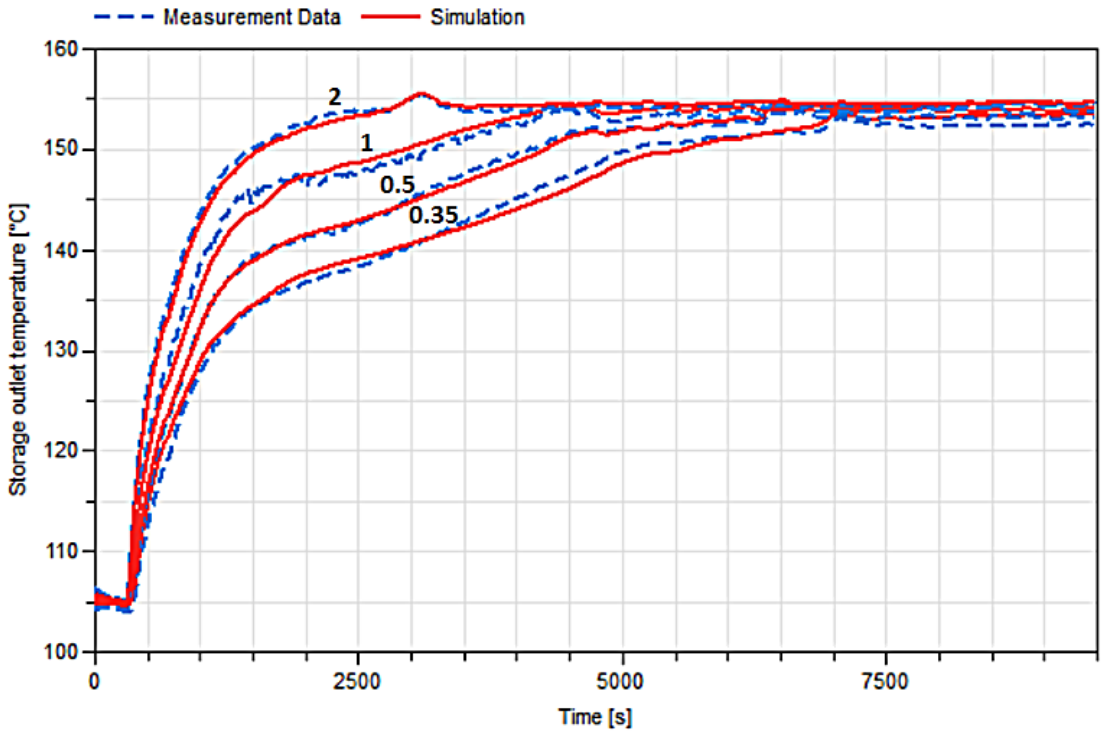

Figure 4.4: Experimental data and model predictions for *Mod2* for mass flow rates 0.35 to 2 kg /s

Error estimation

The optimization procedure returns also the covariance matrix (also known as dispersion matrix) for the parameters. Its elements (i,j) give the covariance between the i^{th} and j^{th} elements of the parameter vector.

For the model 1, the covariance matrix is the following:

$$\mathbf{cov_1} = \begin{array}{c} \begin{array}{cccccc} c2 & c3 & a0 & b1 & \mu & \sigma \end{array} \\ \begin{pmatrix} 18.3976 & -0.0711 & 0.0030 & -0.0829 & -0.1423 & -0.1580 \\ -0.0711 & 0.0012 & -0.0003 & 0.0091 & 0.0031 & -0.0008 \\ 0.0030 & -0.0003 & 0.0024 & -0.0916 & 0.0009 & -0.0002 \\ -0.0829 & 0.0091 & -0.0916 & 4.1958 & -0.0380 & 0.0164 \\ -0.1423 & 0.0031 & 0.0009 & -0.0380 & 0.0585 & 0.0003 \\ -0.1580 & -0.0008 & -0.0002 & 0.0164 & 0.0003 & 0.0111 \end{pmatrix} \end{array} \begin{array}{c} c2 \\ c3 \\ a0 \\ b1 \\ \mu \\ \sigma \end{array}$$

And for the model 2:

$$\mathbf{cov_2} = \begin{array}{c} \begin{array}{ccccc} \lambda_P & c_{p,P} & L & \Delta T & T_m \end{array} \\ \begin{pmatrix} 0.0013 & -0.0003 & 0.0179 & -0.0029 & 0.0049 \\ -0.0003 & 0.0025 & -0.0903 & -0.0003 & 0.0014 \\ 0.0179 & -0.0903 & 3.8634 & -0.0511 & -0.0478 \\ -0.0029 & -0.0003 & -0.0511 & 0.0477 & -0.0021 \\ 0.0049 & 0.0014 & -0.0478 & -0.0021 & 0.0674 \end{pmatrix} \end{array} \begin{array}{c} \lambda_P \\ c_{p,P} \\ L \\ \Delta T \\ T_m \end{array}$$

Once the covariance matrix is known, we can directly extract the relative error of the parameters, because of the following explanation.

We know that the covariance matrix is of the following form:

$$\mathbf{cov} = \begin{pmatrix} \delta_1^2 & \delta_{12} & ... & \delta_{1n} \\ \delta_{21} & \delta_2^2 & ... & \delta_{2n} \\ ... & ... & ... & .... \\ \delta_{n1} & \delta_{n2} & ... & \delta_{nn}^2 \end{pmatrix}$$

So the elements (i,i) on the diagonal line correspond to the variance of the parameter i. By consequent the standard deviation δ, or relative error is given by the following expression:

$$perr_i = \delta_i = \sqrt{\mathbf{cov}(i,i)} \tag{4.1}$$

The relative errors found for the parameters of the models 1 and 2 are listed

Model 1					
c2	c3	a0	b1	μ	σ
4.289	0.035	0.049	2.048	0.242	0.105

Model 2				
λ_P	$c_{p,P}$	L	T_m	ΔT
0.036	0.050	1.965	0.259	0.218

Table 4.4: Relative errors of estimated parameters in Model 1 and 2 for the individual fitting of data from a single melting

in table 4.4.

High relative error values have been obtained for the latent heat of fusion b1 ($Mod1$), L ($Mod2$). As well as for c2 describing the thermal conductivity λ_P. Plotting the equation of λ_P, Eq. (3.26), with the optimized parameters of table 4.3, the blue curve of figure 4.5 is obtained. Parameter c2 describes at which temperature the decrease in conductivity occurs. Two further curves were plotted for different parameter values of c2.

The high relative error indicates that a change in c2 odes not marginally influence the simulation results, which is the outlet temperature in this case. Therefore, in $Mod2$, only a constant thermal conductivity over temperature has been chosen, for which the relative error is negligible.

Parameter correlation

Not only the relative error can be deduced by the covariance matrix, but also the correlation matrix. This matrix of the same size as the covariance matrix characterizes the correlation between the parameters.
The correlation matrix can be seen as the covariance matrix of the standardized variables $X_i/\delta(X_i)$. So the elements of the correlation matrix are calculated with the following formulae:

$$\mathbf{corr}(i,j) = \frac{\mathbf{cov}(i,j)}{\sqrt{\mathbf{cov}(i,i) * \mathbf{cov}(j,j)}} \tag{4.2}$$

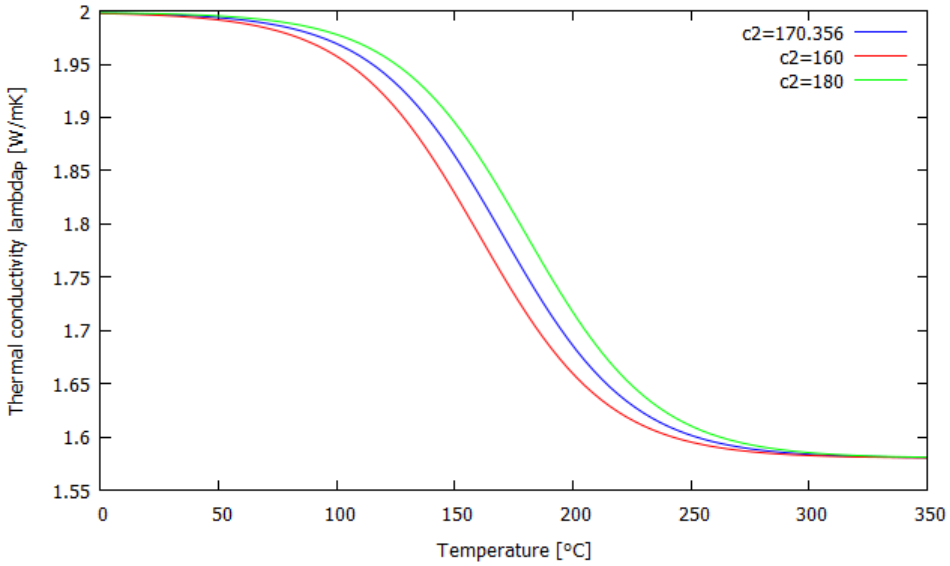

Figure 4.5: Thermal conductivity λ_P as a function of temperature for different parameters c2

The elements of the correlation matrix are in the range of [-1;1] where the extremities -1 and 1 design a total correlation while 0 indicates no correlation. It is clear that the elements on the diagonal line are all equal to 1 because a parameter correlates always totally with itself.

The correlation matrices of the model 1 and 2 are given hereby:

$$\mathbf{corr_1} = \begin{array}{c} \begin{matrix} c2 & c3 & a0 & b1 & \mu & \sigma \end{matrix} \\ \begin{pmatrix} 1 & -0.4621 & 0.0146 & -0.0094 & -0.1371 & -0.3490 \\ -0.4621 & 1 & -0.1845 & 0.1245 & 0.3679 & -0.2220 \\ 0.0146 & -0.1845 & 1 & -0.9099 & 0.0749 & -0.0380 \\ -0.0094 & 0.1245 & -0.9099 & 1 & -0.0767 & 0.0761 \\ -0.1371 & 0.3679 & 0.0749 & -0.0767 & 1 & 0.0141 \\ -0.3490 & -0.2220 & -0.0380 & 0.0761 & 0.0141 & 1 \end{pmatrix} \end{array} \begin{matrix} c2 \\ c3 \\ a0 \\ b1 \\ \mu \\ \sigma \end{matrix}$$

$$\mathbf{corr_2} = \begin{array}{c} \begin{matrix} \lambda_P & c_{p,P} & L & \Delta T & T_m \end{matrix} \\ \begin{pmatrix} 1 & -0.2103 & 0.2518 & -0.3733 & 0.5309 \\ -0.2103 & 1 & -0.9163 & -0.0300 & 0.1079 \\ 0.2518 & -0.9163 & 1 & -0.1191 & -0.0936 \\ -0.3733 & 0.0300 & -0.1191 & 1 & -0.0378 \\ -0.5309 & 0.1079 & 0.0936 & -0.0378 & 1 \end{pmatrix} \end{array} \begin{matrix} \lambda_P \\ c_{p,P} \\ L \\ \Delta T \\ T_m \end{matrix}$$

After analysing this matrices, one correlation factor sticks out. We obtained values of -0.9099 and -0.9163 in the models 1 and 2 respectively for the correlation of latent heat (b1 in model, L in model 2) and specific caloric heat capacity (a0 in model 1 and cp0 in model 2). The fact that the correlation number of ij is negative indicates, that if parameter i increases, it has the opposite effect than an increase of j
So we can conclude that the latent heat and the specific caloric heat capacity are correlated. It is understandable because both increase the storage capacity and have a similar effect on the overall behaviour.

4.1.4 Discharging experiment

Model validation

In the discharging experiment, the inlet temperature is reduced from 155 to around 105 °C. The inlet temperature profiles are represented in figure 4.6. The storage outlet temperature is then fitted to the measurement using a parameter optimization. Like the charging experiment, the process is simulated over 9000 seconds.

As for the charging experiment, a 2D visualization of the process is given in figure 4.7 .

The second step consists in the parameter estimation for the discharging experiment. The approach is the same as in the melting experiment.

The optimized parameters are shown in table 4.5.

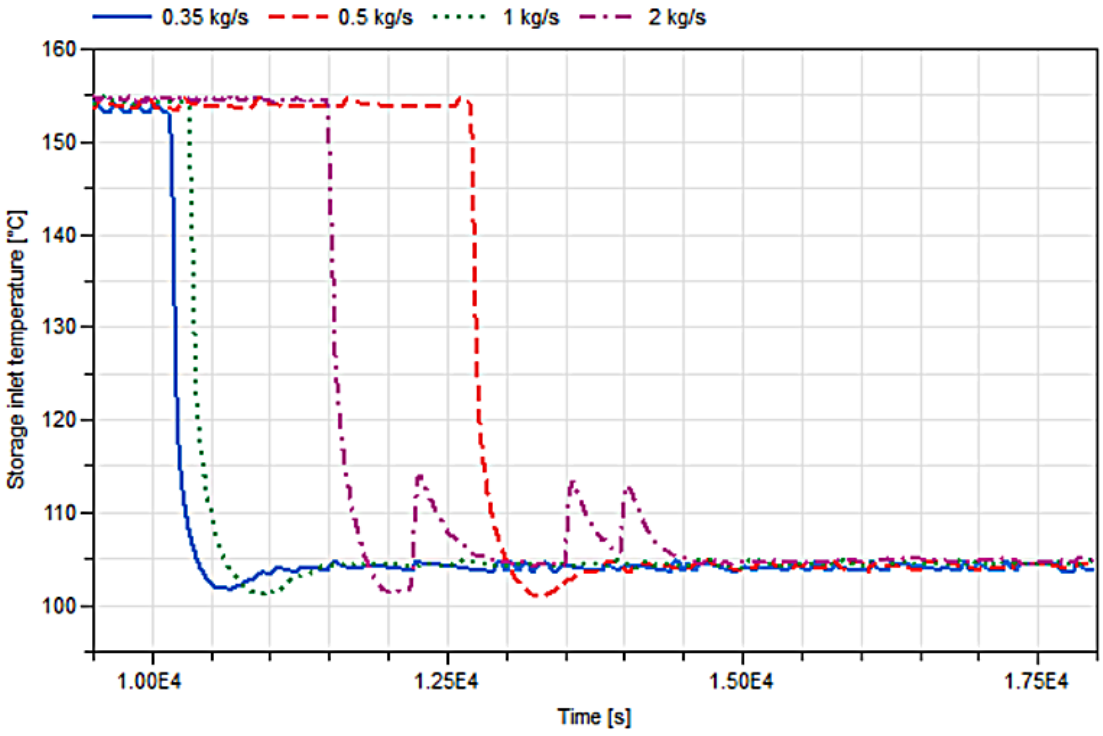

Figure 4.6: Storage inlet temperature profiles for different mass flows in the discharging experiment. The fluctuations for 2 kg /s result from the laboratory devices and have no experimental intention.

The temperature profiles for the discharging experiments using the model 1 and 2 are shown in figures 4.8 and 4.9 respectively.

As in the charging experiment, the simulated temperature profile fits the experiment data very well.

Error estimation

Once more the covariance matrix has be calculated by the optimization program:

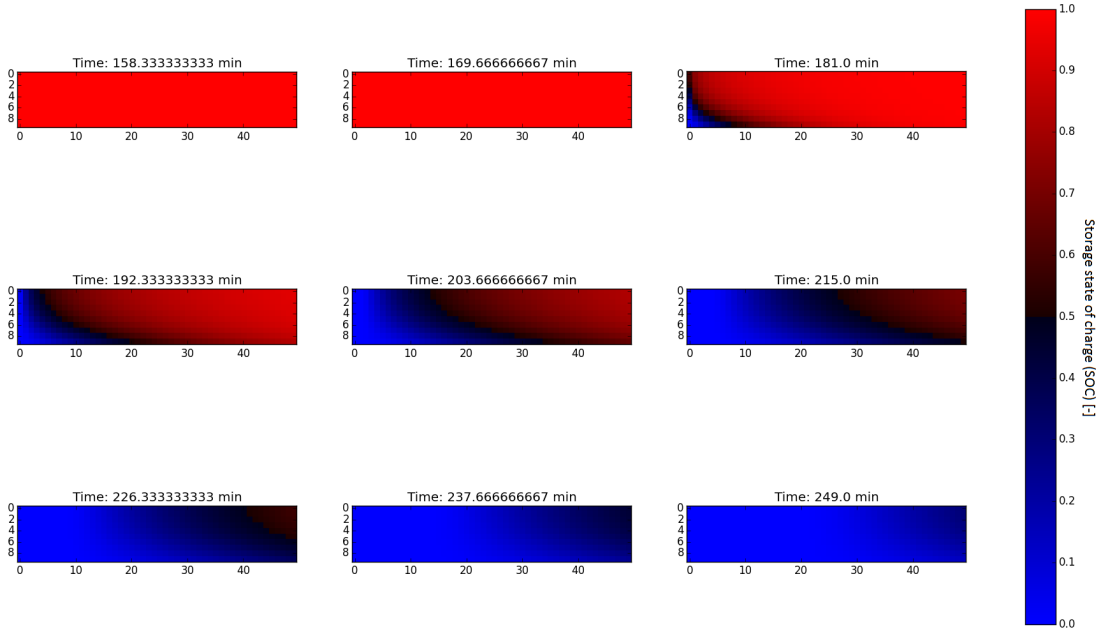

Figure 4.7: 2D visualization of the discharging process (SOC, $\dot{m} = 1kg/s$)

$$\mathbf{cov_1} = \begin{array}{c} \begin{matrix} c2 & c3 & a0 & b1 & \mu & \sigma \end{matrix} \\ \begin{pmatrix} 104.203 & -0.0367 & -0.0145 & -1.6784 & 0.3486 & -0.2960 \\ -0.0367 & 0.0002 & 9e-5 & 0.0054 & -0.0011 & -0.0004 \\ -0.0145 & 9e-5 & 0.0002 & -0.0122 & 7e-5 & -0.0004 \\ -1.6784 & 0.0054 & -0.0122 & 1.4365 & 0.0196 & 0.0236 \\ 0.3486 & -0.0011 & 7e-5 & 0.0196 & 0.0201 & 0.0005 \\ -0.2960 & -0.0004 & -0.0004 & 0.0236 & 0.0005 & 0.0103 \end{pmatrix} \end{array} \begin{matrix} c2 \\ c3 \\ a0 \\ b1 \\ \mu \\ \sigma \end{matrix}$$

And for the model 2:

Model 1						
Parameter	c2	c3	a0	b1	μ	σ
Unit	-	-	kJ/kg	kJ/kg	°C	-
Absolute	406.707	0.628	0.503	146.044	123.894	4.914
Normalized	4.229	4.078	0.284	0.690	0.979	1.151

Model 2					
Parameter	λ_P	$c_{p,P}$	L	T_m	ΔT
Unit	W /m /K	kJ/kg	kJ/kg	°C	K
Absolute	0.786	0.480	145.664	125.542	24.037
Normalized	0.786	0.272	0.688	0.984	2.403

Table 4.5: Estimated parameters in Model 1 and 2 for the individual fitting of data from a single discharging

$$\mathbf{cov_2} = \begin{array}{c} \begin{matrix} \lambda_P & c_{p,P} & L & \Delta T & T_m \end{matrix} \\ \begin{pmatrix} 0.0003 & -9e-5 & 0.0063 & -0.0041 & -0.0028 \\ -9e-5 & 0.0002 & -0.0111 & -0.0024 & 0.0007 \\ 0.0063 & -0.0111 & 1.4246 & -0.0338 & -0.0036 \\ -0.0041 & -0.0024 & -0.0338 & 0.4000 & 0.0238 \\ -0.0028 & 0.0007 & -0.0036 & 0.0238 & 0.0428 \end{pmatrix} \end{array} \begin{matrix} \lambda_P \\ c_{p,P} \\ L \\ \Delta T \\ T_m \end{matrix}$$

Using these covariance matrices, the relative errors of the parameters can be deduced. The results are presented in table 4.1.4
As for the melting experiment, high relative error values have been found for the latent heat of fusions (b1 and L) as well as for c2, describing the effective thermal conductivity of the PCM. Again, using a constant λ_P in $Mod2$, this disadvantage can be avoided.

Parameter correlation

The correlation matrices of the model 1 and 2 are given here by:

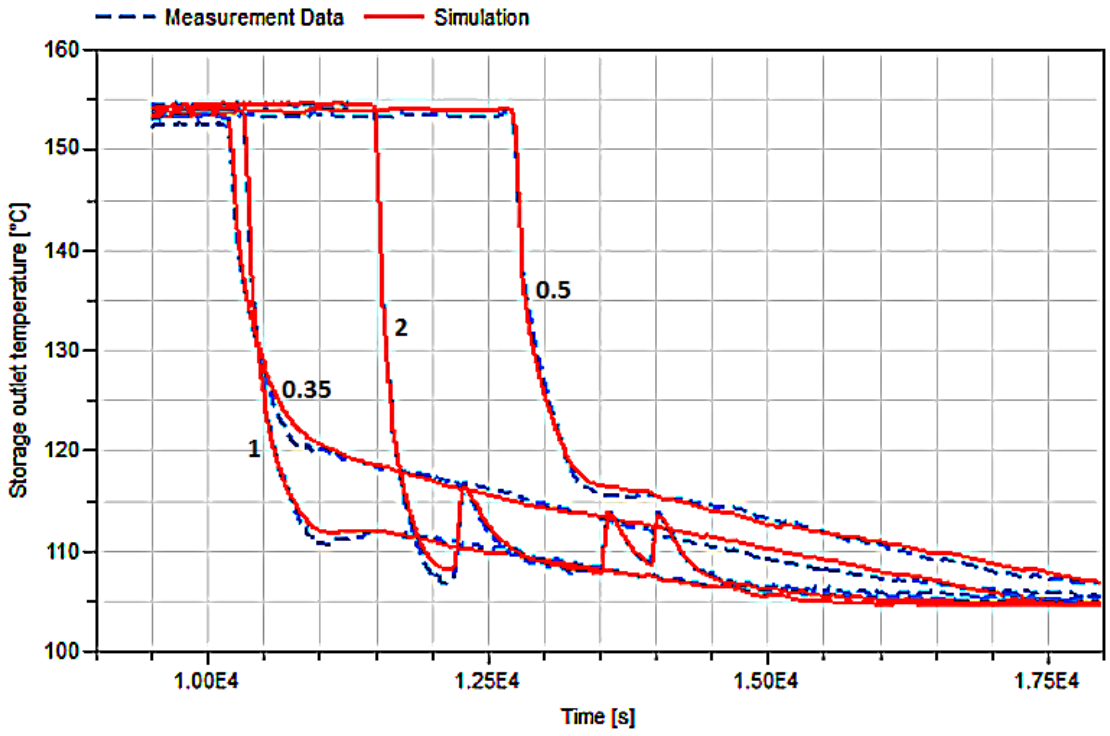

Figure 4.8: Experimental data and model predictions for *Mod1* for mass flow rates 0.35 to 2 kg /s.The fluctuation for $\dot{m} = 2$kg/s are very well resolved by the model.

Model 1					
c2	c3	a0	b1	μ	σ
10.207	0.016	0.015	1.198	0.142	0.102

Model 2				
λ_P	$c_{p,P}$	L	T_m	ΔT
0.018	0.013	1.193	0.207	0.632

Table 4.6: Relative errors of estimated parameters in Model 1 and 2 for the individual fitting of data from a single solidification

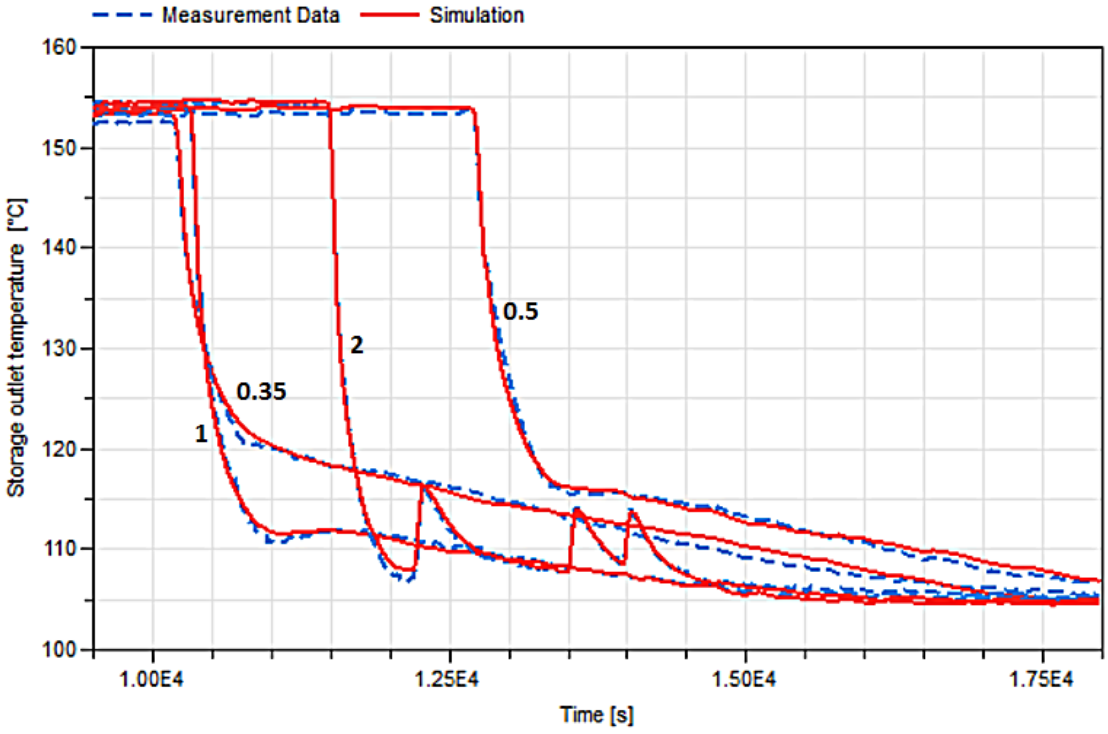

Figure 4.9: Experimental data and model predictions for *Mod2* for mass flow rates 0.35 to 2 kg /s

$$\mathbf{corr_1} = \begin{array}{c} \begin{matrix} c2 & c3 & a0 & b1 & \mu & \sigma \end{matrix} \\ \begin{pmatrix} 1 & -0.2150 & -0.0937 & -0.1371 & 0.2404 & -0.2845 \\ -0.2150 & 1 & -0.3717 & 0.2703 & -0.4513 & -0.2326 \\ -0.0937 & -0.3717 & 1 & -0.6706 & 0.0359 & -0.2670 \\ -0.1371 & 0.2703 & -0.6706 & 1 & 0.1151 & 0.1937 \\ 0.2404 & 0.4513 & 0.0359 & 0.1151 & 1 & 0.0340 \\ -0.2845 & -0.2326 & -0.2670 & 0.1937 & 0.0340 & 1 \end{pmatrix} \end{array} \begin{matrix} c2 \\ c3 \\ a0 \\ b1 \\ \mu \\ \sigma \end{matrix}$$

$$\mathbf{corr_2} = \begin{array}{c} \begin{array}{ccccc} \lambda_P & c_{p,P} & L & \Delta T & T_m \end{array} \\ \begin{pmatrix} 1 & -0.3663 & 0.2932 & -0.3620 & -0.7531 \\ -0.3663 & 1 & -0.6932 & -0.2827 & 0.2494 \\ 0.2932 & -0.6932 & 1 & -0.0448 & -0.0147 \\ -0.3620 & 0.2827 & -0.0448 & 1 & 0.1822 \\ -0.7531 & 0.2494 & -0.0147 & 0.1822 & 1 \end{pmatrix} \end{array} \begin{array}{c} \lambda_P \\ c_{p,P} \\ L \\ \Delta T \\ T_m \end{array}$$

Once again we can remark that the latent heat and the specific caloric heat capacity are largely correlated (by a correlation factor of 0.67 and 0.69). This factor is not as high as in the charging experiment (0.9 and 0.91) but still the most remarkable number compared to the other correlation factors in the matrix.

4.1.5 Total cycle: Charging-discharging experiment

Model validation

The last step consists in the parameter estimation for the combined melting and solidification experiment. For this experiment first the storage is heated in the first 9000 seconds up to 155 °C (charging experiment) and then cooled down again to 105 °C from second 9000 to 18000 (discharging experiment) Up to now, the two experiments were treated separately, but in reality the storage model has to be used for both experiments using the same parameters. So we have to find those parameters that optimize the both experiment. The results are shown in table 4.7.

The temperature profiles for the total experiment using the model 1 and 2 are shown in figure 4.10 and 4.11 respectively.

Model 1						
Parameter	c2	c3	a0	b1	μ	σ
Unit	-	-	kJ/kg	kJ/kg	°C	-
Absolute	226.066	0.665	1.351	132.399	123.039	5.339
Normalized	2.351	4.318	0.765	0.625	0.977	1.2515

Model 2					
Parameter	λ_P	$c_{p,P}$	L	T_m	ΔT
Unit	W /m /K	kJ/kg	kJ/kg	°C	K
Absolute	0.899	1.592	116.318	123.314	15.621
Normalized	0.899	0.901	0.549	0.978	1.562

Table 4.7: Estimated parameters in Model 1 and 2 for the individual fitting of data from the total experiment

Error estimation

Once more the covariance matrix has be calculated by the optimization program:

$$\mathbf{cov_1} = \begin{array}{c} \begin{matrix} c2 & c3 & a0 & b1 & \mu & \sigma \end{matrix} \\ \begin{pmatrix} 33.5033 & -0.0181 & -0.0197 & 0.3147 & 0.0463 & -0.2261 \\ -0.0181 & 0.0001 & -4e-5 & 0.0028 & -1e-6 & -0.0004 \\ -0.0197 & -4e-5 & 0.0009 & -0.0039 & -0.0007 & -0.0009 \\ 0.3147 & 0.0028 & -0.0039 & 2.4186 & 0.0331 & 0.0278 \\ 0.0463 & -1e-6 & -0.0007 & 0.0331 & 0.0299 & 0.0018 \\ -0.2261 & -0.0004 & -0.0009 & 0.0278 & 0.00018 & 0.0155 \end{pmatrix} \end{array} \begin{matrix} c2 \\ c3 \\ a0 \\ b1 \\ \mu \\ \sigma \end{matrix}$$

And for the model 2:

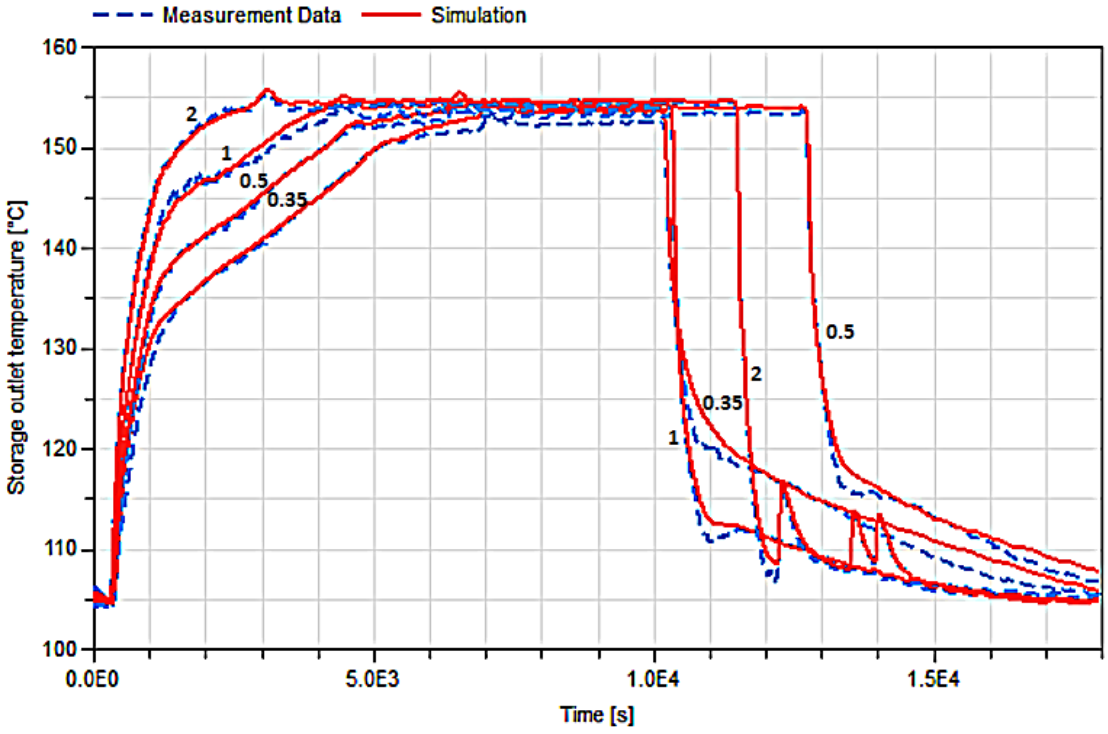

Figure 4.10: Experimental data and model predictions for *Mod1* for mass flow rates 0.35 to 2 kg /s

$$\mathbf{cov_2} = \begin{array}{c} \begin{matrix} \lambda_P & c_{p,P} & L & \Delta T & T_m \end{matrix} \\ \begin{pmatrix} 0.0002 & -9e-5 & 0.0034 & -0.0016 & -0.0001 \\ -9e-5 & 0.0009 & -0.0363 & -0.0254 & -0.0008 \\ 0.0034 & -0.0363 & 1.9930 & 0.1106 & 0.0443 \\ -0.0016 & -0.0254 & 0.1106 & 0.1187 & -0.0012 \\ -0.0001 & -0.0008 & 0.0443 & -0.0012 & 0.0284 \end{pmatrix} \end{array} \begin{matrix} \lambda_P \\ c_{p,P} \\ L \\ \Delta T \\ T_m \end{matrix}$$

Using these covariance matrices, the relative errors of the parameters are deduced and presented in table 4.1.5.

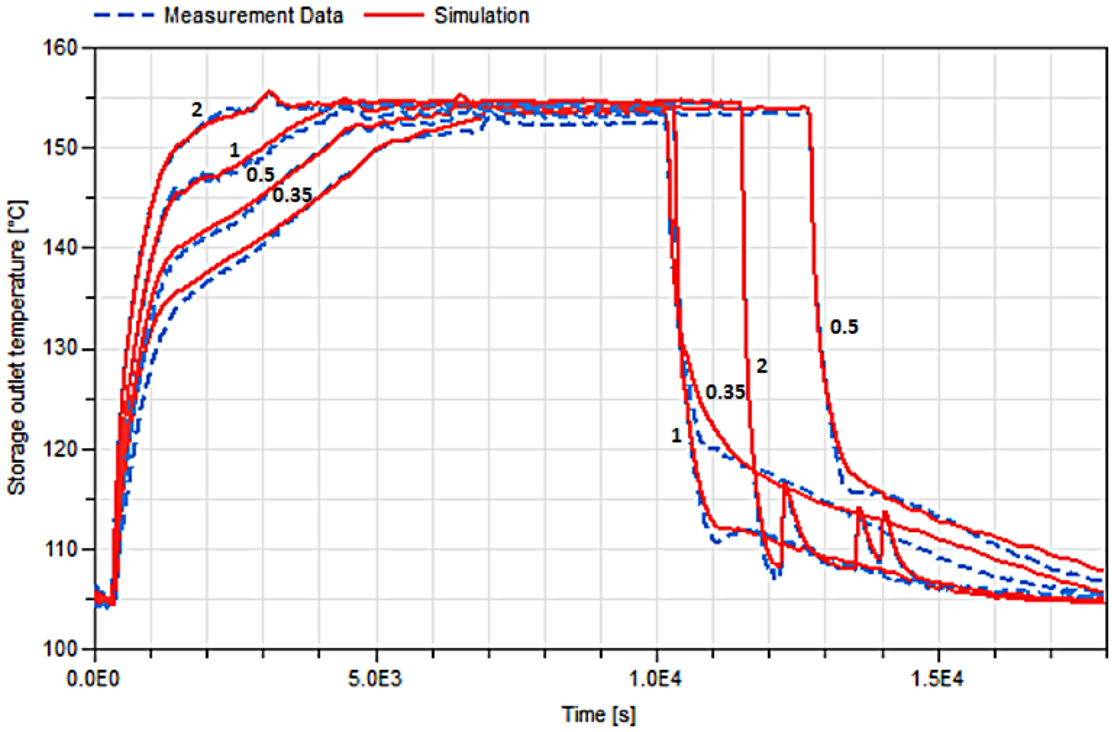

Figure 4.11: Experimental data and model predictions for *Mod2* for mass flow rates 0.35 to 2 kg /s

Model 1					
c2	c3	a0	b1	μ	σ
5.788	0.011	0.031	1.555	0.173	0.125

Model 2				
λ_P	$c_{p,P}$	L	T_m	ΔT
0.018	0.013	1.193	0.207	0.632

Table 4.8: Relative errors of estimated parameters in Model 1 and 2 for the individual fitting of data from the total cycle experiment

No surprising results have been obtained. They are similar to those of the individual experiments.

Parameter correlation

The correlation matrices of the model 1 and 2 are given here by:

$$\mathbf{corr_1} = \begin{array}{c} \begin{array}{cccccc} c2 & c3 & a0 & b1 & \mu & \sigma \end{array} \\ \begin{pmatrix} 1 & -0.2810 & -0.1104 & 0.0349 & 0.0462 & -0.3129 \\ 0.2810 & 1 & -0.1305 & 0.1653 & -0.0006 & -0.3404 \\ -0.1104 & -0.1305 & 1 & -0.8264 & -0.1428 & -0.2313 \\ 0.0349 & 0.1653 & -0.8264 & 1 & 0.1230 & 0.1435 \\ 0.0462 & -0.0006 & -0.1428 & 0.1230 & 1 & 0.0836 \\ 0.3129 & -0.3404 & -0.2313 & 0.1435 & 0.0836 & 1 \end{pmatrix} \end{array} \begin{array}{c} c2 \\ c3 \\ a0 \\ b1 \\ \mu \\ \sigma \end{array}$$

$$\mathbf{corr_2} = \begin{array}{c} \begin{array}{ccccc} \lambda_P & c_{p,P} & L & \Delta T & T_m \end{array} \\ \begin{pmatrix} 1 & -0.2195 & 0.1790 & -0.3563 & 0.0526 \\ 0.2195 & 1 & -0.8385 & -0.2404 & -0.1629 \\ 0.1790 & -0.8385 & 1 & 0.2274 & 0.1863 \\ -0.3563 & -0.2404 & 0.2274 & 1 & -0.0208 \\ 0.0526 & -0.1629 & 0.1863 & -0.0208 & 1 \end{pmatrix} \end{array} \begin{array}{c} \lambda_P \\ c_{p,P} \\ L \\ \Delta T \\ T_m \end{array}$$

Once again we can remark that the latent heat and the caloric specific heat capacity are largely correlated (by a correlation factor of 0.82 and 0.83 in this case).

4.1.6 Experiment result comparison

In the following section, we will analyse the optimized parameters from the three experiments and discuss the obtained differences.

Parameters

The optimized parameters for the charging, discharging and total cycle experiment are summarized in tables 4.3, 4.5 and 4.7, respectively.

Markable differences have been obtained on the melting temperature μ ($Mod1$) ,T_m ($Mod2$) and the latent heat of fusion $b1$ ($Mod1$), L ($Mod2$). Values of both are summarised in table 4.9:

Experiment	**Melting temperature**[°C]		**Latent heat of fusion**[kJ/kg]	
	Mod1	**Mod2**	**Mod1**	**Mod2**
	μ	T_m	$b1$	L
Charging	127.961	125.968	104.919	107.63
Discharging	123.894	125.542	146.044	145.664
Total cycle	123.039	123.314	132.399	116.318

Table 4.9: Parameter summary for the model validation experiments

Beginning with the melting temperature, a higher value of 4 K in the charging experiment compared to discharging can be ascertained in $Mod1$. This phenomena has been also observed in the DSC measurement of the PCM material. Figure 2.8 shows that there is a different apparent melting temperature according to the charging or discharging process. This phenomena is due to the sub-cooling of the phase change material.
Concerning $Mod2$, temperatures of the same magnitudes have been obtained for the three experiments.
A higher latent heat of fusion can be observed both in $Mod1$ and $Mod2$ for the discharging experiment. An average value for the total cycle experiment has been found.
Comparing values from $Mod1$ to $Mod2$, we can conclude that the obtained parameter values do not deviate significantly. Both models can be used for model validation and storage parameter prediction.

Simulation time

The major difference between $Mod1$ and $Mod2$ consists in the number of necessary parameters to describe the phase change material. The fact that $Mod2$ uses only 4 parameters, reduces the time necessary for the optimizer to find the optimal parameter set.
Due to the analytic expression of SOC as well as the simplified thermal conductivity λ_P in $Mod2$, a reduction in the total number of equations describing the system is obtained. Table 4.10 resumes the number of equations and the CPU simulation time for the melting experiment with $\dot{m} = 1$ kg/s.

A discretization of $N_{ax} = 7$ and $N_{rad} = 3$ has been used.

Model	**Equations**	**Simulation time [s]**
$Mod1$	1672	10.9
$Mod2$	1292	5.6

Table 4.10: Comparison of $Mod1$ and $Mod2$ in terms of number of equation and simulation time

A significant reduction in terms of equation number and simulation time is obtained. By consequent, $Mod2$ should be used in large scale systems and/or in systems simulated over a long period of time.

4.1.7 Partial load

In many practical cases, partial load of the PCM storage is realized. Meaning that a part of the phase change material remains in its initial state (solid for partial melting and liquid for partial solidification) during an charging-discharging process.
For a better understanding of the melting front evolution in partial loading case, a simple simulation has been done:
The storage inlet temperature remains at a certain time over the melting temperature ($T_m = 400$ K) at 410 K and then, before reaching a SOC of 1, falling down to 375 K.

Figure 4.12 visualizes the evolution of the SOC for different time cuts. Figure 4.13 shows the temperature evolution.

The sub-figures at minute 28 visualize really well the two melting fronts, which merge together afterwards.
This partial load experiment has been done for a better understanding of the internal processes, necessary for the single-node model development.

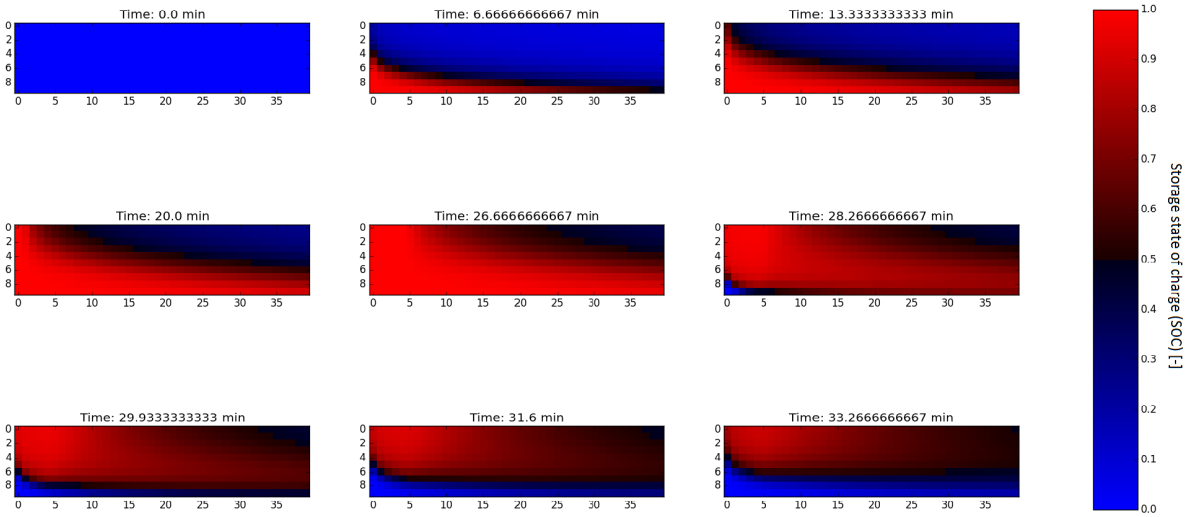

Figure 4.12: Partial loading state of charge (SOC) 2D visualization. Two simultaneous melting fronts can be observed at min 28.

4.2 Single node PCM storage model

As for the discretized model, we will fit the storage outlet temperature of the model to the measurement by optimizing the storage parameters.
As described in section 3.2.2, the simulations are based on the sigmoid function of $cp(T)$ (see *Mod2* in section 3.1.3).
Three different heat transfer models were introduced *version1, version2, version3*. For this model, **partial loading** data is used for the parameter determination, because of the direct influence of the state of charge on the heat transfer. Using the partial load data, a more significant variability on the SOC is obtained, which is advantageous for the heat transfer parameter optimization.

Figure 4.14 shows the measurement data for the partial load experiment. Storage inlet (blue) and outlet (red) temperatures are represented.

Knowing the exact analytical equations of the heat transfer coefficient AU, the relations between its parameters are perfectly known. That's why no

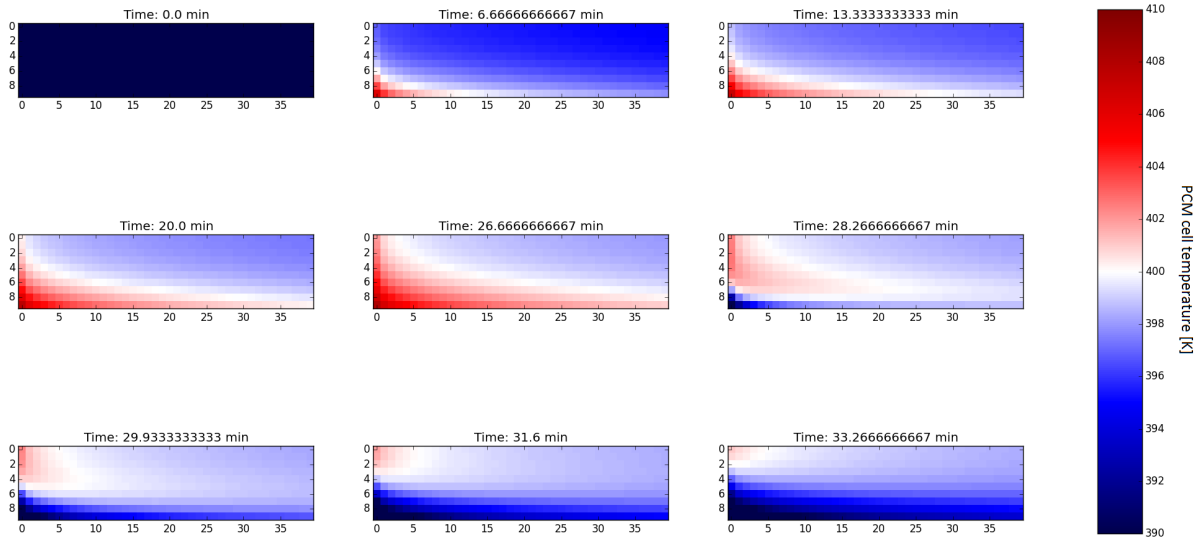

Figure 4.13: Partial loading temperature visualization. At min 28 two melting fronts (the upper results from the melting and the lower from the solidification) can be observed

statistical analyse with correlation determination is done here.

4.2.1 Heat transfer version 1

As described in section 3.2.1 it turned out, that the heat transfer coefficient U_2 is a function of SOC described by Eq. (3.47). A simple charging experiment using the discretized model has been realized to generate $U_2(SOC)$. Then, a parameter optimization has been done to fit *version 1* Eq. (3.47) on this curve.
The results are given in table 4.11.
The parameter $a4$ represents the constant part of U_2. It corresponds nearly

Version 1					
Parameter	a1	a2	a3	a4	a5
Value	0.000315	0.319011	217.80882	0	76.68

Table 4.11: Start parameters for the heat transfer in version 1

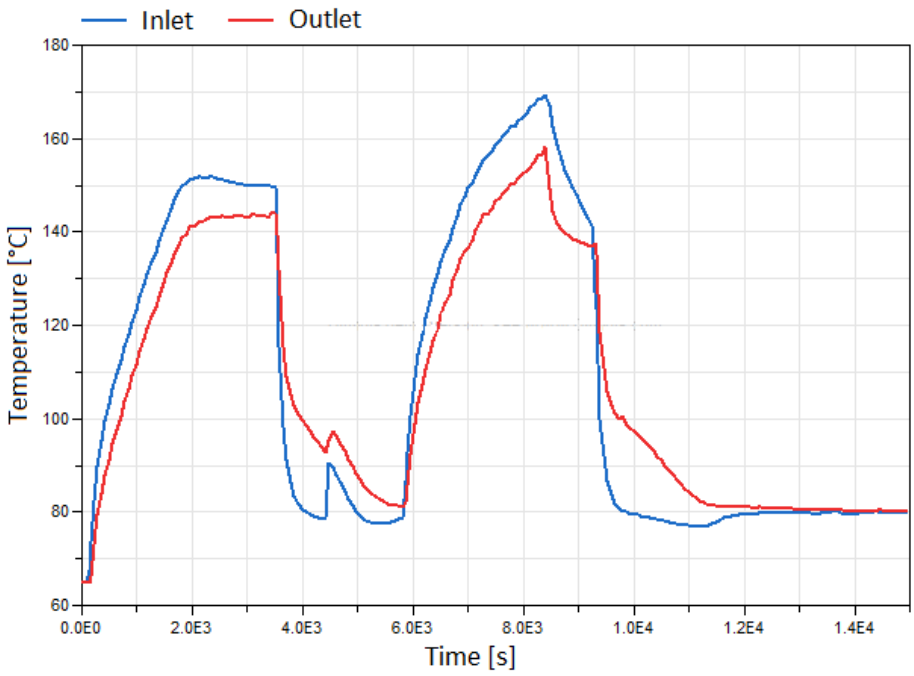

Figure 4.14: Partial loading measurement data

to the value of U_2 if SOC is equal to 1. The curve fitting gives a value of zero for this constant term. But in reality heat transfer is different from zero if the SOC is 1, due to the sensible heat capacity of the PCM. Therefore there is a need of this constant term, characterizing the sensible heat transfer if SOC is equal to 1.

Using these parameters, the storage power is calculated by Eq. (3.45). We compare it to the generated power by the discretized model. The result is given in figure 4.15.

We take these parameters as starting values for further parameter determination calculations.

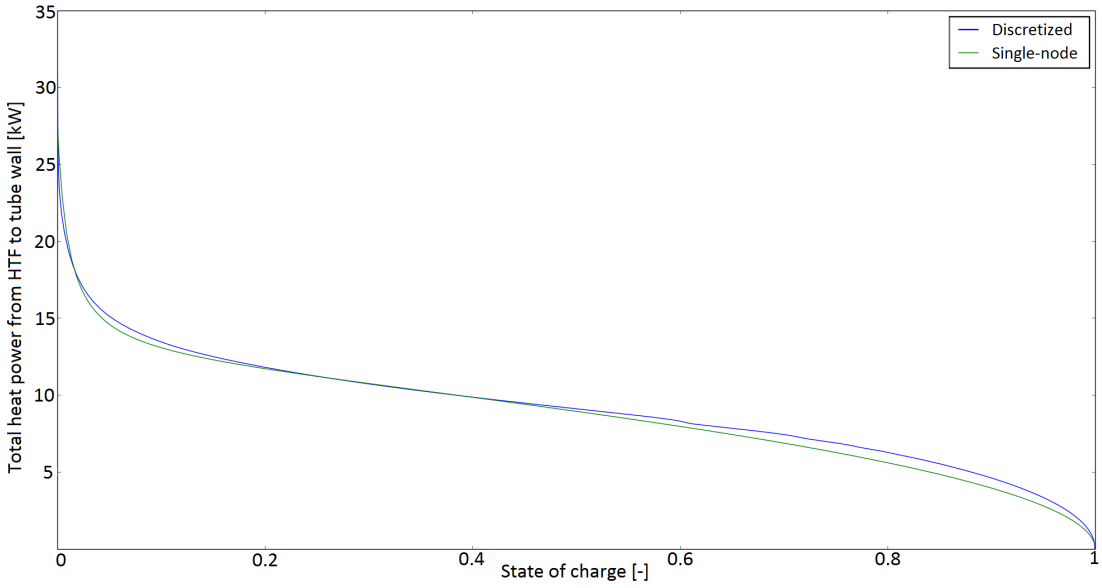

Figure 4.15: Comparison of the storage power in the case of discretized and one node model.

4.2.2 Model validation

The other heat transfer versions are simplifications of the version 1. They don't match exactly to the heat transfer curve of the discretized model but are more generic. In the following we will see if this simplification results in marginal differences in terms of outlet storage temperature and storage power.

Table 4.12 summarizes the optimized PCM parameters for single node model.

As already mentioned in section 3.2.3, there are only four PCM parameters in the single node model, because the thermal conductivity λ_P is included in $U_2(SOC)$.

In a first time the heat transfer parameter estimation has been done on U

Parameter	$c_{p,P}$	L	T_m	ΔT
Unit	$\mathrm{kJ\,kg^{-1}}$	$\mathrm{kJ\,kg^{-1}}$	°C	K
Value	1.339	229.518	130.774	28.960

Table 4.12: Estimated single-node model PCM parameters for the individual fitting of data from the partial load experiment

only, by specifying the total heat exchange surface, equal to $A = 7.634m^2$.

Version 1					
Parameter	a1	a2	a3	a4	a5
Value	0.000207	0.023703	115.869	45.30031	96.4999

Version 2				
Parameter	a1	a2	a3	a5
Value	963.161499	1.157108	156.258038	96.4999

Version 3				
Parameter	a1	a2	a3	a5
Value	530.504373	1.929636	82.431222	96.4999

Table 4.13: Estimated parameters of the heat transfer coefficient U in version 1, 2 and 3 for the individual fitting of data from the partial load experiment

Figure 4.16 shows the optimized storage outlet temperature (red) and the measurement data (blue) with the parameter values in table 4.13 (U). The second sub-figure gives the delivering power of the storage. This simulations have been done with heat transfer **version 1** (see Eq. (3.47)).
Both simulation curves fit the measurement data very well, which certify the choice of the heat transfer equation.

Furthermore an interesting observation can be made in this figure. It can be seen that the absolute maximum power in loading mode (negative) is lower than in unloading mode (positive). This phenomena can be explained by figure 2.8, where the cooling (unloading) apparent heat capacity possesses a

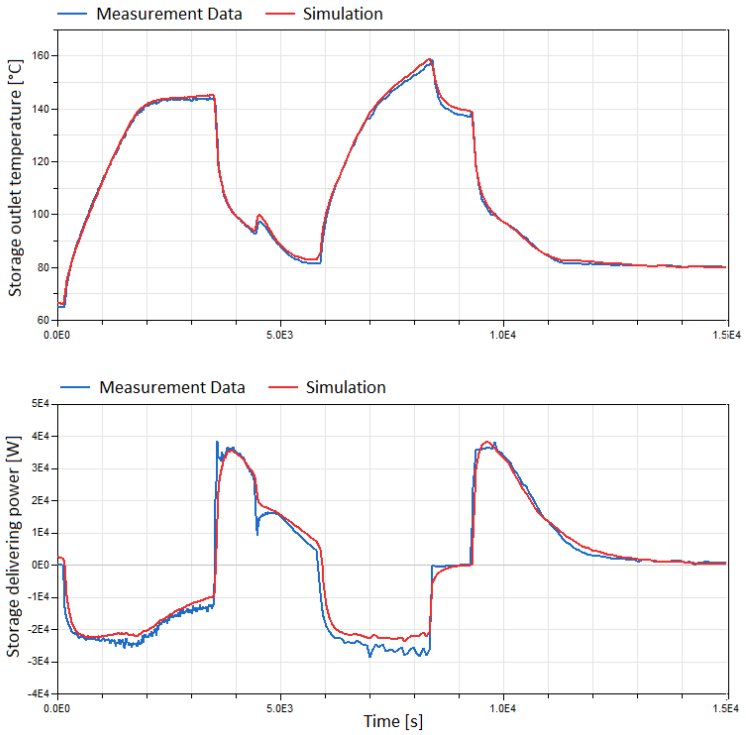

Figure 4.16: Measurement and Simulation: 1. Storage outlet temperature, 2. Storage delivering power

higher peak value than for the heating (loading) process.

As the parameter determination has been done on partial load data, it is interesting to show the storage state of charge (see figure 4.17).

It shows well that the SOC does not reach its maximum during the experiment.
Figure 4.18 shows the system variables needed for the heat transfer calculation. The first sub-figure represents the *loading* boolean, introduced in Eq. (3.52) which indicates if the storage is in loading or unloading situation. Using this information the x variable defined in Eq. (3.46) is calculated. Finally, the heat transfer coefficient U_2 is computed using Eq.(3.47) (*version 1*).

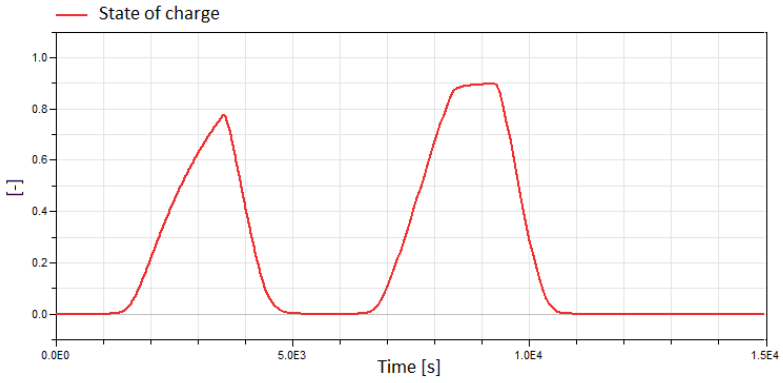

Figure 4.17: Storage state of charge for partial load experiment. It does not reach the maximum value due to partial loading.

4.2.3 Heat transfer versions: Comparison

After examination of the simulation results of heat transfer version, a direct comparison between the three version will be done in terms of outlet temperature, power and heat transfer coefficient.

First, we start with the estimated heat transfer parameters for the three versions in the case of the parametrization of U. The same results can be found with the parameters for AU. To have a better understanding of these parameters, the heat transfer coefficients of the three versions computed with the different parameter values of table 4.13 are plotted in figure 4.19.
In opposite to version 1, the other two version consider more or less linear dependency of U_2 on SOC. In the following, we will analyse its impact on the simulation results.
The simulation results can be found in figure 4.20 and 4.21 .

We can conclude, that beside the fact that the three heat transfer version have quite different shapes, the resulting storage characteristics don't diverge in significant ways. The simplified models 2 and 3 are by consequent as reliable as version 1.

Beside the simplicity of the developed sing-node grey-box model, reliable results have been obtained. However, this model is only intended for the

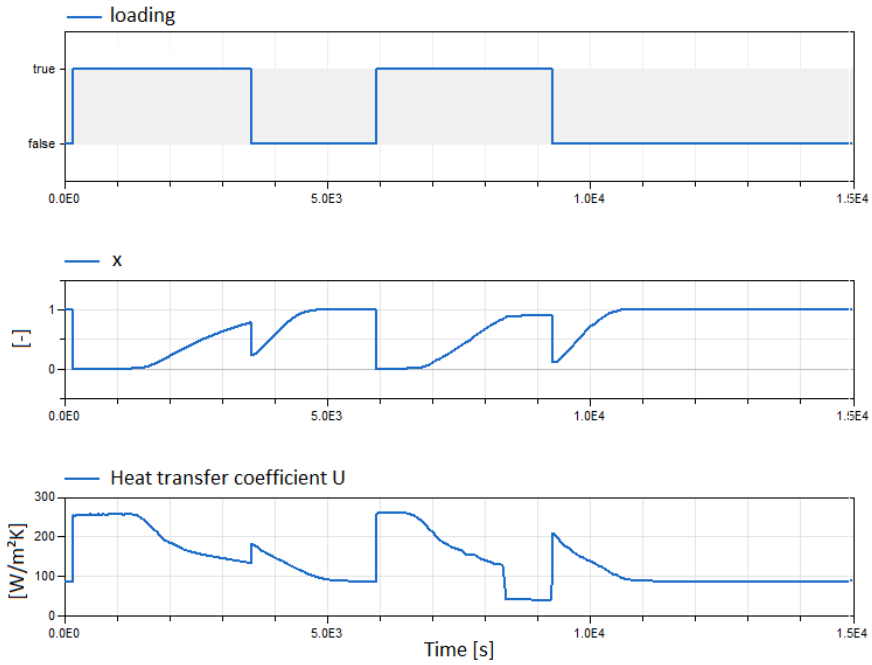

Figure 4.18: Heat transfer variables for the partial load experiment. When there is a transition in the loading boolean, the the heat transfer coefficient U sees a significant increasing. It is physically based on the fact that a new melting front appears near to the HTF tubes causing a high heat transfer rate.

prediction of storage outlet temperature profiles and cannot be used for parameter estimation and storage construction.

4.2.4 Charging and discharging experiment

To compare the single node model to the discretized one, the charging and discharging experiment introduced in section 4.1.3 and 4.1.4 has been made using the single-node grey-box model. Figure 4.22 shows the results for the charging experiment and figure 4.23 represents the discharging process:
Figure 4.24 shows the direct comparison between the discretized (blue), the one node model (red) and the measurement data (green) for the melting experiment.
We can conclude, that in terms of storage outlet temperature the single-

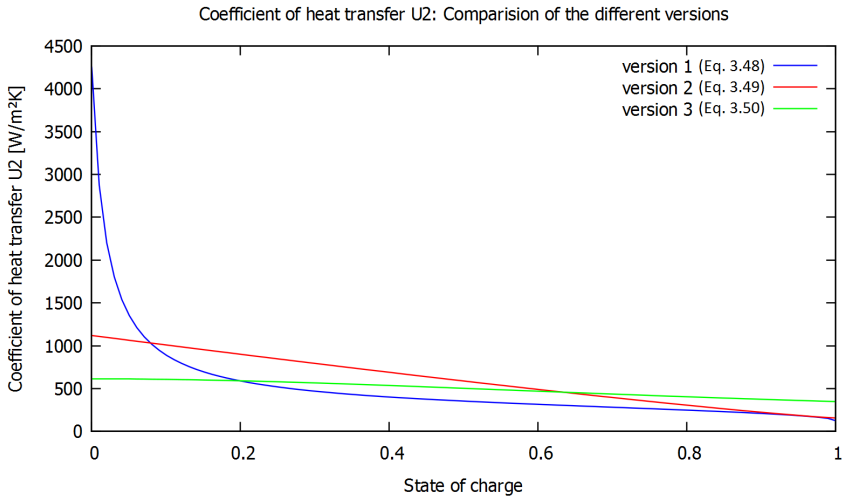

Figure 4.19: Comparison of the heat transfer coefficients as a function of SOC for the three versions

node model provides as reliable simulation results as the discretized model. The major advantage of the latter model concerns the physical meaningful parameters and the predication of the internal PCM fluid state variables which are necessary for storage design.

4.2.5 Comparison with discretized model

In the following the differences in terms of total equation number and simulation time will be analysed, as it has been done for $Mod1$ and $Mod2$ in section 4.1.6. Table 4.14 resumes the number of equations and the CPU simulation time for the melting experiment with $\dot{m} = 1\,kg/s$. A discretization of $N_{ax} = 7$, $N_{rad} = 3$ has been used for the discretized model.

The single node model can be further simplified by resuming the system equations in a single component. No subcomponents are needed, reducing significantly the number of equations and by consequent the simulation time. The corresponding results are listed in the line "Single-node simple".

A markable reduction in terms of equation number and simulation time is obtained between the discretized and single-node models. Their implemen-

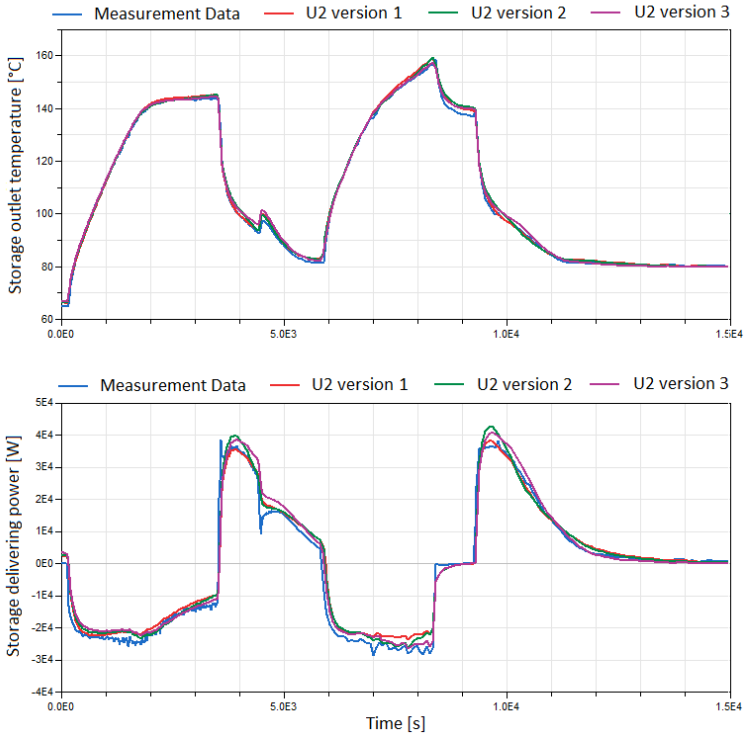

Figure 4.20: Comparison of the heat transfer versions (Thermal storage characteristics): 1. Storage outlet temperature, 2. Storage delivering power. The different heat transfer versions show no marginal differences in terms of storage characteristics, despite the unequal shapes of $U_2(SOC)$ in figure 4.19.

Model	**Equations**	**Simulation time [s]**
Discretized	1292	5.6
Single-node	209	3.1
Single-node simple	97	2.3

Table 4.14: Comparison of $Mod1$ and $Mod2$ in terms of number of equation and simulation time

tation is advantageous for simple system analyses containing PCM storages, where no detailed information about the storage interior state is needed.

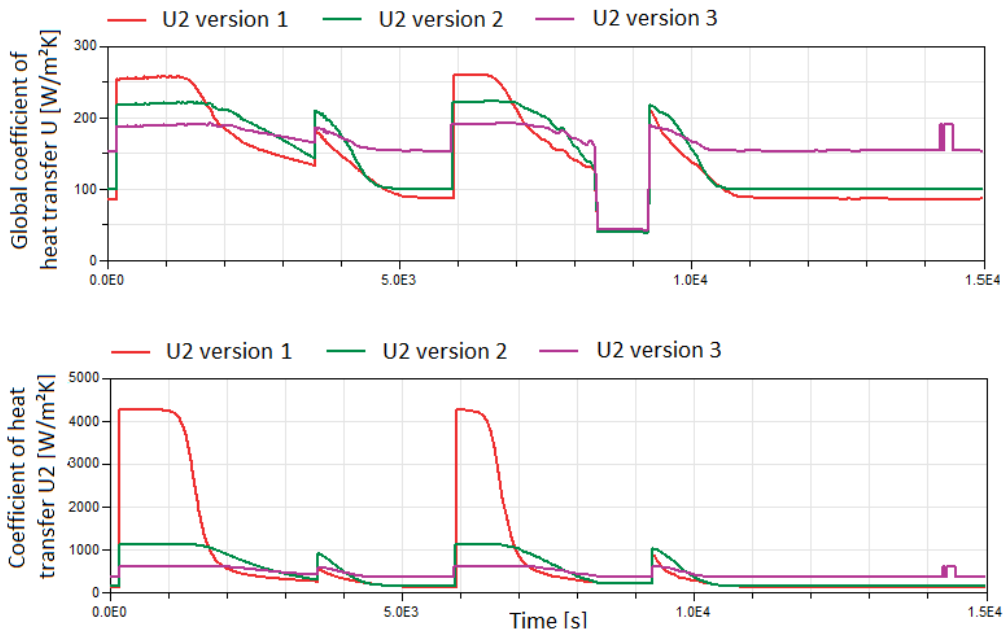

Figure 4.21: Comparison of the heat transfer versions (Calculation of U2): 1. x variable, 2. Heat transfer coefficient U2. Higher peaks for version 1 can be observed due to its high value at SOC=0. Nevertheless, it does not marginally influence the results, see figure 4.20.

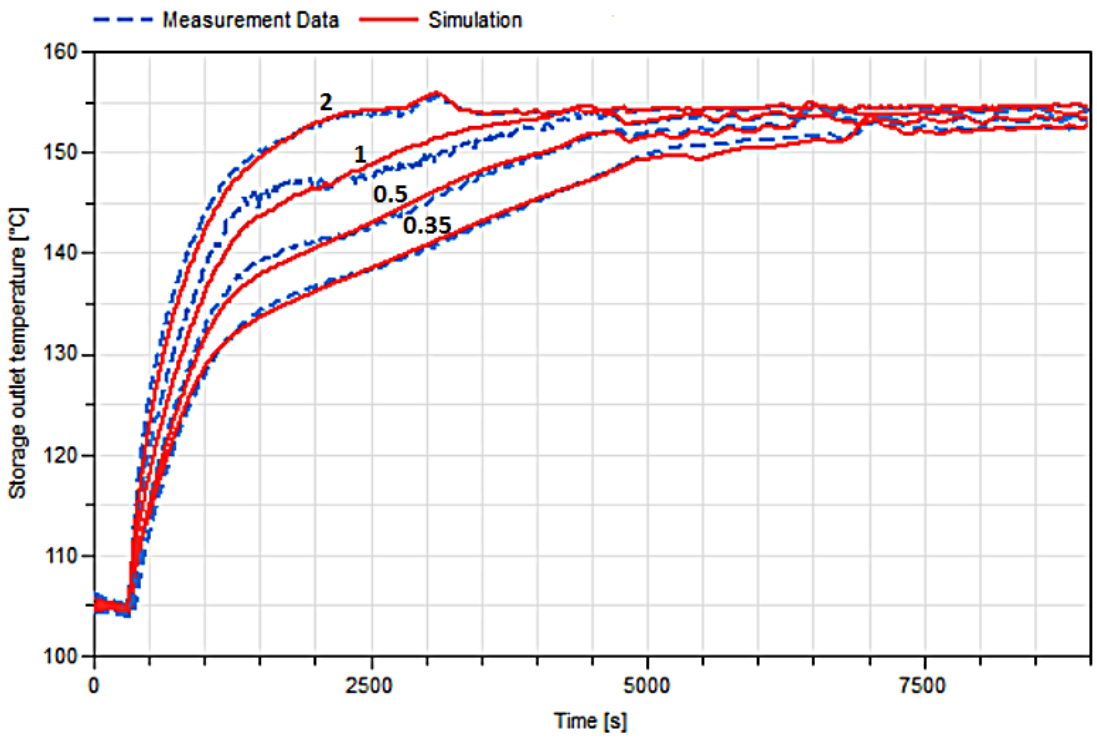

Figure 4.22: Experimental data and model predictions of the single-node model with mass flow rates 0.35 to 2 kg /s for the charging process

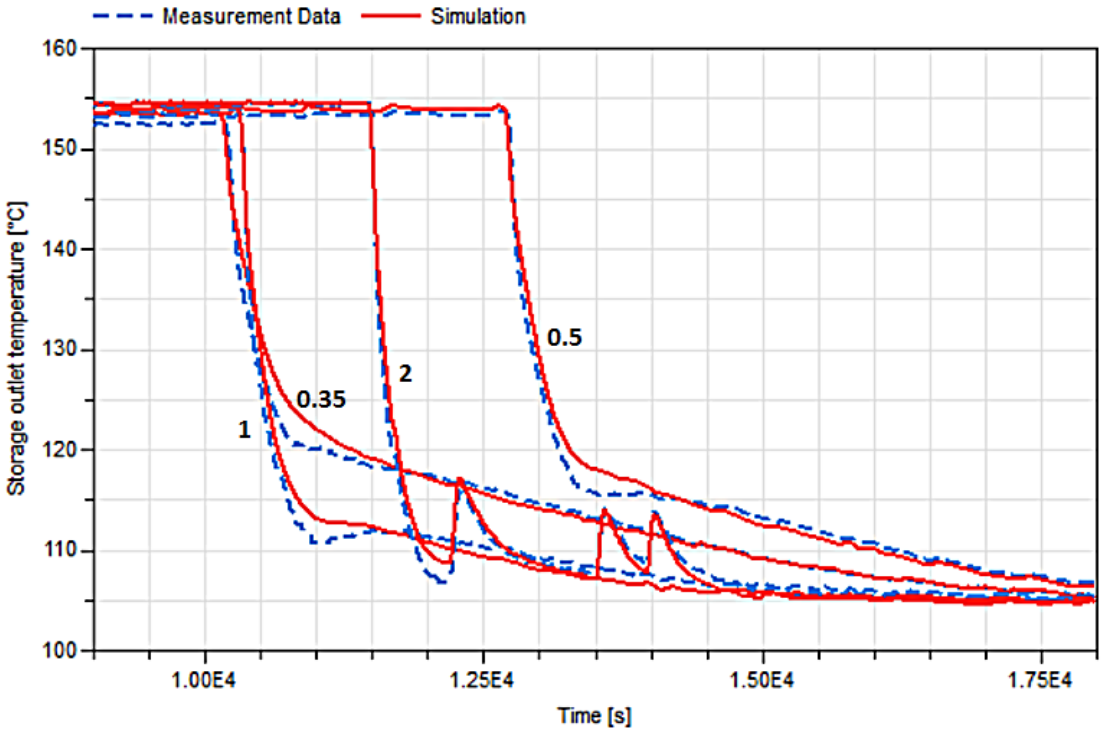

Figure 4.23: Experimental data and model predictions of the single-node model with mass flow rates 0.35 to 2 kg /s for the discharging process

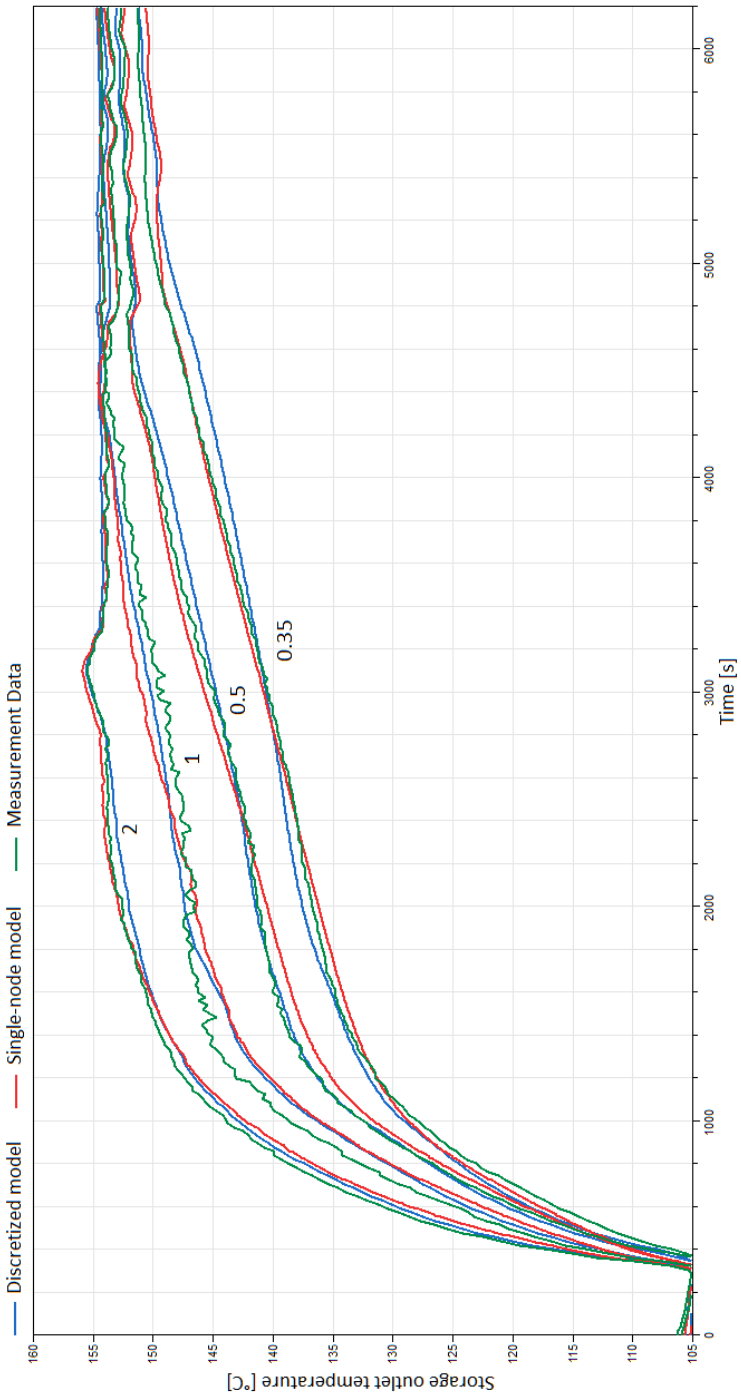

Figure 4.24: Comparison between the discretized and one node model for the melting experiment. Beside the simplicity of the sing-node model, good simulation results have been obtained.

Chapter 5

Model application: CSP - biomass system

As an application of the discretized white-box PCM storage model described in the previous chapters, the storage has been implemented into the system simulations of the CSP-biomass plant investigated in the BRICKER project.

Figure 5.1 shows the system model in Dymola. The PCM storage is connected in series right to the solar field outlet. A parallel connection could also be imagined, but this would claim an additional control strategy. The series connection has the advantage to store immediately any excess in solar power and to smooth the solar field outlet temperature profile.

5.1 PCM storage sizing

For the storage sizing a reference solar irradiation on the solar collectors has been chosen (figure 5.2).

Without a thermal energy storage, solar power is wasted when there is an excess of solar insulation due to the defocusing of the solar collectors. Basing on a reference day with given solar irradiation, this excess of solar power is of an amount of 706.872 kWh. It corresponds to the difference of absorbed energy of the solar field in the case of focusing and defocusing mode. It counts for 17% of the total amount of energy produced by the solar field over the reference day. For this simulation the heating demand was reduced to be

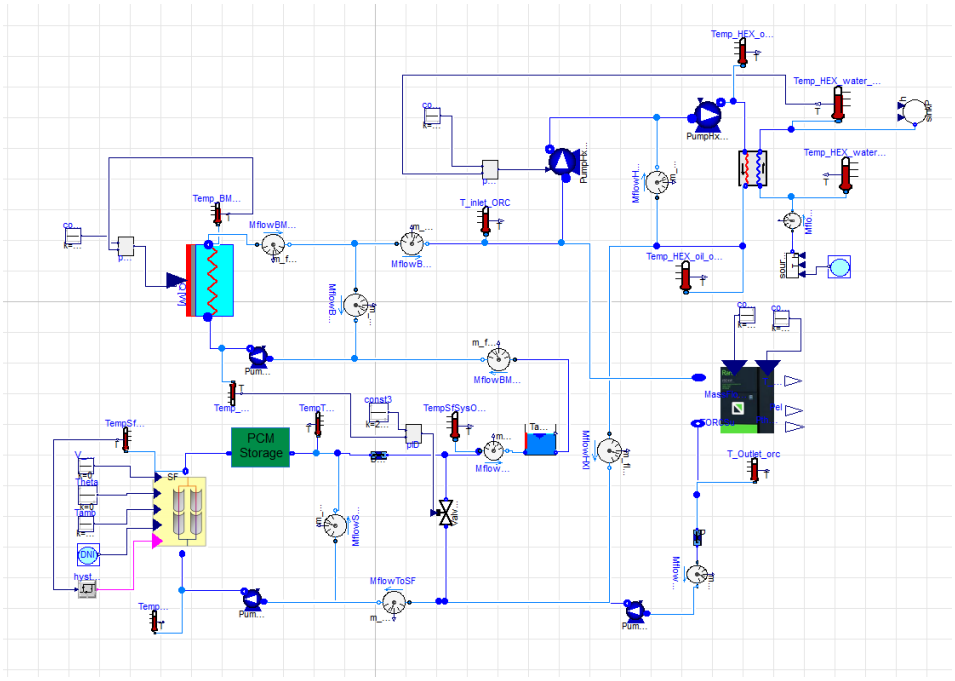

Figure 5.1: CSP-biomass system model in Dymola with the implemented PCM storage

zero.
The thermal energy absorbed is represented as a function of time in figure 5.3.

The purpose of the thermal storage is to limit the temperature at the biomass inlet, so that is does not exceed its maximum temperature. By consequent the bypass regulation of the solar system has not been activated and the temperature at the solar field outlet remains in acceptable range, unlike in the case without storage, where the defocusing is activated due to overheating of the thermal oil caused be the recirculation in the bypass.

5.1.1 Melting temperature

Besides the geometrical parameters of the storage, also the parameters of the phase change material, introduced in section 3.1.3 have to be chosen carefully in order to improve the utilization of the storage.

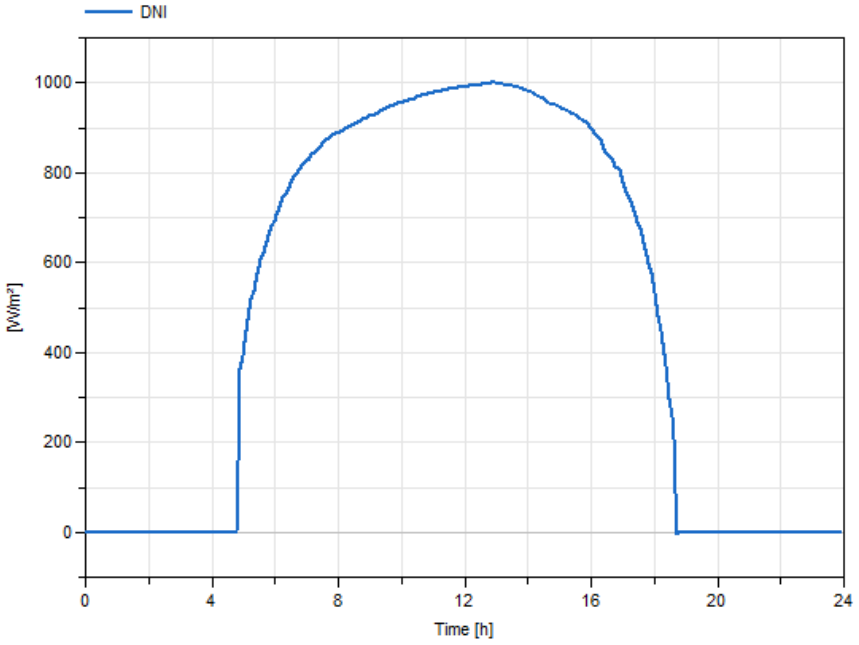

Figure 5.2: Reference solar irradiation (DNI) on solar collectors in kW

In this simplified study, we vary only the melting temperature T_m. All other material parameters have been taken from the parameter determination of the lab scaled storage. The parameters can be found in table 4.7. The chosen PCM model is *Mod1*, using the Sigmoid distribution.
In order to avoid the automatic defocusing of the solar field collectors, the melting temperature has to be lower than the defocusing set point of 228 °C and higher than 170 °C, the outlet temperature of the ORC. It is also necessary that these temperatures are situated out of the range $[T_m - \frac{\Delta T}{2}; T_m + \frac{\Delta T}{2}]$, where ΔT is the transition width of PCM melting. Otherwise, parts of the PCM will remain in its solid or liquid state, depending on which temperature is situated in the previous range. Consequently, the storage capacity is not fully used there is a squandering of storage volume and money.
After several simulation with different melting temperatures it turned out that with a melting temperature of 200 °C satisfying results have been found.

Knowing the energy to be stored in the PCM storage, its dimensions of have been determined in order to obtain a SOC near to 1 after the storage inlet

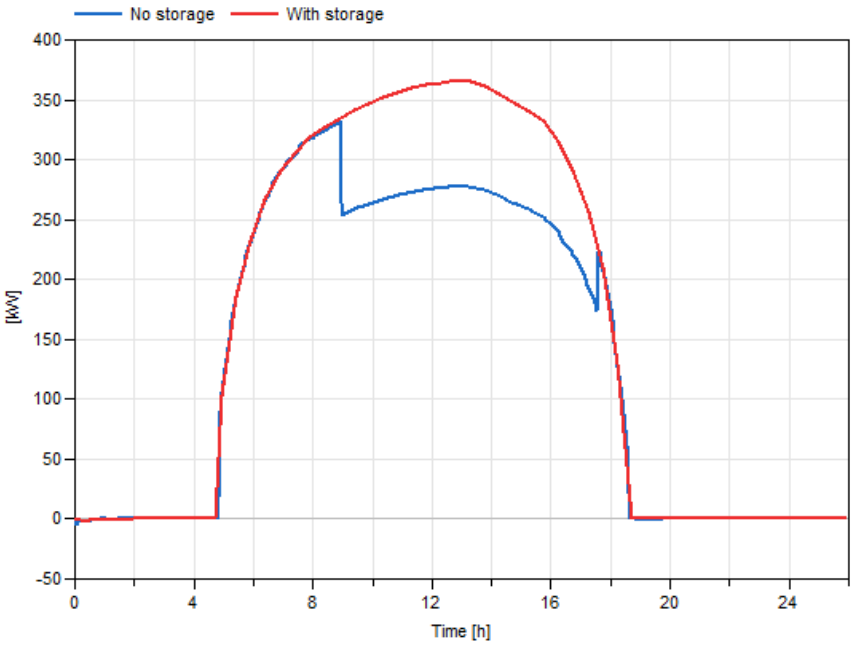

Figure 5.3: Solar field absorbed power with and without storage. The difference corresponds to the amount of energy necessary to store.

temperature has reached its maximum and felt down to the melting temperature of 200 °C. It is clear that the bigger the storage, the smoother the outlet temperature which is favourable for the biomass and ORC systems. But to limit the investment costs, the size is limited by the energy need to be stored.

Figure 5.4 shows the evolution of storage inlet and outlet temperature as well as the state of charge used for the storage sizing.

The corresponding optimized sizes are presented in table 5.1:

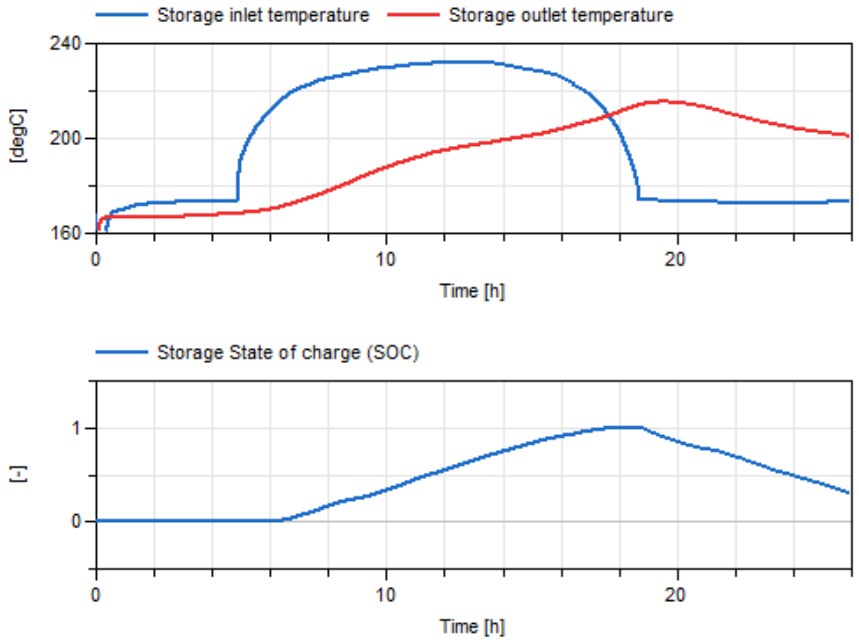

Figure 5.4: Storage inlet/outlet temperature and SOC as a function of time. The PCM storage is designed to reach SOC=1 (fully charged) after the irradiation peak.

Symbol	Dimension	Size	Dimension
A_{ap}	Cross section	4.7	m^2
l_{hex}	Length	9	m
V	Volume	42.3	m^3

Table 5.1: Storage dimensions

5.2 System simulation

To analyse the effect of the PCM storage in the whole system, simulations over 3 days have been made. Irradiation data (DNI) is taken from the Solar One power plant in Nevada, US from the 21/06/2008 to the 24/06/2008, having almost the same irradiation magnitudes as the at the plant location in Spain. Heating demand data of the building is also provided.

In figure 5.5, the system behaviour without a storage is represented. The heating demand is also considered by a thermal heating load on the oil-water heat exchanger HXI.

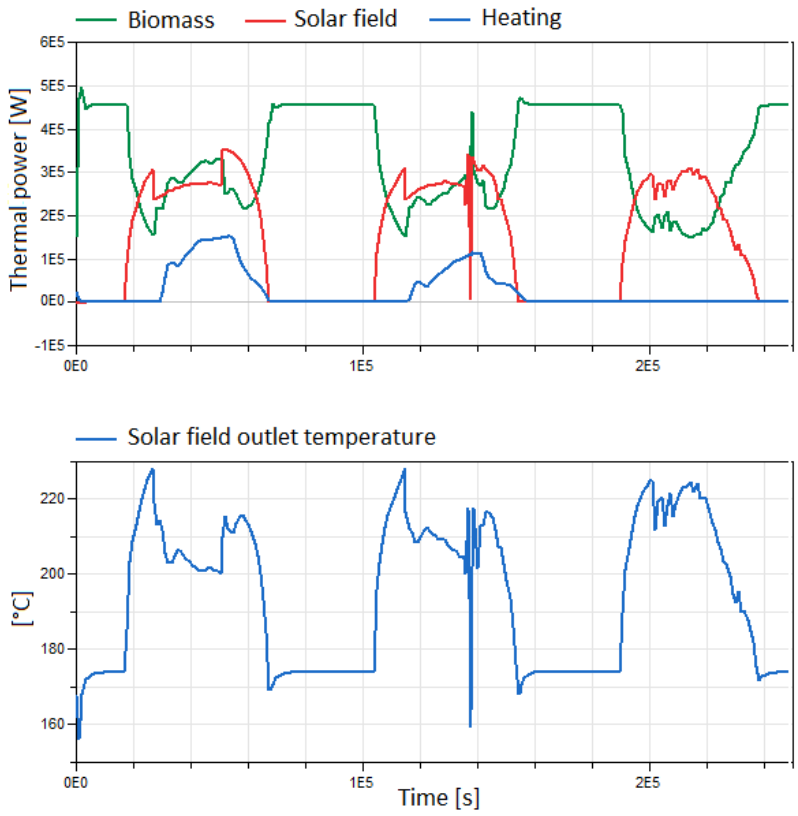

Figure 5.5: System simulation without storage implementation (with heating demand): 1.System powers 2.Storage outlet temperature. High fluctuations of the system parameters can be observed.

Figure 5.6 shows the effect on the biomass system after the implementation of the storage. Also the outlet temperature and the state of charge are represented to check if the storage sizing is satisfying.

One can observe that the storage outlet temperature remains in the acceptable range and by consequent no defocusing of the solar field collectors occurs.

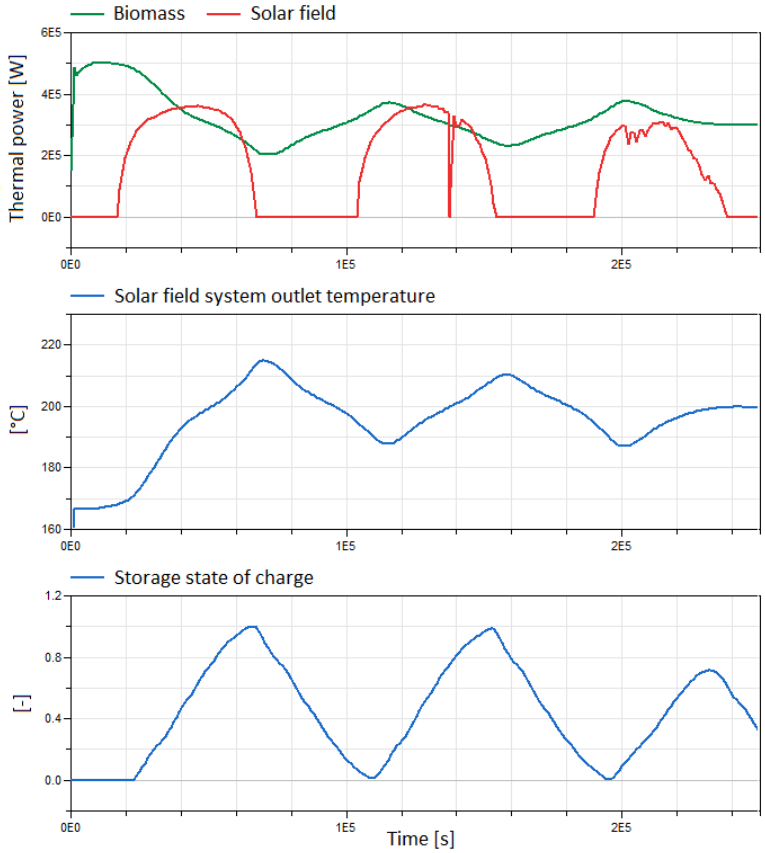

Figure 5.6: System simulation with storage implementation (No heating): 1.Biomass and solar field power 2.Storage outlet temperature 3.State of charge. Smoother variations can be observed and the storage capacity is fully used during the first two days.

Furthermore we obtain a state of charge that varies between 0 and 1 in 24 hours due to the appropriate dimensions of the storage.

The following figure 5.7 shows the effect of the additional heating demand:

The additional consummation of thermal power on the heating heat exchanger reduces the total energy need to be stored in the storage. Therefore the state of charge does not reach the maximum at the end of the first day, like it was in the case without heating.

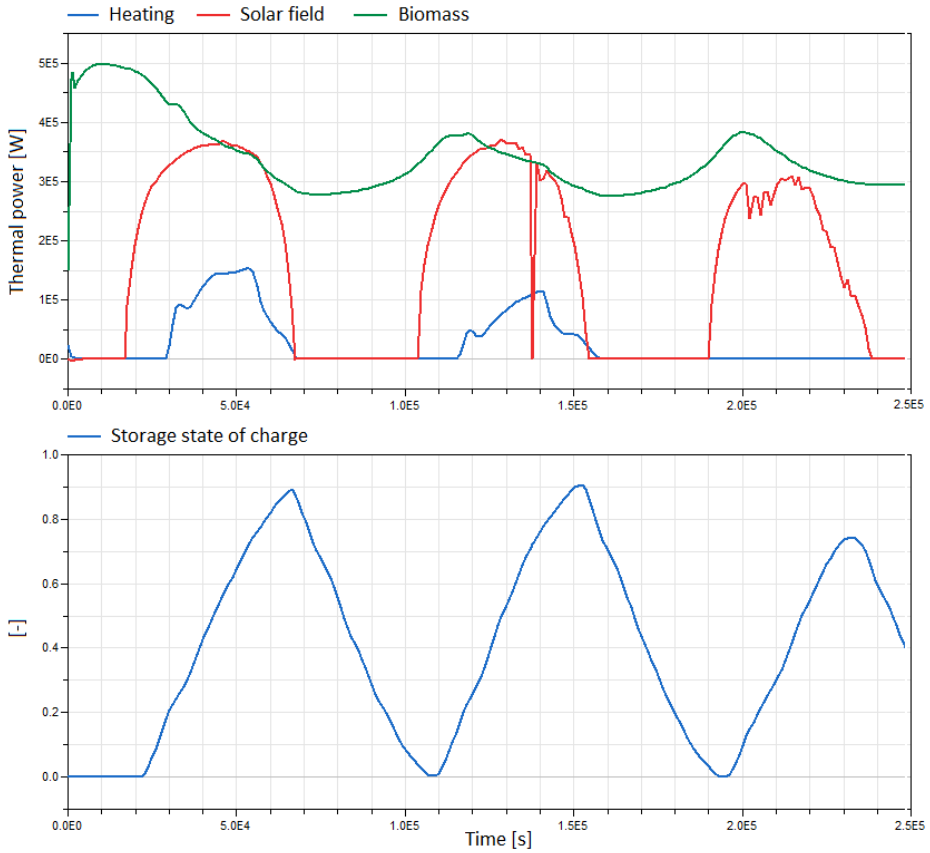

Figure 5.7: System simulation with storage implementation (with heating demand): 1. Biomass and solar field power 2. State of charge. Due to the heating demand, the energy to store is lower, so the storage state of charge does not reach its maximum value of 1.

For the better illustration of storage implementation effect on the system, figure 5.8 resumes some system variables and compares them in the case of the integration of the storage and without it.

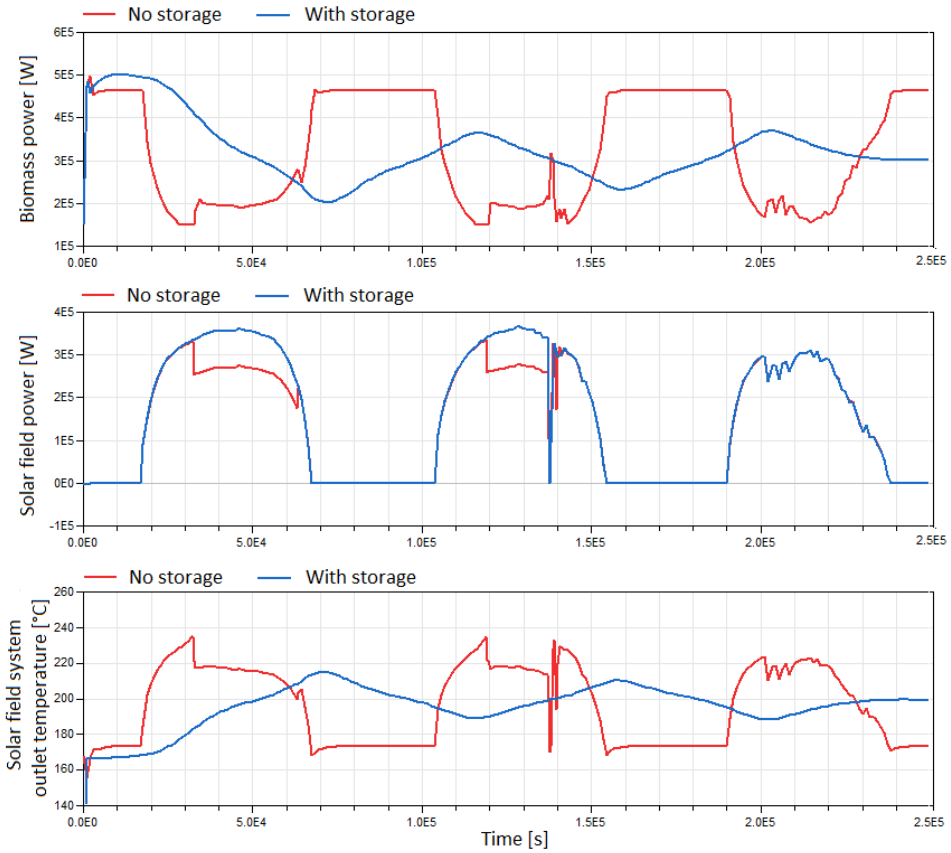

Figure 5.8: Effect of the PCM storage implementation: 1.Biomass power 2.Solar field power 3.Solar field outlet temperature. Smoother temperature and power profiles can be observed

5.2.1 Solar fraction

Using a storage system the excess of solar energy normally lost by defocusing, can be stored and will lead to a higher solar fraction, defined by:

$$SF = \frac{E_{SF}}{E_{tot}} = \frac{E_{SF}}{E_{SF} + E_{BM}} = \frac{\int \dot{Q}_{SF} dt}{\int \dot{Q}_{SF} dt + \int \dot{Q}_{BM} dt} \tag{5.1}$$

The calculated solar fractions over the 3 days are given in table 5.2.

The difference in heating cases result in the additional biomass heat needed

	No heating	Heating
No storage	0.2967	0.2940
With storage	0.3229	0.3131
Relative difference	**+8.8 %**	**+6.4 %**

Table 5.2: Solar fractions

to balance the additional heating demand.

5.3 Comparison with a thermocline storage

5.3.1 Thermocline storage: Generalities

A thermocline storage is composed of a single tank, in which the hot heat transfer fluid at the top is separated by the use of buoyancy forces to the cold fluid at the bottom. It results that a thermal gradient called a thermocline occurs between the two zones. In regard of reducing the investment costs of the storage, it is possible to add low-cost solid filler materials to the tank. Doing that, up to 80 % of the heat transfer fluid can be replaced, causing no loss in energy storage efficiency [16].
The solid materials that can be used for high temperature heat storages are metals, sand, bricks, rocks, concrete and ceramic [13].

5.3.2 Results

Using the thermocline storage model of the ThermoCylce library, the materials used for the comparison are **Brick** and **Iron**.

As for the PCM storage, the dimensions of the thermocline tanks are sized on the the reference irradiation in figure in order to avoid collector defocusing. The amount of energy to store is about 706.872 kWh.
We found for the brick storage a necessary volume of 80 m^3 and for the pure iron 55 m^3. The difference in volume results in a higher specific heat capacity of the pure iron. In both cases a filler porosity of 0.4 has been taken [13].

Figure 5.9 and 5.10 resume the effects of the different storage methods on

the system. Figure 5.9 considers no heating demand.

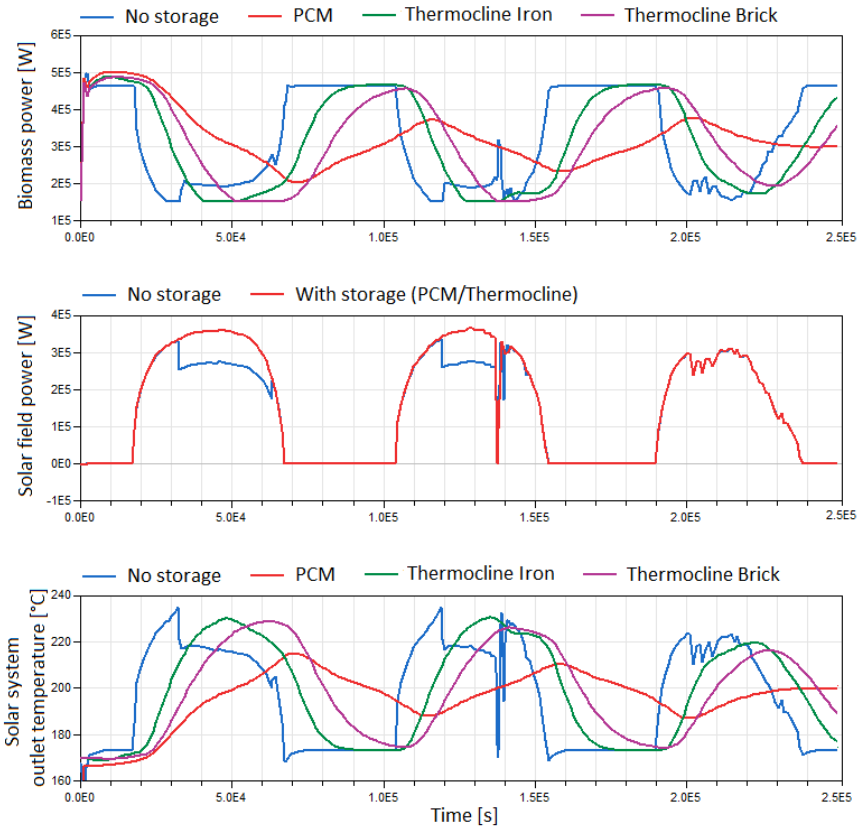

Figure 5.9: Storage comparison (No heating demand): 1.Biomass power 2.Solar field power 3.Solar field outlet temperature

Beside the fact, that the PCM storage need a lower volume for the same energy quantity stored, it also provides smoother temperature and biomass power profiles.

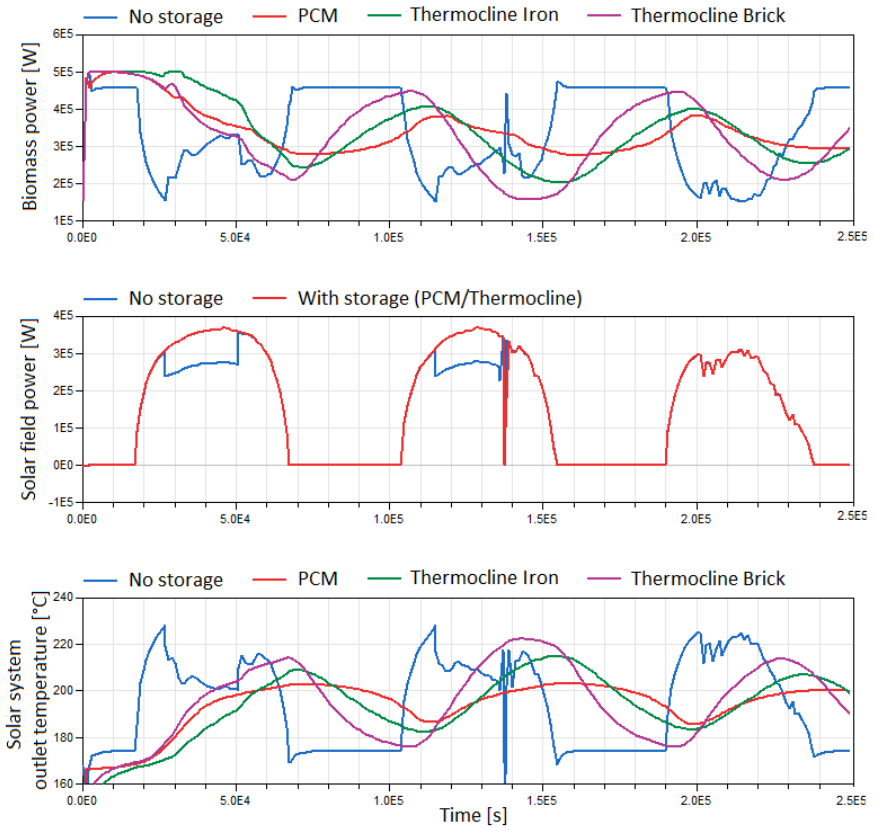

Figure 5.10: Storage comparison (With heating demand): 1.Biomass power 2.Solar field power 3.Solar field outlet temperature

5.4 System simplification

After the implementation of the PCM storage, it turned out that due to the adequate sizing, the temperature at the storage outlet never exceed its maximum which would lead to the opening of the bypass valve on the solar field. By consequent this protective mechanism for the biomass system becomes useless. A simplification of the system can be done by omitting the bypass valve and the recirculation tube on the solar field.
In our numerical model, this reduces the number of equation by 62 and a gain in simulation time of 270 second for the simulation of the 6 days.
Figure 5.11 shows the simplification in the system.

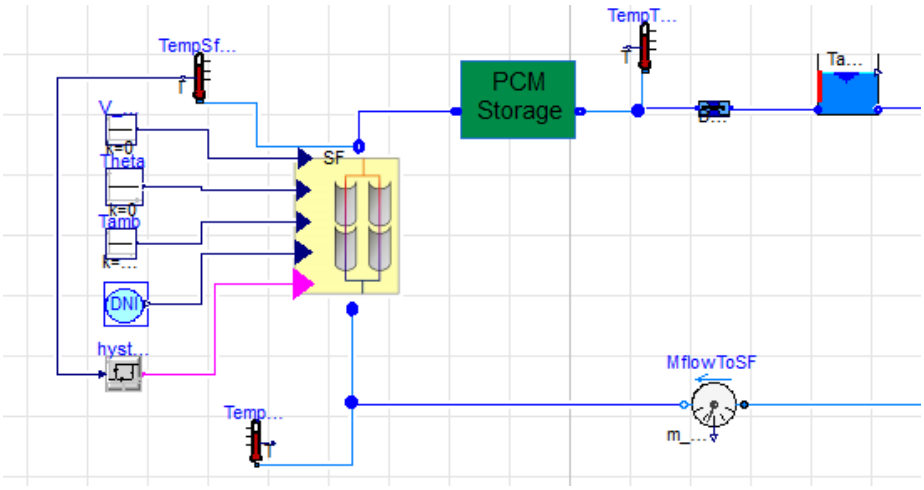

Figure 5.11: Simplified solar field system with PCM storage

Nevertheless, this simplification can only be done with the PCM storage. In fact, the thermocline storages are only providing a shift in time of the temperature profiles, as we can see in figures 5.9 and 5.10. The temperatures maxima are nearly of the same magnitude as without storage. Therefore, even with storage the maximum inlet temperature of the biomass will be exceeded and the bypass vale will by opened.
Compared to the case without storage, this does not occur when the solar irradiation is maximum, so no defocusing is needed.

5.5 Conclusion

It turned out that, compared to thermocline storages, a PCM storage has the advantage to provide smooth temperature and biomass power profiles with a relative small storage volume. In addition the system can be significantly simplified which reduces simulation time and investment costs.

Chapter 6

Conclusion

Two numeric models, a white-box discretized and a grey-box single node mode, of a latent heat thermal energy storage and their validation on experimental measurement data of a laboratory storage prototype have been presented in this work. The discretized model consist in a complex model destined to predict real physical parameters for storage design. The single-node model, in contrast, uses a simple approach for system simulation and curve fitting where internal storage thermophysical processes are not necessary to be simulated. The phase change material behaviour have been characterized by an apparent heat capacity method described by parameter sets of different PCM model approaches.
The validation of both model types on experimental data, showed that the simulation prediction fit the measurement values very well. Further statistical analyses proved the adequate choice of the parameter sets and showed the differences in PCM models. A comparison between the PCM models in terms of optimized parameter results and simulation time has been provided, as well as a comparison in simulation time between discretized and single-node model approach.
The validated discretized LHTES model has finally included in the CSP-biomass system to improve its solar fraction. It turned out that the use of a latent heat storage provides both, the advantage to store eventual solar power excess, increasing the solar fraction, and generating a smooth biomass inlet temperature profile causing less fluctuating boiler power.

Bibliography

[1] http://www.bricker-project.com/. [Online; accessed 11-July-2016].

[2] http://www.thermocycle.net. [Online; accessed 29-July-2016].

[3] http://www.ewp.rpi.edu/hartford/~ernesto/S2006/CHT/Notes/ch03.pdf. [Online; accessed 14-April-2016].

[4] http://www.docs.scipy.org/doc/scipy/reference/tutorial/optimize.html. [Online; accessed 2-March-2016].

[5] http://www.simulationresearch.lbl.gov/modelica/buildingspy/simulate.html. [Online; accessed 2-March-2016].

[6] M.B. Abd-el Malek and M.M. Helal. Group method solution for solving nonlinear heat diffusion problems. *Applied mathematical modelling*, 30:930–940, 2006.

[7] A. Abhat. Low temperature latent heat thermal energy storage: heat storage materials. *Solar Energy*, 30:313–332, 1983.

[8] F. Agyenim, N. Hewitt, P. Eames, and M. Smyth. A review of materials, heat transfer and phase change problem formulation for latent heat thermal energy storage systems (lhtess). *Renewable and Sustainable Energy Reviews*, 14:615–628, 2010.

[9] H.D. Baehr and K. Stephan. *Wärme- und Stoffübertragung, Vol. 3.* Springer, Berlin, 1994.

[10] R.B. Bird, W.E. Stewart, and E.N. Lightfoot. *Transport phenomena.* John Wiley, 2007.

[11] M. Costa, D. Buddhi, and A. Oliva. Numerical simulations of a latent heat thermal energy storage system with enhanced heat conduction. *Energy conversion management*, 39:319–330, 1998.

[12] A. Desideri, S. Amicabile, F. Alberti, S. Vitali-Nari, S. Quoilin, L. Crema, and V. Lemort. Dynamic modeling and control strategies analysis of a novel small csp biomass plant for cogeneration applications in building. In *Solar World Congress 2015, Daegu, Korea*.

[13] H. Grirate, H. Agalit, N. Zari, A. Elmchaouri, S. Molina, and R. Couturier. Experimental and numerical investigation of potential filler materials for thermal oil thermocline storage. *Solar Energy*, 131:260–274, 2016.

[14] S.M. Hasnain. Review on suitable thermal energy storage technologies, part 1: Heat storage materials and techniques. *Energy conversion management*, 11:1127–1138, 1998.

[15] F. Hengstberger, C. Zauner, K. Resch, S. Holper, and M. Grobbauer. High temperature phase change materials for the overheating protection of facade integrated solar thermal collectors. *Energy and Building*, 124, 2016.

[16] J.-F. Hoffmann, T. Fasquelle, V. Goetz, and X. Py. A thermocline thermal energy storage system with filler materials for concentrated solar power plants: Experimental data and numerical model sensitivity to different experimental tank scales. *Applied Thermal Engineering*, 100:753–761, 2016.

[17] Murat M. Kensisarin. High-temperature phase change materials for thermal energy storage. *Renewable and Sustainable Energy Reviews*, 14:955–970, 2010.

[18] Saba Khan. A review - an optimization of macroencapsulated paraffin used in solar latent heat storage unit. *International Journal of Engineering and Technical Research*, 2016.

[19] Doerte Laing, Tomas Bauer, Nils Breidenbach, Bernd Hachmann, and Maike Johnson. Development of high temperature phase-change-material storages. *Applied Energy*, 109:497–504, 2013.

[20] Marc Medrano, Gil Antoni, Ingrid Martorell, Xavi Potau, and Luisa F. Cabeza. State of the art on high-temperature thermal energy storage for power generation. part 2—case studies. *Renewable and Sustainable Energy Reviews*, 14:56–72, 2010.

[21] Harald Megling and Luisa F. Cabeza. *Heat and cold storage with PCM.* Springer, Berlin, 2008.

[22] H. Mehling, P. Schossig, and D. Kalz. Latent heat storage in buildings, storing heat and cold in a compact and demand-oriented manner. *BINE Informationsdienst*, 1, 2009.

[23] S. Quoilin, A. Desideri, J. Wronski, I. Bell, and V. Lemort. Thermocycle: A modelica library for the simulation of thermodynamic systems. 2014.

[24] Atul Sharma, V.V. Tyagi, C.R. Chen, and D. Buddhi. Review on thermal energy storage with phase change materials and applications. *Renewable and Sustainable Energy Reviews*, 13:318–345, 2009.

[25] Barz Tilman, Christoph Zauner, Daniel Langer, Diana Lopez Cardenas, Florian Hengstberger, Mariano Nicolas Cruz Bournazou, and Klemens Marx. Experimental analysis and numerical modeling of a shell and tube heat storage unit with phase change materials. *Industrial and Engineering Chemistry Research*, 55:8154–8164, 2016.

[26] VDI-Gesellschaft Verfahrenstechnik und Chemieingenieurwesen. *VDI Heat Atlas.* Springer, Berlin, 2010.

[27] B. Zalba, J. M. Marn, L. F. Cabeza, and H. Mehling. Review on thermal energy storage with phase change: materials, heat transfer analysis and applications. *Applied thermal engineering*, 23:251–283, 2003.

[28] Christoph Zauner, Florian Hengstberger, Mark Etzel, Daniel Lager, Rene Hofmann, and Heimo Walter. Experimental characterization and simulation of a fin-tube latent heat storage using high density polyethylene as pcm. *Applied Energy*, 179:237–246, 2016.

List of Figures

List of Tables